

S&L -I  
M

Report No. FR-79-73-697  
HAC Ref. No. D8855

sepucha *CS*

then file: Hughes: A03503

35

SLL 82-250/M-I

---

# HOLOGRAPHIC AXICON STUDY FINAL REPORT

## CONTRACT NO. F30602-76-C-0402

MARCH 1979

DISTRIBUTION STATEMENT A

Approved for public release  
Distribution Unlimited

AEROSPACE GROUPS

**HUGHES**

HUGHES AIRCRAFT COMPANY  
CULVER CITY, CALIFORNIA

DTIC QUALITY INSPECTED 4

PLEASE RETURN TO:

BMD TECHNICAL INFORMATION CENTER  
BALLISTIC MISSILE DEFENSE ORGANIZATION  
7100 DEFENSE PENTAGON  
WASHINGTON D.C. 20301-7100

19980309 358

43891

Accession Number: 3891

Publication Date: Mar 01, 1979

Title: Holographic Axicon Study Final Report

Corporate Author Or Publisher: Hughes Aircraft Company, Culver City, CA Report Number: FR-79-73-697

Report Prepared for: Rome Air Development Center, Griffiss AFB, NY Report Number Assigned by Contract Monitor: SLL 82-250/M-I; HAC Ref. No. D8555

Comments on Document: Archive, RRI, DEW

Descriptors, Keywords: Holographic Axicon Geometry Property Mix Compact Resonator Magnification Reentrant Ray Polarization  
Waxicon Model Align Misalign Hexagon Modification Efficiency

Pages: 00094

Cataloged Date: Nov 23, 1992

Contract Number: F30602-76-C-0402

Document Type: HC

Number of Copies In Library: 000001

Record ID: 25215

Source of Document: DEW

Report No. FR-79-73-697  
HAC Reference No. D8855

Holographic Axicon Study  
Final Report

Contract No. F30602-76-C-0402

March 1979

Submitted to

Rome Air Development Center (PMRZ)  
Griffiss Air Force Base, New York

Electro-Optical and Data Systems Group  
AEROSPACE GROUPS  
Hughes Aircraft Company • Culver City, California

## ACKNOWLEDGMENTS

This work was performed jointly by the Laser Systems Division, the Research Laboratories, and the Strategic Systems Division of Hughes Aircraft Company. The principal investigators were David Fink and Richard C. Smith of the Laser Systems Division, resonator analysis; Anson Au and Monica L. Minden of the Research Laboratories, axicon fabrication and measurement; and Paul D. Atcheson of the Strategic Systems Division, detailed axicon ray trace. We also wish to acknowledge the assistance of Carolyn L. Sauer with resonator analysis; Charles M. Hammill for incorporating the resonator code into the general optical design package; Merry N. Colborn for grating fabrication; Hugh L. Garvin and Klaus N. Robinson for ion machining, and Wayne P. Fleming for the scanning electron microscope photographs.

## CONTENTS

1.0	INTRODUCTION .....	1-1
2.0	GEOMETRIC PROPERTIES OF THE MIXING AXICON RESONATOR .....	2-1
2.1	The Completely Compacted Resonator .....	2-1
	Magnification .....	2-1
	Reentrant Rays .....	2-3
	Almost Reentrant Rays .....	2-5
2.2	The Incompletely Compacted Resonator .....	2-7
	Magnification .....	2-8
	Reentrant Rays .....	2-9
	Non-reentrant Rays .....	2-11
3.0	ROTATION OF POLARIZATION BY WAXICON ELEMENTS...	3-1
4.0	COMPUTER MODELING .....	4-1
4.1	Description of Resonator Modeling Code .....	4-1
4.2	Modeling Method .....	4-4
4.3	Resonator Models .....	4-5
4.4	Aligned Results .....	4-9
4.5	Misaligned Resonators .....	4-21
4.6	Length Variation and Sampling Rate .....	4-24
4.7	Conclusions .....	4-29
5.0	DETAILED AXICON MODEL .....	5-1
5.1	Task Requirements .....	5-1
5.2	The Tasks .....	5-1
5.3	Hexagon Modifications .....	5-4
5.4	Conclusion .....	5-7

## CONTENTS (Continued)

6.0	AXICON FABRICATION AND MESAUREMENT . . . . .	6-1
6.1	Tasks . . . . .	6-1
6.2	Visible Grating Axicon Fabrication – Holographic Technique . . . . .	6-3
6.3	Linear Grating Fabrication . . . . .	6-6
6.4	Circular Grating Fabrication . . . . .	6-11
	Quality of the Conical Axicon . . . . .	6-14
	Controlling the Intensity Distribution in the Exposure Plane . . . . .	6-18
	IR Techniques . . . . .	6-22
	Computer Generated Grating Axicon . . . . .	6-24
6.5	Efficiency and Polarization . . . . .	6-32
6.6	Phase Measurement . . . . .	6-35

## LIST OF ILLUSTRATIONS

Figure		Page
1-1	Real Axicons Can be Replaced with Holographic Axicons . . . . .	1-2
1-2	Mixing Axicons are Possible with Holographic Construction . . . . .	1-2
2-1	Mixing Axicon Ring Resonator . . . . .	2-2
2-2	Complete and Incomplete Compactors . . . . .	2-8
3-1	Waxicons Do Not Preserve Polarization . . . . .	3-2
3-2	Axicons Do Preserve Polarization . . . . .	3-2
3-3	Waxicons Can be Designed to Preserve Polarization by Having One Reflection Less than Brewster's Angle and the Other Greater . . . . .	3-4
4-1	Active Medium Accounted for by Lumped Gain and Refractivity . . . . .	4-2
4-2	Segment Broken into Stream Tubes and Flux Boxes . . . . .	4-3
4-3	Beam Expansion into Annular Shape and Recompression by Axicon Elements . . . . .	4-5
4-4	Ring Resonator with Circular Beam of Diameter 3.8 cm Expanded and Recompressed by Real Axicons . . . . .	4-6
4-5	Ring Resonator with Circular Beam of Diameter 3.8 cm Expanded and Recompressed by Axicon Elements . . . . .	4-7
4-6	Phase and Irradiance Distributions in Scrambled Starter Wave . . . . .	4-10
4-7	Phase and Irradiance Distributions at Feedback Mirrors for $M = 1.4$ , All-Geometric Resonator . . . . .	4-13
4-8	Phase and Irradiance Distribution at Feedback Mirror for $M = 2.0$ , All Geometric Resonator . . . . .	4-14
4-9	Phase and Irradiance Distribution at Feedback Mirror for $M = 2.8$ , All Geometric Resonator . . . . .	4-16

# LIST OF ILLUSTRATIONS (Continued)

Figure		Page
4-10	Phase and Irradiance Distribution at Feedback Mirror for $M = 1.4$ , Holographic Axicon Resonator . . . . .	4-17
4-11	Phase and Irradiance Distribution at Feedback Mirror for $M = 2.0$ , Holographic Axicon Resonator with No Gain . . . . .	4-18
4-12	Phase and Irradiance Distribution at Feedback Mirror for $M = 2.0$ , Holographic Axicon Resonator with Gain . .	4-19
4-13	Phase and Irradiance Distribution at Feedback Mirror for $M = 1.4$ , Holographic Axicon Resonator, Along Direction of 100 Microradian Tilt . . . . .	4-22
4-14	Phase and Irradiance Distribution at Feedback Mirror for $M = 2.0$ , All-Geometric Axicon Resonator, Along Direction of 100 Microradian Tilt . . . . .	4-23
4-15	Phase and Irradiance Distribution at Feedback Mirror for $M = 1.4$ , Holographic Axicon Resonator, Along Direction of $10^{-4}$ cm Offset . . . . .	4-25
4-16	Phase and Irradiance Distribution at Feedback Mirror for $M = 1.4$ , All-Geometric Axicon, Along Direction of $0.5 \times 10^{-4}$ cm Offset . . . . .	4-26
4-17	Phase and Irradiance Distribution at Feedback Mirror for $M = 1.4$ , Holographic Axicon Resonator with 130 cm Compacted Length . . . . .	4-27
4-18	Phase and Irradiance Distribution at Feedback Mirror for $M = 2.0$ , All-Geometric Axicon Resonator . . . . .	4-28
5-1	Axicon Beam Expander Profiles . . . . .	5-2
5-2	Axicon Beam Contractor Profile . . . . .	5-3
5-3	Holographic Axicon Expander Output Amplitude . . . . .	5-4
5-4	Conventional Axicon Contractor Output Amplitude . . . . .	5-5
6-1	Holographic Grating Axicon . . . . .	6-1
6-2	Self-Referencing Exposure Geometry for a Holographic Grating Axicon . . . . .	6-4
6-3	Transmitted Annular Beam Shows Circular Polishing Striations of Refracting Cone . . . . .	6-5
6-4	$1 \mu\text{m}/\text{cycle}$ Grating Recorded in $4200^{\circ}\text{A}$ of Photoresist with Standing Wave Nodal Separation of $1314^{\circ}\text{A}$ . . . . .	6-7



# LIST OF ILLUSTRATIONS (Continued)

Figure		Page
6-5	1 $\mu\text{m}$ /Cycle Grating Recorded in 1000 $^{\circ}\text{A}$ of Photoresist . . . . .	6-9
6-6	Experimental Data of Duty Cycle Versus Exposure for 1 $\mu\text{m}$ /Cycle Grating on 4200 $^{\circ}\text{A}$ of Photoresist . . . . .	6-12
6-7	Experimental Data of Duty Cycle Versus Exposure for 1 $\mu\text{m}$ /Cycle Grating on 1000 $^{\circ}\text{A}$ of Photoresist . . . . .	6-13
6-8	Results of Construction Axicon Design Analysis . . . . .	6-14
6-9	Interferometric Testing of Refractive Conical Axicon . . . . .	6-15
6-10	Twenty-six Degree BK-7 Axicon, as Received . . . . .	6-16
6-11	Twenty-six Degree BK-7 Axicon, as Received . . . . .	6-16
6-12	Twenty-six Degree BK-7 Axicon, after First Resurfacing . . . . .	6-18
6-13	Twenty-six Degree BK-7 Axicon, After Second Resurfacing . . . . .	6-18
6-14	Twenty-six Degree BK-7 Axicon, After Second Resurfacing . . . . .	6-19
6-15	The Interference of Two Waves Produces a Sinusoidal Intensity Variation for Holographic Exposures . . . . .	6-21
6-16	Fringe Contrast and Intensity Variation in the Exposure Plane of a Holographic Grating Axicon Recording System . . . . .	6-22
6-17	Two Methods of Generating a Compensating Filer for Exposure of a Holographic Axicon, Using Photographic Superposition . . . . .	6-23
6-18	Specifications of the Computer Plotted and Photo-reduced IR Grating Axicon Pattern . . . . .	6-25
6-19	Microscopic Photographs of Reduced Chrome Mask Pattern for IR Grating Axicon . . . . .	6-28
6-20	Photoresist Grating Axicon is Exposed Using the Chrome Master Pattern . . . . .	6-29
6-21	Grating Axicon Center Ion Machines in Gold . . . . .	6-30
6-22	Ion-Machined 15.24 $\mu\text{m}$ /Cycle Grating Axicon Profiles in Gold . . . . .	6-31
6-23	Predicted Diffraction Efficiency of a Grating Axicon; Angular Variation . . . . .	6-33

# LIST OF ILLUSTRATIONS (Continued)

Figure		Page
6-24	Measuring the Diffraction Efficiency of a Grating Axicon . . . . .	6-34
6-25	Measured Diffraction Efficiency of Four Grating Axicon Samples . . . . .	6-35
6-26	Point Diffraction Interferometry at 10.6 $\mu\text{m}$ . . . . .	6-36
6-27	Interferogram of PDI System Without Axicon Rhomb . . . . .	6-37

## LIST OF TABLES

Table		Page
4-1	Daughter Rays in HGA Ring . . . . .	4-8
4-2	. . . . .	4-30

## 1.0 INTRODUCTION

The major application annular resonators are being designed for is high power chemical lasers. Since the excited species produced in the pumping reactions typically decay very rapidly, a configuration that affords high gain volume with relatively small length in the gas flow direction will have to be part of a successful high power design. Considerable attention has recently attached to a cylindrical annular gain region as a prospective choice, provided that the optical beam can be induced to extract energy efficiently in such a situation. This program is concerned with the performance of a resonator in which a circular beam is expanded into an annular shape by a pair of axicon elements prior to entering the gain region, and subsequently recompactd by another axicon pair. In particular, the contribution to be expected from a holographic grating axicon (HGA), described below, is investigated.

The Holographic Axicon Resonator study had two objectives: a preliminary investigation of mode control in an annular resonator using the new concept of a holographic mixing axicon; and development of methods for fabricating and testing holographic mixing axicons.

Holographic axicons spring from noting that a real axicon can be replaced with a diffractive optics equivalent constructed from equally spaced circular grooves, as shown in Figure 1-1. While such an axicon is quite different from a real axicon in such practical aspects as fabrication and cooling, its net optical effect is not particularly different. However, a diffractive element may be constructed as in Figure 1-2 to amplitude split the incoming wave and send a full-width sample of the compact region into diametrically opposite portions of the annular region rather than just half the width into each portion.

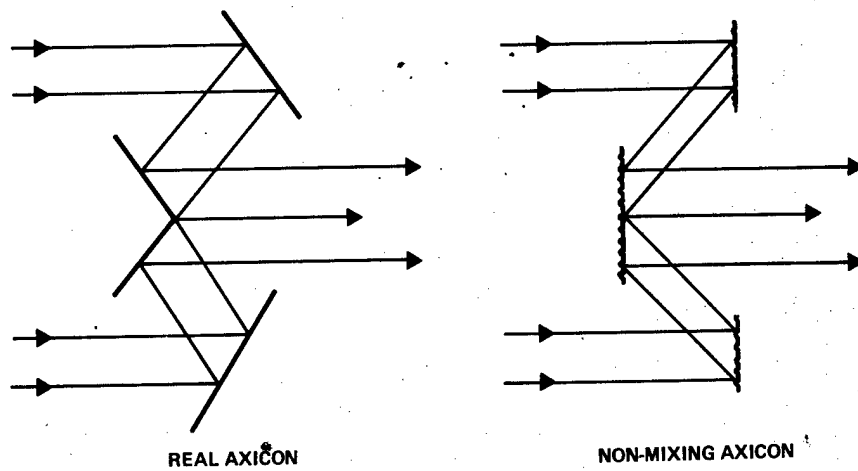


Figure 1-1. Real axicons can be replaced with Holographic axicons.

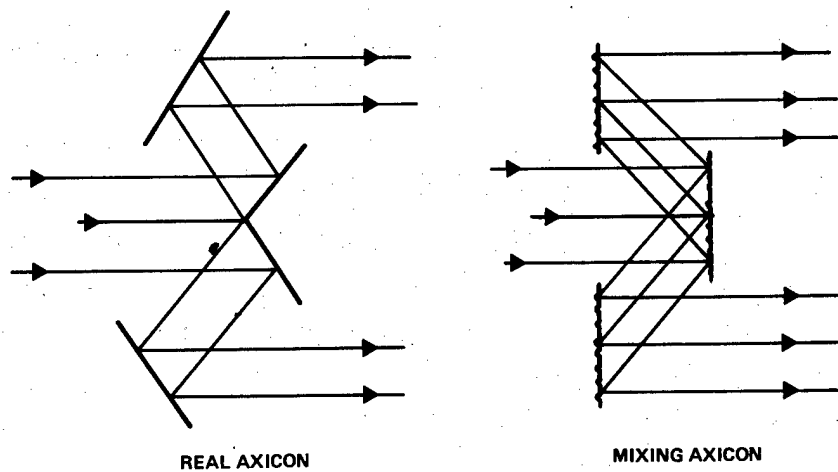


Figure 1-2. Mixing axicons are possible with Holographic construction.

This type of grating axicon is referred to as a "mixing axicon"; it is this feature that makes the holographic axicon so promising for use in annular resonators. It has proven difficult to obtain good phase quality (i. e., to obtain good mode control) with conventional axicons in an annular resonator. This is due to the fact that different azimuthal regions of the annular part of the resonator are coupled weakly or not at all to other regions. Holographic grating axicons should provide a number of important advantages for annular resonators, including:

1. Stronger coupling of all parts of the annulus due to the mixing or beam-splitting action of the holographic grating axicon.
2. Elimination of the tip geometry of the conventional axicon as a detriment to mode control; the region of the holographic axicon resonator from which coherence is established is an annulus rather than the central filament as in the conventional annular resonator.

Consequently even if recombination from the annular region were to take place by a conventional axicon, the shape of the tip region would not be critical because the coherence is controlled by the annulus. In fact, the tip could be blunted without affecting the output quality; diffraction would quickly fill in the hole.

The mixing axicon should only be used as a splitter, not a combiner, because as a combiner there are severe alignment tolerances so that the combining beams interfere constructively, not destructively. As a splitter, the tolerances should be similar to those of a real axicon. Because of this restriction, a ring resonator was designed. However, further investigation may show the alignment tolerance to be not much more severe than for a conventional axicon. Off-centering an element of a conventional axicon by  $1/2$  a wavelength causes a 1 wavelength distortion of the transmitted beam.

The holographic axicon ring resonator is shown in Figure 2-1. The axicon on the right is a holographic equivalent of a conventional real axicon. This holographic axicon does not endow the resonator with any special optical properties but does have the practical features of a flat substrate, i. e., it is easy to manufacture and to cool compared to a conical substrate. This type of virtual axicon may be substituted for any real axicon with consideration given to its wavelength dependent magnification.

The unusual optical properties come from the left axicon, which has no conventional counterpart. This element is designed to diffract equally into both the +1 and -1 orders. Thus a mixing axicon is created as distinct from the non-mixing axicon on the right. The most apparent optical property the mixing axicon gives to this resonator is that the upper path and the lower path in the annular region are coherent because they are split from the same wavefront.

On closer examination, further unusual properties appear. An unstable resonator of magnification 2 results if all mirrors are plane. For this magnification, every ray retraces its path every second round trip. For other magnifications, a ring of rays in the compacted region repeats itself every second round trip.

## 2.0 GEOMETRIC PROPERTIES OF THE MIXING AXICON RESONATOR

### 2.1 THE COMPLETELY COMPACTED RESONATOR

#### Magnification

A drawing of the resonator is presented in Figure 2-1. The resonator is drawn with full virtual axicons at both ends - the mixing central axicon with a virtual outer axicon at the left, and a virtual outer axicon with a virtual non-mixing central axicon at the right. Any of the axicons except the mixing can be replaced with a real axicon.

With an all-virtual system, it can be seen that the diameter of the compacted section on the left is equal to the thickness of the annular beam. If the outer virtual axicon on the left is replaced with a real axicon, the thickness of the annulus,  $t$ , becomes

$$t = D_1 \cos \theta_1,$$

where  $D_1$  is the diameter of the compacted beam on the left and  $\theta_1$  is the angle of diffraction, measured from the normal, at the mixing axicon. The annular thickness may be written as

$$t = S_1 D_1,$$

where  $S_1 = 1$  or  $S_1 = \cos \theta$  for the virtual or real outer axicon, respectively.



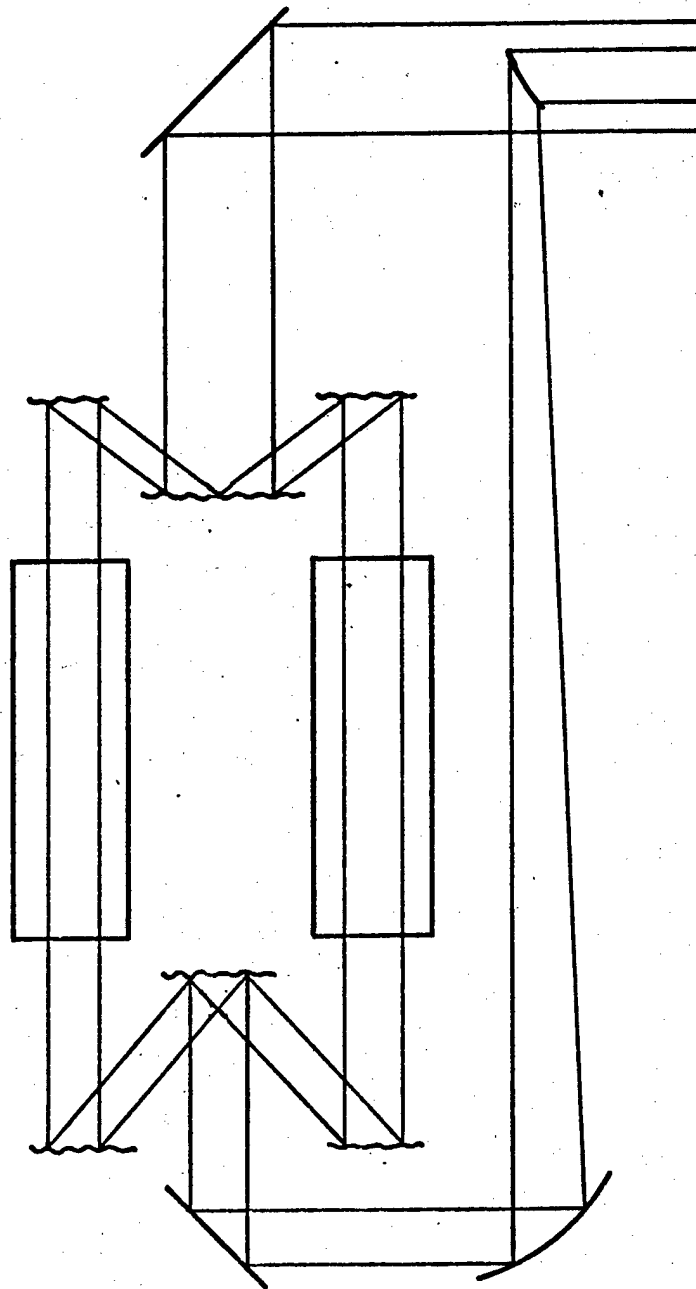


Figure 2-1. Mixing axicon ring resonator.

At the right, with both axicons virtual or both axicons real,

$$D_2 = 2t,$$

where  $D_2$  is the diameter of the compacted section on the right. If the inner axicon is real and the outer virtual,

$$D_2 = 2t \cos \theta_2,$$

where  $\theta_2$  is the angle of diffraction at the outer axicon. If the inner axicon is virtual and the outer real,

$$D_2 = 2t / \cos \theta_3,$$

where  $\theta_3$  is the angle of diffraction at the inner axicon.

The compacted diameter at the right may be written as  $D_2 = 2S_2t$ , where  $S_2 = 1$  or  $S_2 = \cos \theta_2$  or  $S_2 = 1/\cos \theta_3$ .

The sizes of  $D_1$  and  $D_2$  are determined by the feedback coupling and the magnification of the feedback leg. The feedback mirror is of diameter  $D_1/m$ , where  $m$  is the magnification of the feedback leg. Note  $m$  is not the resonator magnification. The resonator magnification is

$$M = mD_2/D_1 = 2mS_1S_2$$

Unlike a conventional unstable resonator, this magnification applies only to the diameter of the geometric beams, and not to the ray locations on successive passes.

### Reentrant Rays

We may now trace rays around the resonator. Consider a ray that is a distance  $a$  above the axis at the entrance to the mixing axicon. This ray will split into two rays at the axicon. We will follow the ray that stays closer to the axis. In the annular region, this ray is a distance  $S_1a$  above the center

of the annular section, or a distance  $-S_1(D_1/2-a)$  from the inside edge of the annulus. When the beam is compacted at the right, this ray will be a distance  $-S_1S_2(D_1/2-a)$  from (below) the axis.

If this ray is fed back, it will arrive at the mixing axicon a distance  $-mS_1S_2(D_1/2-a)$  from the axis. Using the equation for the resonator magnification, this distance is  $-(D_1/2-a)M/2$ . As this ray is below the axis, whereas the original ray was above, the ray cannot be reentrant (close back upon itself). However, after another trip around the ring it will again be above the axis and could be reentrant.

To get the reentrant condition, the distance  $-(D_1/2-a)M/2$  cannot be substituted back into itself because the formula is only for positive  $a$ . This is because at the mixing axicon, the ray that went down, not up, was chosen. For negative  $a$ , the up ray would have been chosen. For negative  $a$  the formula for the return ray location is  $(D_1/2+a)M/2$ . Now the reentrant condition for two round trips may be written:

$$a = \left\{ \frac{D_1}{2} - \left[ \left( \frac{D_1}{2} - a \right) \frac{M}{2} \right] \right\} \frac{M}{2},$$

which yields

$$a(M^2 - 4) = (MD_1/2)(M-2).$$

Therefore

$$a = \frac{D_1}{2} \frac{M}{M+2},$$

but we must also check the divided out factor,  $M - 2$ .

Substituting  $M = 2$  back into the two pass reentrant condition, we get  $a=a$ . Therefore for  $M = 2$ , all rays are reentrant after two round trips -- if they are fed back. To see which rays are fed back, we check the location of the ray.

after one trip for  $M = 2$ :  $-(\frac{D_1}{2} - a)$ . As  $a$  varies from 0 to  $D_1/2$ , the one trip return ray location varies from  $-D_1/2$  to 0. As these locations are all within the beam, all of these rays have been fed back. In summary, for  $M = 2$ , all rays are fed back and all are reentrant after two trips.

Now let us reexamine the general case reentrant rays. The formula for the ray location after one trip was derived under the assumption that the ray was fed back. The reentrant ray that starts out at

$$a = \frac{D_1}{2} \frac{M}{M+2}$$

arrives after one trip at

$$-\left(\frac{D_1}{2} - \frac{D_1}{2} \frac{M}{M+2}\right) \frac{M}{2},$$

which reduces to

$$-\frac{D_1}{2} \frac{M}{M+2};$$

that is, at the same distance from the axis as it started, but on the other side of the axis. Because this returned ray is at the same distance as the original, it was fed back. In summary, for any magnification, there is a ring of rays that are reentrant after two trips.

#### Almost Reentrant Rays

Consider a ray that starts out a distance  $a_o$  from the axis. After one round trip it is at a distance

$$a_1 = -\left(\frac{D_1}{2} - a_o\right) \frac{M}{2}.$$

After two round trips it is at

$$a_2 = \left( \frac{D_1}{2} - \frac{M}{2} \frac{D_1}{2} + \frac{M}{2} a_o \right) \frac{M}{2} .$$

After three trips it is at

$$a_3 = - \left( \frac{D_1}{2} - \frac{M}{2} \frac{D_1}{2} + \left( \frac{M}{2} \right)^2 \frac{D_1}{2} - \left( \frac{M}{2} \right)^2 a_o \right) \frac{M}{2} .$$

After four trips,

$$a_4 = \left( \frac{D_1}{2} - \left( \frac{M}{2} \right) \frac{D_1}{2} + \left( \frac{M}{2} \right)^2 \frac{D_1}{2} - \left( \frac{M}{2} \right)^3 \frac{D_1}{2} + \left( \frac{M}{2} \right)^3 a_o \right) \frac{M}{2} .$$

After n trips,

$$a_n = (-1)^n \left[ \frac{D_1}{2} \sum_{i=1}^n \left( -\frac{M}{2} \right)^{i-1} - \left( -\frac{M}{2} \right)^{n-1} a_o \right] \frac{M}{2} ,$$

$$a_n = (-1)^n \left[ \frac{D_1}{2} \frac{M}{2} \frac{\left( \frac{M}{2} \right)^n - 1}{-\frac{M}{2} - 1} - \left( -\frac{M}{2} \right)^n a_o \right] .$$

If  $M < 2$ , we may take the limit as  $n \rightarrow \infty$  of  $|a_n|$ ,

$$\lim_{n \rightarrow \infty} |a_n| = \frac{D_1}{2} \frac{M}{M+2} ,$$

which is the location of the reentrant ring. So for  $M < 2$ , all rays condense to the reentrant ring. This does not imply a catastrophic intensity problem because we have only been following one of the two rays leaving the mixing axicon.

For  $M > 2$ , we take the equation relating  $a_n$  and  $a_o$  and solve for  $a_o$ :

$$a_o = \left(\frac{2}{M}\right)^n a_n + \frac{D_1}{2} \frac{M}{2} \frac{1 - \left(\frac{-2}{M}\right)^n}{\frac{M}{2} + 1}$$

Now by taking the limit as  $n \rightarrow \infty$ , we find the source of all rays:

$$a_o = \frac{D_1}{2} \frac{M}{M+2},$$

which again is the location of the reentrant ring. The reentrant ring for  $M > 2$  is analogous to the axial filament of a conventional unstable resonator.

In the next section, a different approach to the problem shows the general ray changes its distance from the reentrant ring by  $M/2$  on each pass and alternates from inside the ring to outside.

## 2.2 THE INCOMPLETELY COMPACTED RESONATOR

The previous geometric analysis of the mixing axicon resonator, Figure 2-1, treated the case of a fully compacted resonator; that is, one in which the compacting axicon brought the geometric beams precisely together so they met at the axis. This section will treat an incompletely compacted resonator, where the beams are not brought to the center axis. Drawings of complete and incomplete compactors are shown in Figure 2-2.

A fully compacted resonator may not be desirable for several reasons.

- 1) There may be difficulty in figuring the tip of the real axicon or forming the grooves at the center of the virtual.
- 2) The flux loadings become very high at the axial location.
- 3) Due to diffraction, power in the contracting beams may miss the tip of the real axicon or illuminate the incorrect side of the virtual axicon and be lost.

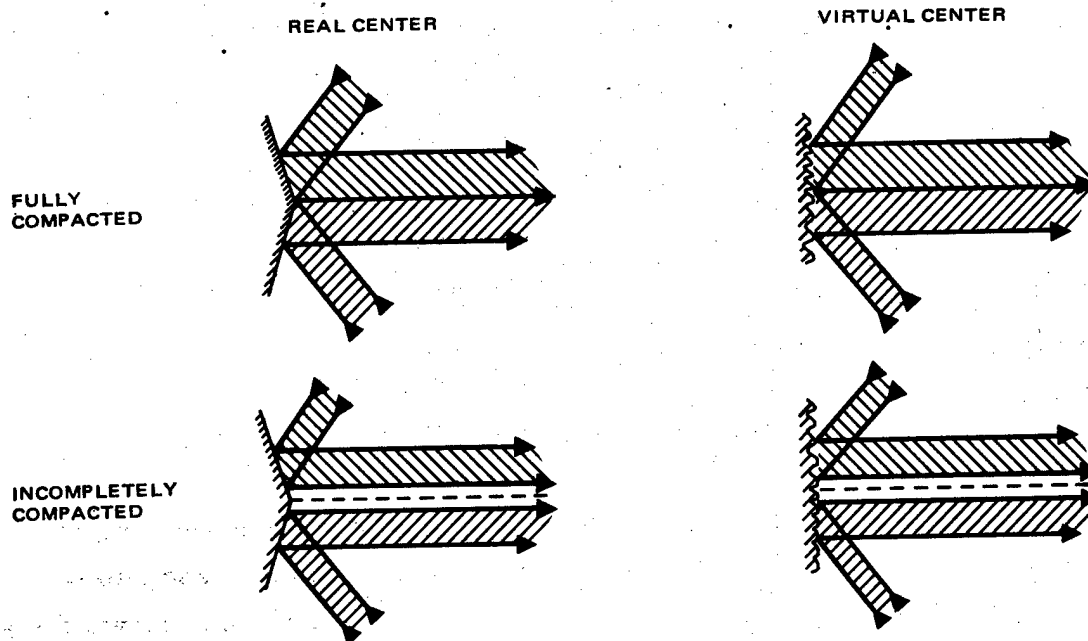


Figure 2-2. Complete and incomplete compactors.

### Magnification

The notation used will be that of the last section:  $D_1$  is the diameter of the beam incident on the mixing axicon,  $t$  is the thickness of the annular region,  $S_1$  is defined by  $t = S_1 D_1$ ,  $D_2$  is the diameter of the compacted beam leaving the non-mixing axicon,  $S_2$  is defined by  $D_2 = 2S_2 t$ ;  $m$  is the magnification of the feedback leg. One new parameter is needed:  $b$  is the incomplete compaction distance -- the distance from the axis to the inside edge of the hollow compacted region to the right of the non-mixing axicon. The resonator magnification is

$$M = mD_2/D_1 = 2m(S_2 t + b)/D_1 ,$$

$$M = 2m(S_1 S_2 + b/D_1) .$$

### Reentrant Rays

Consider a ray that is a distance  $a$  above the axis at the entrance to the mixing axicon. This ray will split into two rays at the axicon. We will follow the ray that stays closer to the axis. In the annular region, this ray is a distance  $S_1 a$  above the center of the annular section, or a distance  $-S_1(D_1/2 - a)$  from the inside edge of the annular. When the beam is compacted at the right, this ray will be a distance  $-[S_1 S_2(D_1/2 - a) + b]$  from (below) the axis.

If this ray is fed back, it will arrive at the mixing axicon a distance  $-m[S_1 S_2(D_1/2 - a) + b]$  from the axis. As this ray is below the axis, whereas the original was above, the ray cannot be reentrant. However, after another trip around the ring it will again be above the axis and could be reentrant.

To obtain the reentrant condition, we note the above formula for the return distance is only for positive  $a$  because the down ray at the mixing axicon was chosen. For negative  $a$  the formula is

$$m[S_1 S_2(D_1/2 + a) + b], \quad a < 0$$

Substituting the first formula into the second, the reentrant condition for two round trips may be written:

$$a = m S_1 S_2 [D_1/2 - m S_1 S_2 (D_1/2 - a) - m b] + m b,$$

which yields

$$a[1 - (m S_1 S_2)^2] = m S_1 S_2 (D_1/2)(1 - m S_1 S_2) + m b (1 - m S_1 S_2).$$



Therefore

$$a = \frac{D_1}{2} \frac{mS_1S_2 + 2mb/D_1}{mS_1S_2 + 1},$$

but we must check the divided out factor,  $1 - mS_1S_2$ .

Substituting  $mS_1S_2 = 1$  back into the two pass reentrant condition, we get  $a = a$ . Therefore for  $mS_1S_2 = 1$ , all rays are reentrant after two round trips -- if they are fed back. To see which rays are fed back, we check the location of the ray after one round trip for  $mS_1S_2 = 1$ :

$$-(D_1/2 - a) - mb.$$

We must notice that the range available for  $a$  is not 0 to  $D_1/2$ , but  $mb$  to  $D_1/2$ . With incomplete compaction, there are no rays within a distance  $b$  of the axis to the right of the non-mixing axicon. This empty region is magnified by the feedback leg to give an empty core of radius  $mb$  at the entrance to the mixing axicon. As  $a$  varies from  $b/m$  to  $D_1/2$ , the one trip return location varies from  $-D_1/2$  to  $-mb$ . As these locations are all within the beam, all of these rays have been fed back. In summary, for  $mS_1S_2 = 1$ , all rays are fed back and all are reentrant after two trips.

Now let us examine the general case reentrant rays. The formula for the ray location was derived under the assumption that the ray was fed back. The reentrant ray that starts out at

$$a = \frac{D_1}{2} \frac{mS_1S_2 + 2mb/D_1}{mS_1S_2 + 1}$$

arrives after one trip at

$$-m \left[ S_1S_2 \left( \frac{D_1}{2} - \frac{D_1}{2} \frac{mS_1S_2 + 2mb/D_1}{mS_1S_2 + 1} \right) + b \right]$$

which reduces to

$$-\frac{D_1}{2} \frac{mS_1S_2 + 2mb/D_1}{mS_1S_2 + 1} ;$$

that is, at the same distance from the axis as it started, but on the other side. Because this returned ray is at the same distance as the original, it was fed back. In summary, for any magnification, there is a ring of rays that are reentrant after two trips.

#### Non-reentrant Rays

In general, if the path of a ray is traced through the resonator, with the branch nearest the axis chosen when a mixing axicon splits it into two orders, it is found that the ray does not return to its original location. If its initial position with respect to the beam axis is  $r_0$ , it will be at some different distance  $r_1$  after a complete circuit. The analysis above provides the relationship between  $r_0$  and  $r_1$ :

$$r_1 = -m[S_1S_2(D_1/2 - r_0) + b] .$$

If the positions are referred to the reentrant ring instead of the beam axis, that is, if one replaces  $r_0$  by  $a + \alpha_0$ , and  $r_1$  by  $-(a + \alpha_1)$ , one obtains

$$-a - \alpha_1 = -m[S_1S_2(D_1/2 - a - \alpha) + b] .$$

Using the equation that expresses the fact that rays at radius  $a$  are reentrant gives

$$\alpha_1 = -mS_1S_2\alpha_0 ;$$

the general ray's distance from the repeating ring is multiplied by  $-mS_1S_2$  in one pass through the resonator. The negative sign means it alternates between

inside the ring and outside. In terms of  $M$ , the magnification,

$$\alpha_1 = -\left(\frac{M}{2} - \frac{mb}{D_1}\right) \alpha_0,$$

so if  $M/2 > (1 + mb/D_1)$ , all rays diverge from the reentrant ring, while if  $M/2 < (1 + mb/D_1)$ , they collapse into it. The case  $M = (2 + 2mb/D_1)$  is again the case  $mS_1S_2 = 1$ , in which all rays are reentrant. As in the fully compacted resonator, the reentrant ring of the incompletely compacted resonator is analogous to the axial filament of a conventional unstable resonator.

### 3.0 ROTATION OF POLARIZATION BY WAXICON ELEMENTS

Consider the retro-axicon, or "waxicon" of Figure 3-1 for perfect dielectric reflections. A ray with vertical (north-south) polarization incident on the east or west sides will return with vertical polarization. A ray incident at the north or south also returns with vertical polarization but with a phase reversal. This phase reversal leads to the examination of a ray incident on the north-west side of the axicon. The tangentially polarized component returns with the same tangential polarization, but the radial component is returned with a phase reversal. Recombining the components yields horizontal (east-west) polarization. Following rays all around the axicon leads to the result that the plane of polarization of the returned rays is at an angle of  $2\theta$ , where  $\theta$  is the azimuthal angle around the annulus. Figure 3-2 shows how, under the same perfect dielectric conditions, the basic axicon does preserve polarization.

If the s and p reflectivities are not equal, the polarization directions are not as described for either the axicon or waxicon, as each vector is further rotated according to the relative amount of s and p in its construction. The phase shifts for reflection from a perfect dielectric are, for the p wave, 0 radians for incident angles less than Brewster's angle and  $\pi$  radians for angles larger, and for the s wave,  $\pi$  radians for all angles of incidence. For an imperfect dielectric or a metal, the phase shifts are not just 0 and  $\pi$  but vary continuously with the angle of incidence. If the difference between the s and p phase shifts is not exactly 0 or  $\pi$ , then the resultant polarizations in Figures 3-1 and 3-2 become elliptical with axes parallel and perpendicular to the linear polarization of the 0 and  $\pi$  phase shift case.

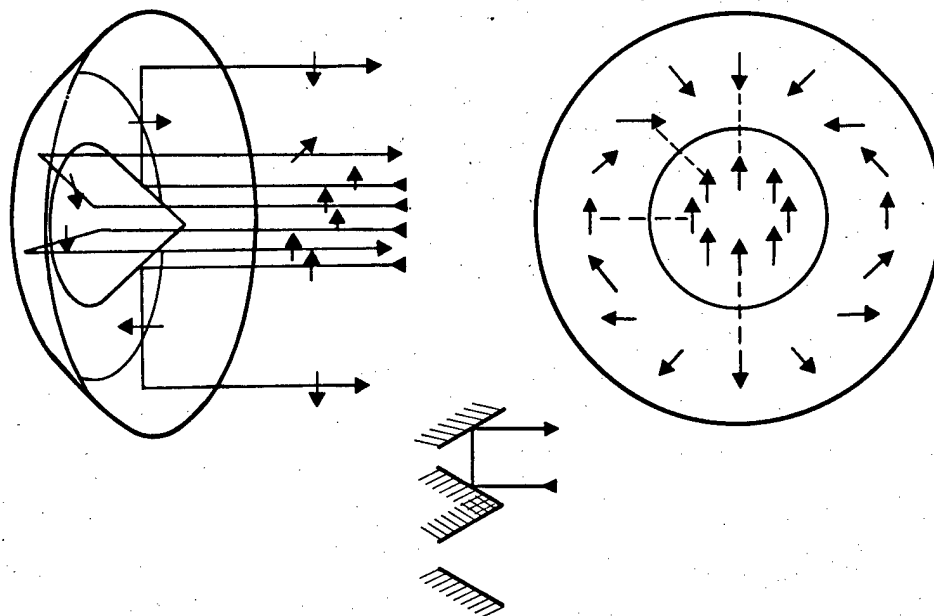


Figure 3-1. Waxicons do not preserve polarization. Perspective, front, and cross-section views for perfect dielectric reflection.

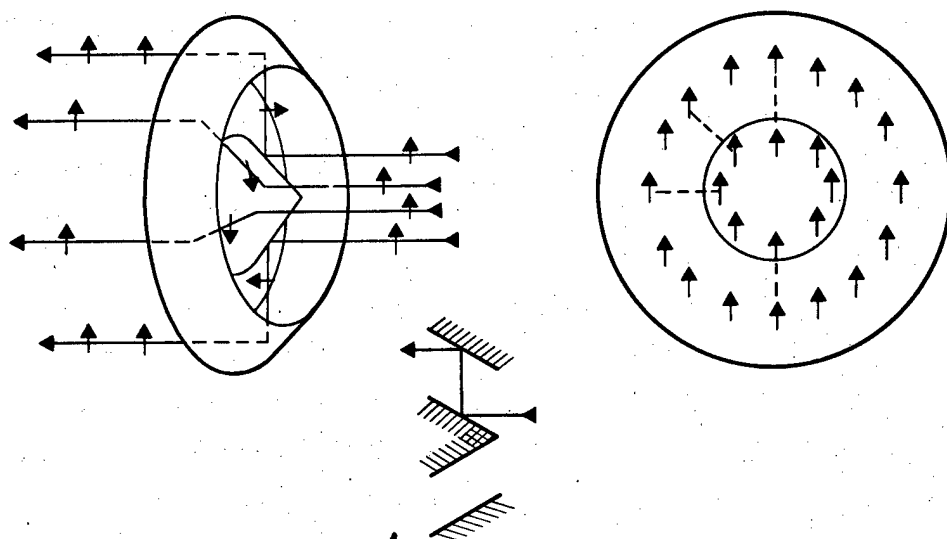


Figure 3-2. Axicons do preserve polarization. Perspective, front, and cross-section views for perfect dielectric reflection.

A retroreflecting cone will behave as a waxicon in its polarization transforming properties. An axicon or waxicon generated from a curve, one with optical power, will have to contend with a range of angles of incidence and the corresponding range in s and p reflectivities and phase shifts.

It is clear that due to their polarization properties, these elements have the potential for causing havoc within a resonator. Even without any diffraction, an odd number of encounters with perfect dielectric waxicons and cones will preclude a linearly polarized beam from reproducing itself in one round trip. Diffraction will prevent reproduction for an even number of encounters. Once a resonant mode is formed, the far-field irradiance will suffer if the output is not uniformly linearly polarized. For instance, if an output beam had a polarization variation similar to that from the waxicon in Figure 3-1, the on axis far-field irradiance would be zero.

There are some possible solutions. A waxicon can be designed to preserve polarization by making one of the reflections at less than Brewster's angle and the other greater, as shown in Figure 3-3. In any case, application of these elements will have to use dielectric coatings designed for matched s and p reflectivities and 0 or  $\pi$  relative phase shifts. The former will be satisfied if the coatings are designed for high reflectivity for both s and p, but the latter will require more care.

The holographic axicon, being analogous to the basic "through" type axicon, does not have the intrinsic polarization problem of the waxicon, but it is still subject to the effects of non-0 or  $\pi$  relative phase shift between the s and p polarizations. These phase shifts can be both calculated and measured, but neither has yet been done.

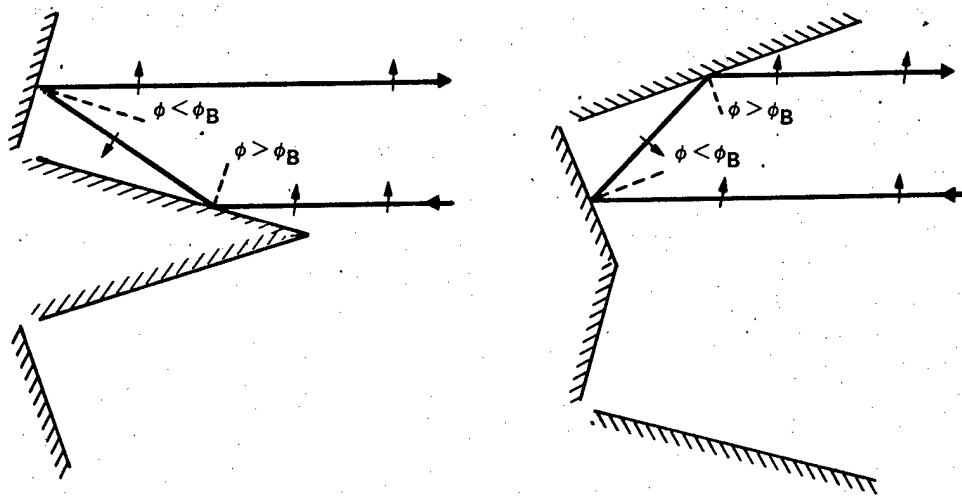


Figure 3-3. Waxicons can be designed to preserve polarization by having one reflection less than Brewster's angle and the other greater.

## 4.0 COMPUTER MODELING

### 4.1 DESCRIPTION OF RESONATOR MODELING CODE

The Hughes resonator/amplifier modeling code is a very flexible modeling tool that employs diffractive propagation within a three-dimensional resonator. It can handle resonators with folded and multiply overlapped beams within the medium, a flowing, saturable medium with gain and refractivity, shock waves, mirror thermal distortion, clipping apertures, and misalignments.

No a priori functional dependence is imposed on the solution. An initial guess of the solution is launched from one mirror and allowed to develop as it is propagated repeatedly around the resonator. When repeated iterations through the resonator cause no further changes in the wave at all locations, the propagating wave represents the steady-state solution of the resonator.

The diffractive optical propagation is computed in a converging or diverging coordinate system that accounts for the basic sphericity of the optical wave. This approach maintains the sampled points distributed over the same size region as the optical irradiance even though the size of this region may change over a propagation step. The equivalent collimated beam is propagated with an averaged kernel Fresnel integral. The Fresnel integral is computed efficiently by expressing it as a convolution, which is then evaluated by Fourier transforms.

The active medium is accounted for by a series of lumped gain and refractivity segments as shown in Figure 4-1. As a wave enters the medium at the left dashed plane of Figure 4-1, it loads the first medium segment. Next, one-half of the extraction is accounted for; that is, the



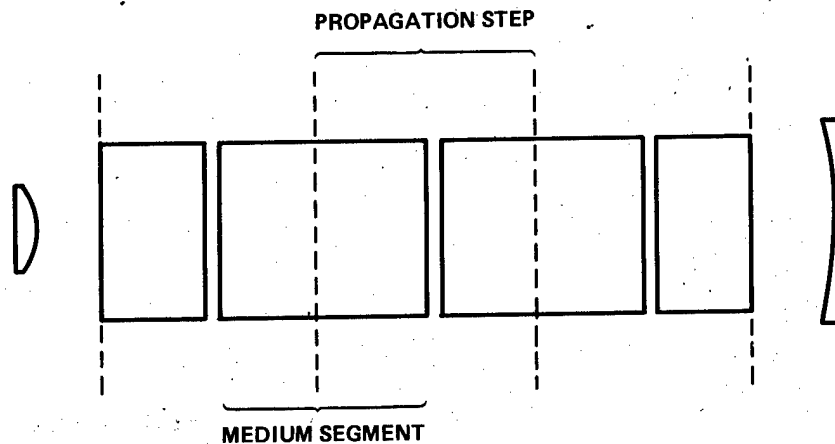


Figure 4-1. Active medium accounted for by lumped gain and refractivity.

wave is adjusted in amplitude and phase as determined by the gain and refractivity of the half-segment in front of it – the gain and refractivity determined by the total loading at the left dashed plane from the previous iteration. The wave is then propagated as if in vacuum to the second dashed plane. Its amplitude and phase are adjusted according to the gain and refractivity of the half-segment to the left of the second dashed plane, again determined by the loading from the previous iteration. The medium of the second segment is now loaded with the wave at the second dashed plane and the sequence is repeated: pre-extract, propagate, post-extract, load, until the end of the pass through the medium. The same process is repeated on any return or overlapped passes with the loadings added to the previous pass values. After a complete iteration, the accumulated loadings are used to calculate the gain and refractivity throughout the resonator for the next iteration.

Each medium segment is divided into a two-dimensional array of flux boxes. A column of flux boxes in the direction of the medium flow is called a stream tube, as shown in Figure 4-2. The loadings are accumulated by summing all of the field power that falls within each flux box every

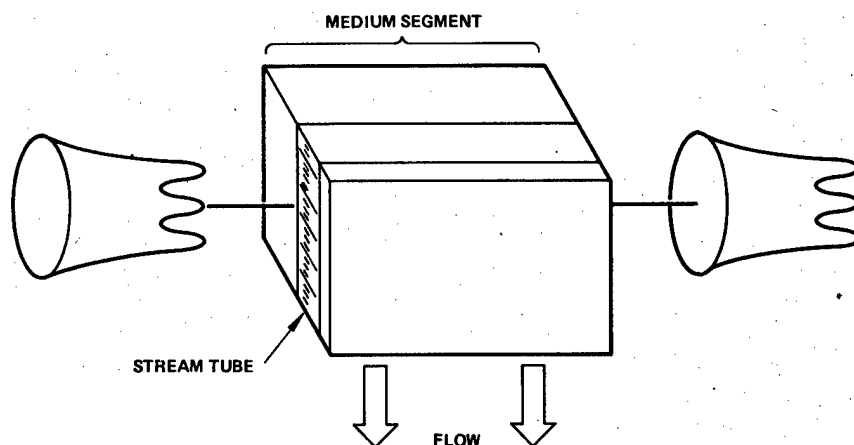


Figure 4-2. Segment broken into stream tubes and flux boxes.

time the wave passes on one iteration. The gain and refractivity are calculated from one of several available kinetics models, depending on the type of laser being modeled. For a supersonic  $\text{CO}_2$  gas dynamic laser, the kinetic rate equations that relate the energy transferred among the vibrational, rotational, and translational states and the radiation field are solved while following the medium flowing in a stream tube from the nozzle exit plane across the lasing cavity through the differently loaded flux boxes. As the kinetic equations are solved, the average gain and refractivity of each flux box are saved.

Because the mirrors, in general, are also subjected to more than one optical wave, a mirror loading array is accumulated in the same manner as the medium loading array and is used to calculate the total mirror thermal distortions.

Recently this modeling code or its predecessor has been successfully used on three Air Force Weapons Laboratories programs: The Airborne Laser Laboratory Cycle IV, design of a  $\text{CO}_2$  gas dynamic laser; SRAT Beam Control/Advanced Laser System, design of a  $\text{CO}_2$  E-beam pumped electric discharge laser; and SRAT Beam Control/BGDL, design of a bireactant  $\text{CO}_2$  gas dynamic laser.

## 4.2 MODELING METHOD

Resonators incorporating both real and virtual axicons can be modeled using this diffractive code. The code repeatedly propagates a field defined on a square grid of points around, in principle, any optical configuration, and iteration is continued until identical results on successive passes signal that the steady-state solution has been found. The square grid seems to involve inefficiency for annular devices since the central core of the beam is dark. For the very narrow rings proposed for chemical lasers, an annular propagation scheme is required for efficient calculation, but for this study, a rather thick doughnut can be used. In particular, an axicon magnification, defined as the ratio of annulus outer diameter to input beam diameter, of three results in 14 percent of the grid points in the hole for expansion of the type shown in 4-3a, while 8.6 percent are sacrificed if expansion is done using the HGA of Figure 4-3b with  $\theta = 45^\circ$ . To include diffracted energy, a guard band of points interior to the ring would have to be carried in any event, so the actual computation time penalty for using this well-established code is surely less than these percentages.

The effect of the axicons upon the beam seems most readily modeled by some sort of ray-tracing routine. Detailed codes for this exist, for example as part of the Hughes optical design code, but they are too expensive of calculation time for use in an iterative code. However, considerable information about mode quality can be extracted from resonator models in which all axicons are assumed to be in perfect alignment. In that case, simple ray- and amplitude-mapping functions are available. A beam tilt induced at the flat mirror which precedes expansion permits assessment of the effect of relative tilt of beam and axicon axes. The effects of relative displacement of beam and axicon axes, or decentration, are studied through a simplified ray tracing routine that assumes that the most important contributor to azimuth dependent phase changes in passing through an axicon pair is the azimuthally varying ray path from an entrance plane to the outer axicon. In the same spirit of computational efficiency, the gain region is modeled as a simple saturable gain system.

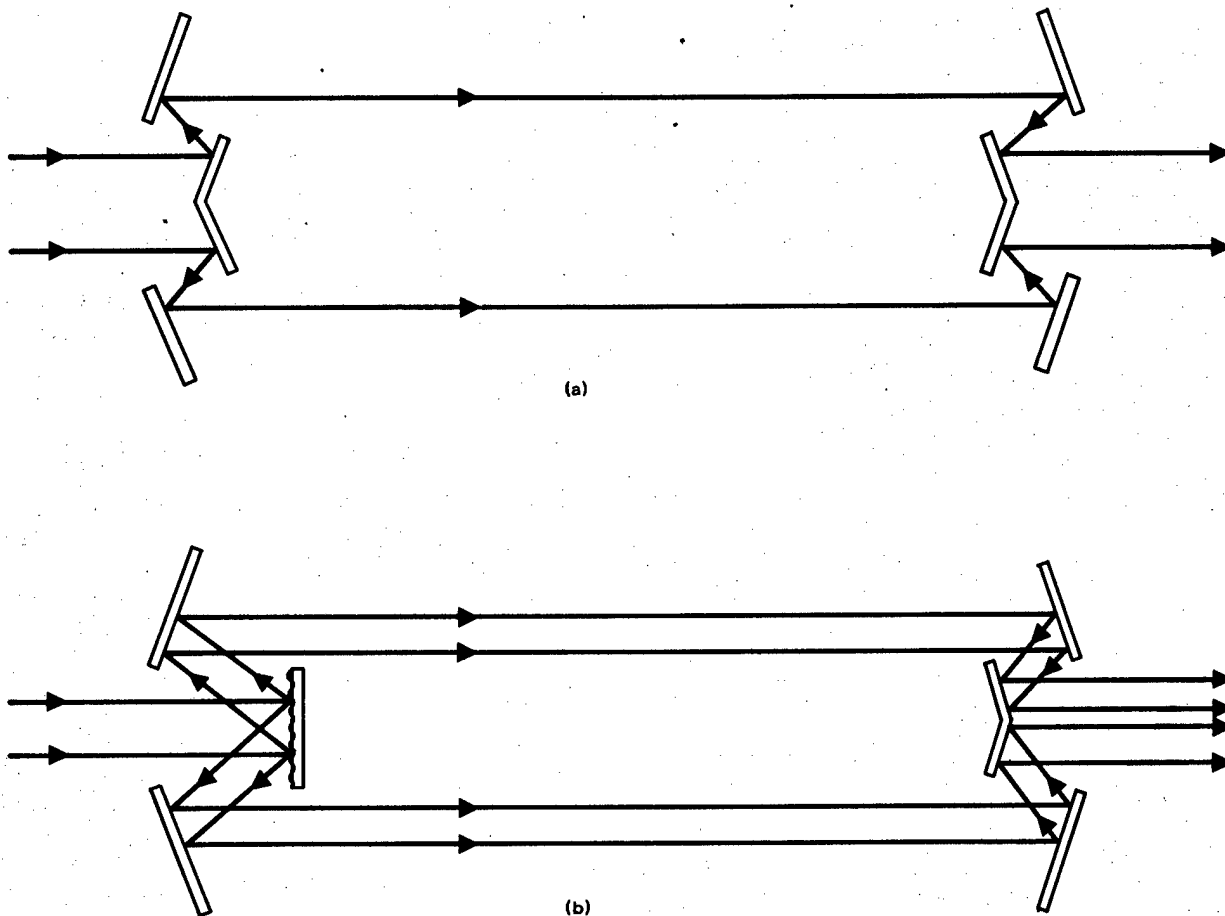


Figure 4-3. Beam expansion into annular shape and recompaction by axicon elements. (a) Expansion and compacting done by pairs of real axicons. (b) Same as (a) except that the inner cone of the expansion stage is replaced by a holographic grating axicon.

### 4-3 RESONATOR MODELS

The particular optical layouts chosen for study are shown in Figures 4-4 and 4-5. Although it is intended that these sketches be self-explanatory, a particular point should be made of the meaning of the two uses of the term "magnification". First, there is the usual resonator magnification, called  $M$  herein, which is the ratio of the full geometric beam diameter at the outcoupling element to the diameter of the feedback beam. Secondly, we also refer to a magnification in beam diameter at the expansion axicon pair. In the all-geometric axicon ring, this magnification is balanced by a return to the input beam size induced by the compacting axicon pair.

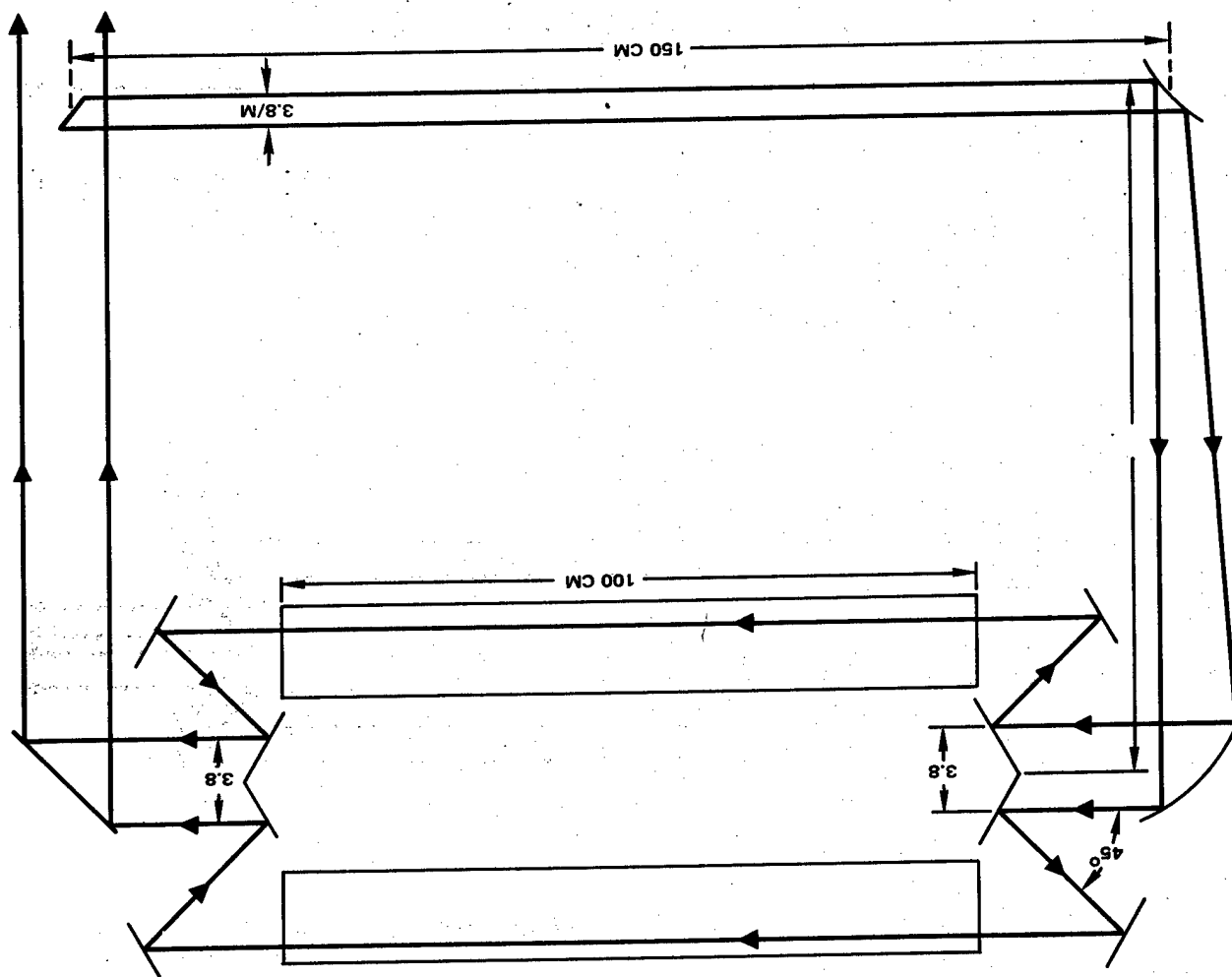


Figure 4-4. Ring resonator with circular beam of diameter 3.8 cm expanded and recompact by real axicons.  $M$  is the resonator magnification. The dimensions shown were used in all calculations except those whose results are shown in Figure 4-17.

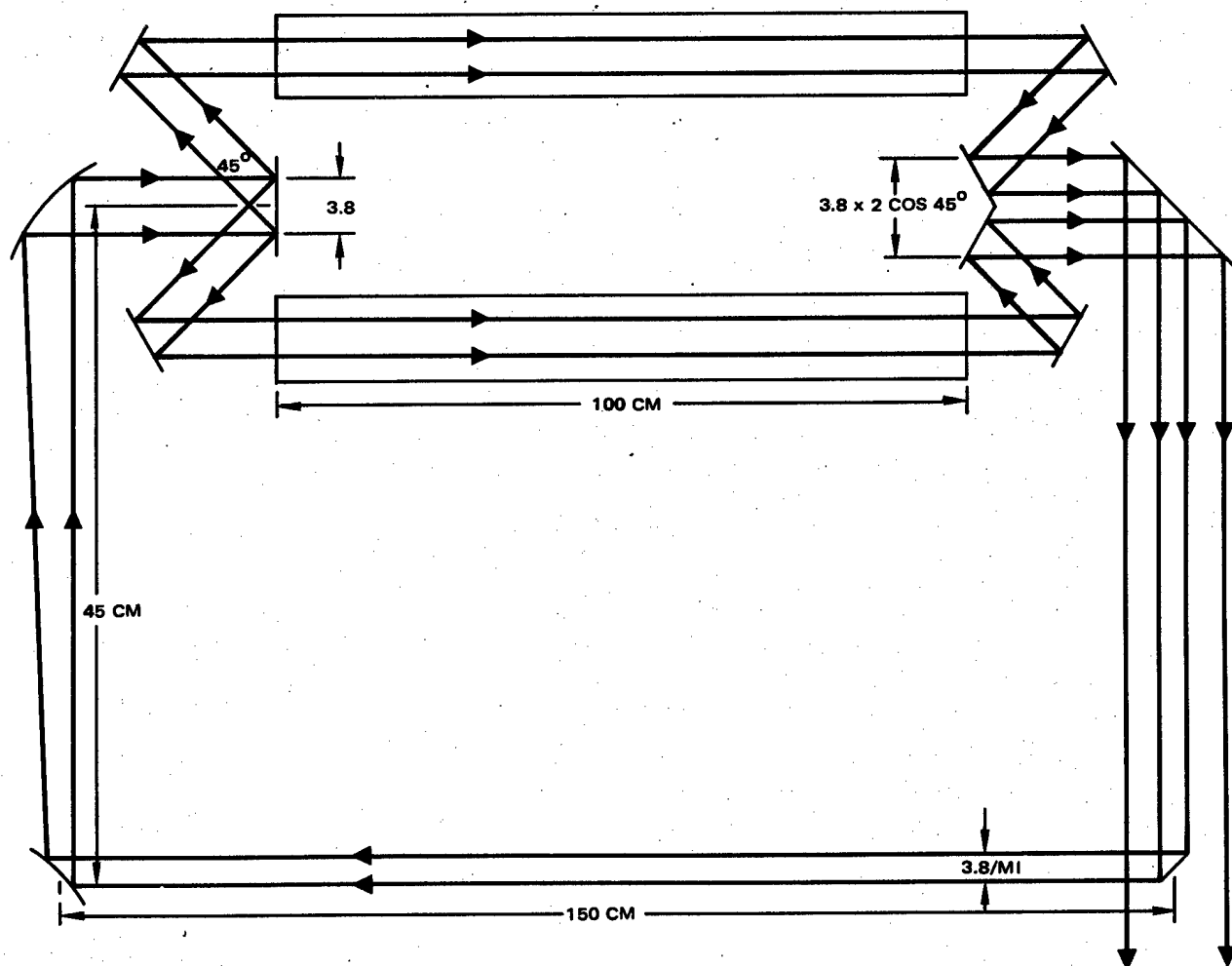


Figure 4-5. Ring resonator with circular beam of diameter 3.8 cm expanded and recompact by axicon elements. The inner element of the expander is a holographic grating axicon that splits the beam into two equal orders. After expansion and recompact, the beam is magnified by  $2 \cos 45^\circ$  in this configuration.  $M_1$  is the magnification of the resonator exclusive of the axicon magnification. Resonator magnification  $M = M_1 \times 2 \cos 45^\circ$ .

It is the axicon magnification that is fixed at 3.0 while  $M$ , the resonator magnification, which is related to outcoupling, is varied. For the HGA ring, there is a magnification in the beam from  $D$ , the input diameter, to  $2D\cos\theta$  at recompaction. For a given total resonator value of  $M$ , the magnification between feedback mirror and input to the expansion step is  $M/(2D\cos\theta)$ .

From a simple ray optics point of view, the all-geometric axicon ring resonator behaves like the usual unstable resonator. A ray that is  $\epsilon D/2$  ( $0 \leq \epsilon \leq 1$ ) from the beam axis as it approaches the expander tours the resonator until  $M^n \epsilon > 1$ , at which time it is outcoupled. The central filament ( $\epsilon = 0$ ) is the source of all rays. The HGA ring is quite different. Our typical ray-in-the-street at  $\epsilon D/2$  is split into two rays by the HGA. After two complete trips, as many as four rays may trace their paternity to it. Table 4-1 shows their locations.

TABLE 4-1. DAUGHTER RAYS IN HGA RING  
(Coordinates given as  $r, \phi$ )

Start	After One Trip	After Two Trips
$\epsilon D/2, \phi$	$1 \rightarrow D/2 \left[ \frac{M}{2} (1 + \epsilon) \right], \phi$ $2 \rightarrow D/2 \frac{M}{2} (1 - \epsilon), \phi - \pi$	$11 \rightarrow D/2 \left\{ \frac{M}{2} \left[ 1 + \frac{M}{2} (1 + \epsilon) \right] \right\}, \phi$ $12 \rightarrow D/2 \left\{ \frac{M}{2} \left[ 1 - \frac{M}{2} (1 + \epsilon) \right] \right\}, \phi - \pi$ $21 \rightarrow D/2 \left\{ \frac{M}{2} \left[ 1 + \frac{M}{2} (1 - \epsilon) \right] \right\}, \phi - \pi$ $22 \rightarrow D/2 \left\{ \frac{M}{2} \left[ 1 - \frac{M}{2} (1 - \epsilon) \right] \right\}, \phi$

Of course, depending upon  $\epsilon$  and  $M$ , some of these rays may not be in the resonator. Ray 22 will have returned to its source if

$$\epsilon = M/2 \left[ 1 - M/2 (1 - \epsilon) \right]$$

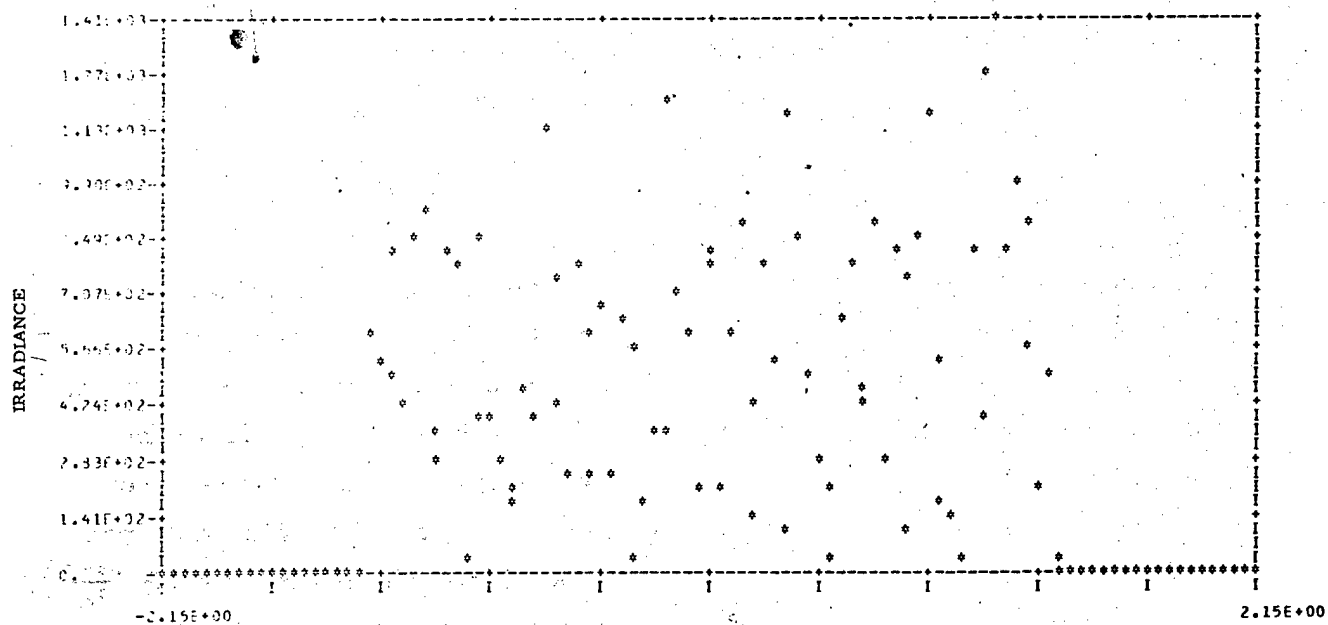
There are two solutions. For  $M = 2$ , ray 22 replicates the original ray for any  $\epsilon$ . For  $M \neq 2$ , the ring of rays at  $\epsilon = M/(M + 2)$  returns there upon alternate passes. That is, it returns in the sense that the 22 type offspring occupies the same position. A ray originally at distance  $\alpha D/2$  from the repeating ring will be  $(M/2)^2 \alpha D/2$  away from it after two iterations. For  $M > 2$ , rays diverge from the repeating ring, while for  $M < 2$  they collapse into it. In addition, for  $M > 2$ , the central portion of the beam,  $r < \frac{D}{2} \left( \frac{M-2}{M} \right)$ , is completely outcoupled on each pass. It therefore appears that for the HGA resonator,  $M=2$  is a boundary between different types of behavior. The case  $M=2$ , with all rays repeating, might somehow be special.

#### 4.4 ALIGNED RESULTS

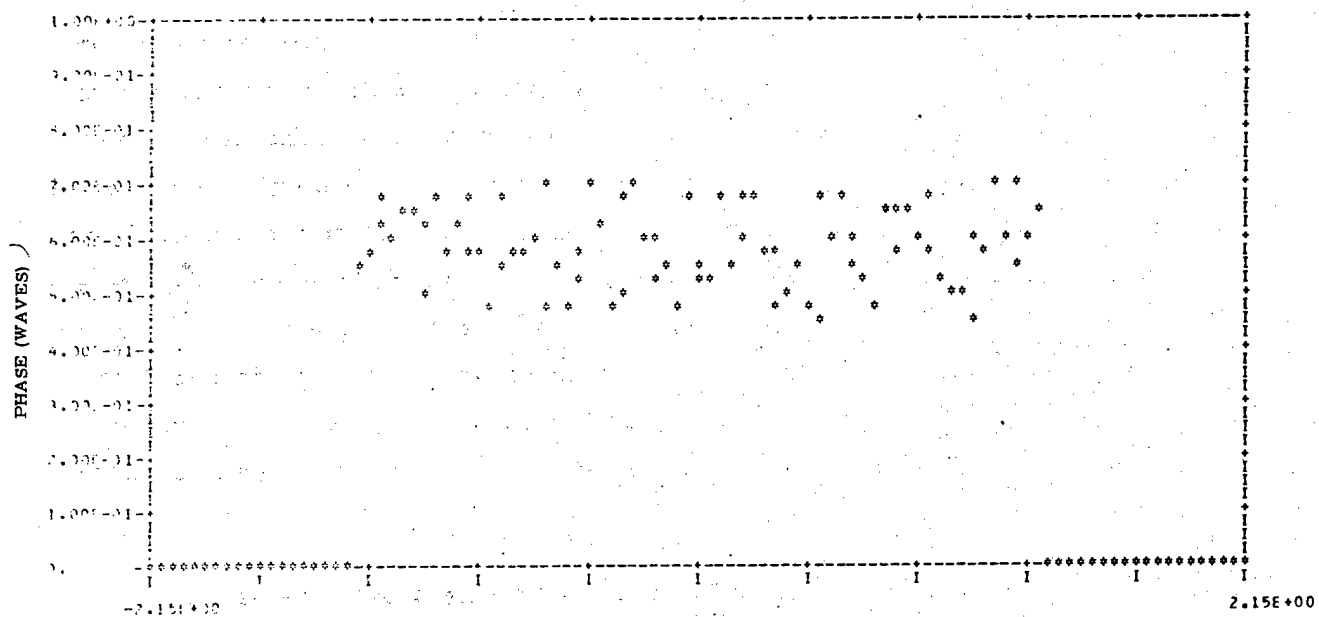
Numerical investigation was pursued for  $M = 1.4$ ,  $2.0$ , and  $2.8$  for both the HGA and all-geometric resonators, since  $M = 2.0$  seems likely to mark a division between different types of HGA resonator behavior. The all-real cases were carried to provide direct information about the effect of the HGA. A sufficient condition that a configuration will support a mode is that the mode be selected by the resonator from a random wave. Figure 4-6 displays line printer plot cross-sections of the starter wave used.\* Numbers produced by a so-called random number generator were taken in pairs to form complex field values  $(x + iy)$ . Intensity was then  $x^2 + y^2$  and phase  $\tan^{-1} (y/x)$ . Since all of the random numbers were between 0 and 1, phase

\*In this and all subsequent line printer plots, a line along one or both of the two coordinate directions ( $x$  and  $y$ ) transverse to the beam propagation direction ( $z$ ) is shown. If a plot is for example, along  $x$ , then  $y$  is fixed at the value of the grid point just below the beam center value. Beam center falls between two grid points and the lesser-valued one is chosen for plotting. When the plotting direction is not specified, cylindrical symmetry is implied.



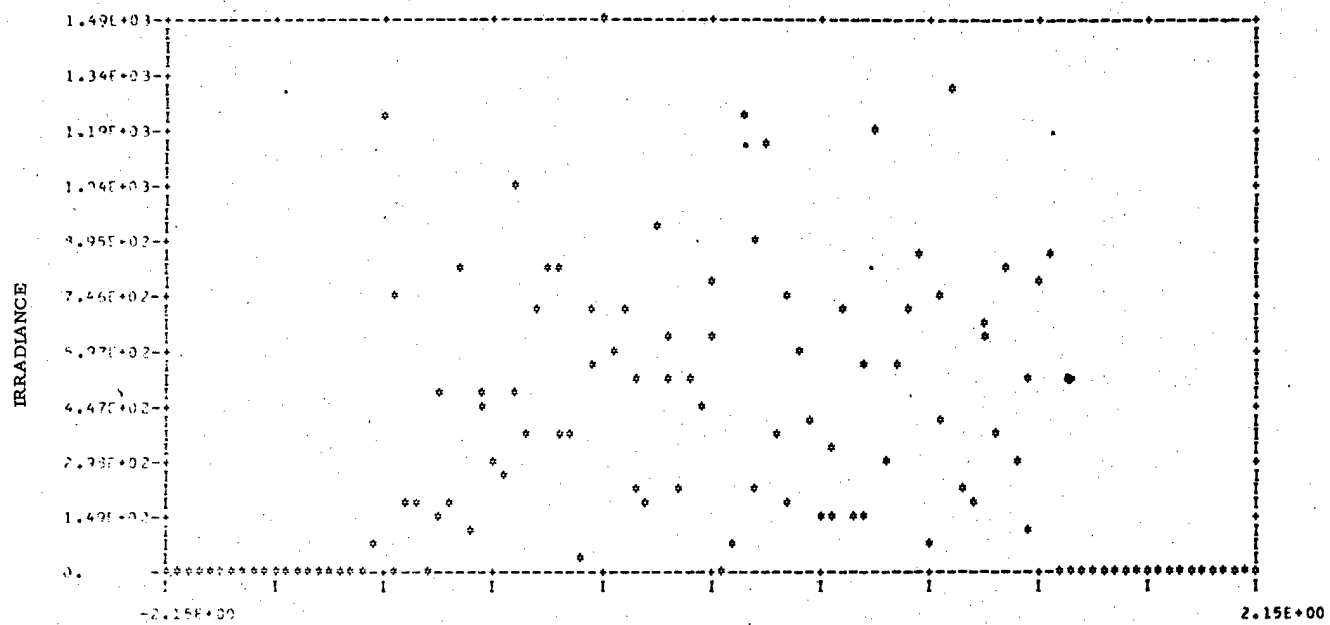


(a) Irradiance along x-direction.

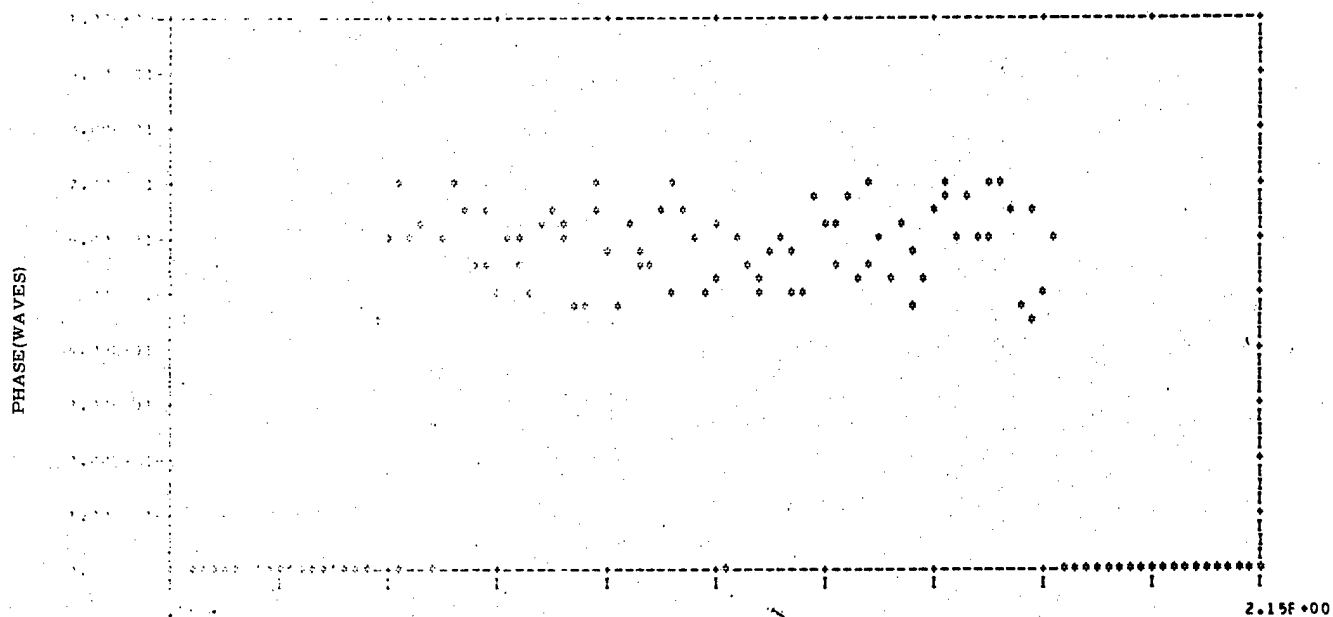


b) Phase along x-direction.

Figure 4-6. Phase and irradiance distributions in scrambled starter wave.



c) Irradiance along y-direction.



d) Phase along y-direction

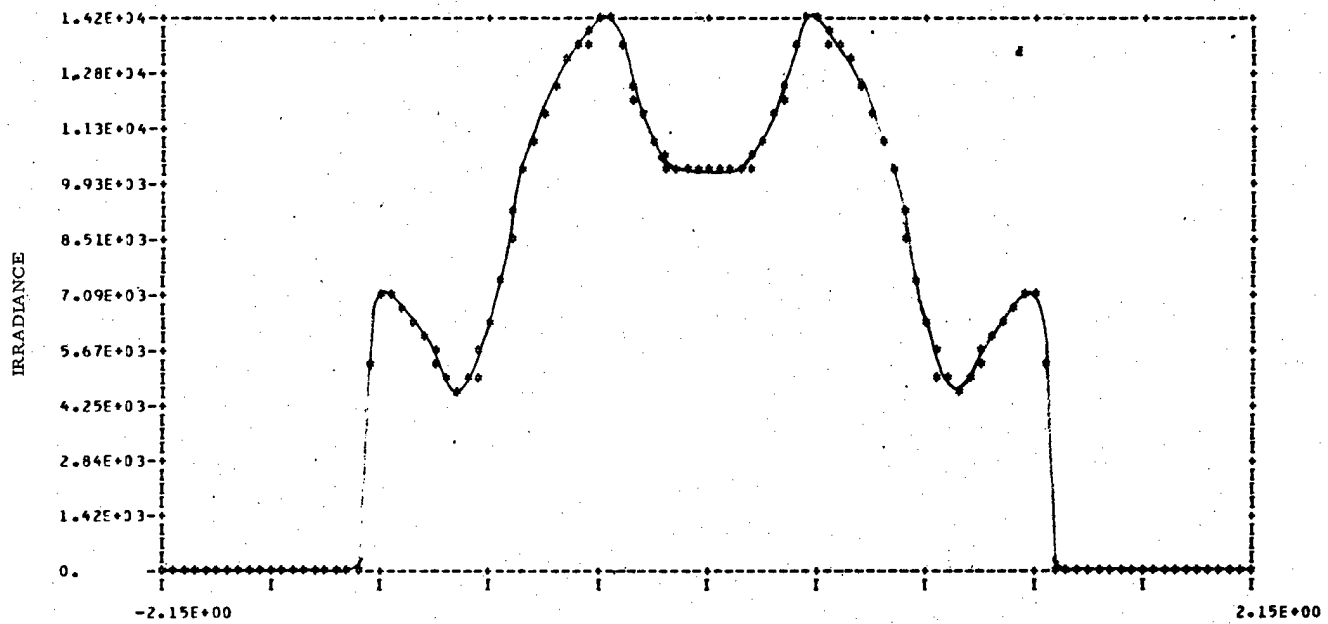
Figure 4-6. Phase and irradiance distributions in scrambled starter wave. (Continued)

varies over  $1/4$  wave. Intensity was renormalized to provide a specified total power in the starter beam.

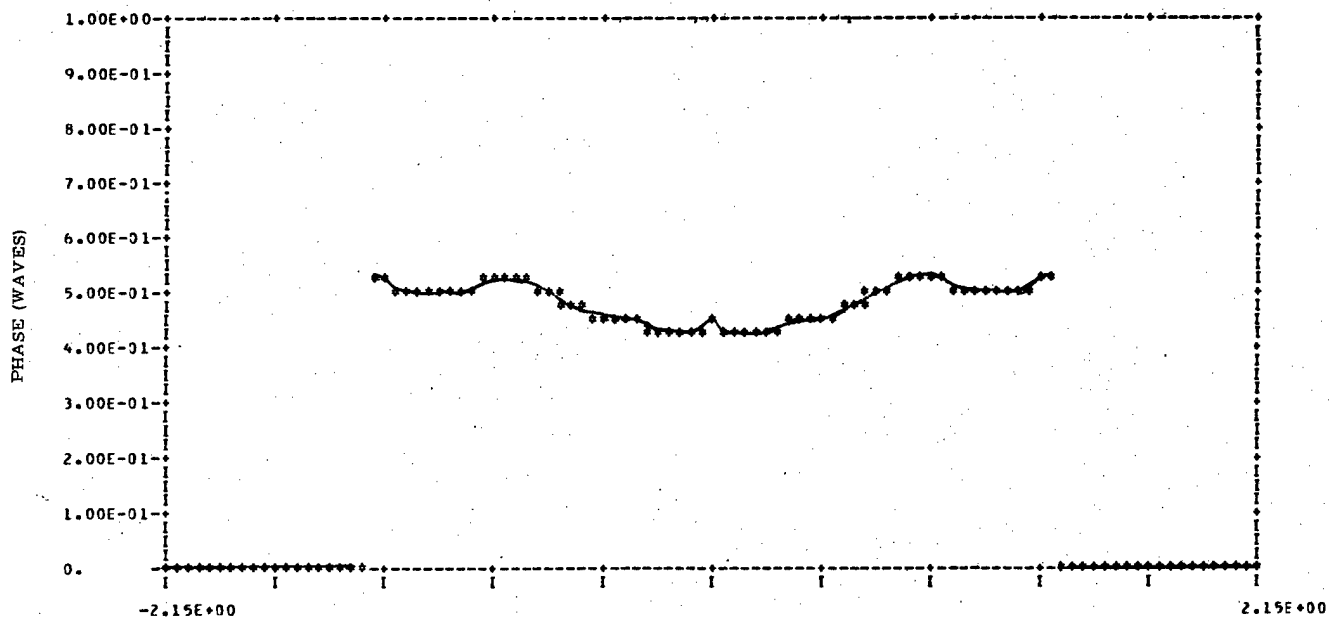
Figures 4-7 through 4-10 show the converged results at the feedback mirror achieved with the simple gain model included. All the geometric cases and the  $M = 1.4$  holographic case met this criterion. Figure 4-8 provides an example of what is meant by a converged solution. It displays two consecutive iterations obtained for the  $M = 2.0$  all-geometric resonator. Within the accuracy of a limited number of iterations, they are identical, a requirement that a solution to our steady-state code be meaningful. The HGA resonators with  $M = 2.0$  and  $2.8$  did not attain this state and, in fact, showed no apparent tendency toward convergence.

Lesser challenges were devised for the  $M \geq 2.0$  HGA rings. It was possible to reach steady state when a plane wave was used as the starter, but since the aligned resonators had azimuthal symmetry, a symmetric starter had no test of its discrimination against higher order azimuthal modes. Therefore a starter was used consisting of a wave of uniform amplitude  $1.0$  and phase  $0.0$  added to  $5$  percent of the wave shown in Figure 4-6 and, of course, renormalized. For  $M = 2.8$ , even an empty resonator so started failed to converge. At  $M = 2.0$ , the empty case reached the converged solution of Figure 4-11 from the perturbed start, but when gain was included, a rather close approach to the converged solution disintegrated upon carrying the calculation further, a fate illustrated in Figure 4-12.

A tentative conclusion is that the HGA resonator requires  $M < 2$  for stability, with  $M = 2$  a sort of marginal case. However, stability conclusions are tenuous when drawn from steady state modeling. For an empty resonator, the calculated non-converged wave does represent the evolution of a real wave — if the real wave ever takes the form of the initial starter. For a loaded resonator, the calculated non-converged wave represents no physical reality because the gain distribution for each iteration is calculated as if the optical wave of the previous iteration were the steady state solution. All a steady state model can say with certainty is that if an optical field distribution replicates itself, that distribution is a steady state solution.

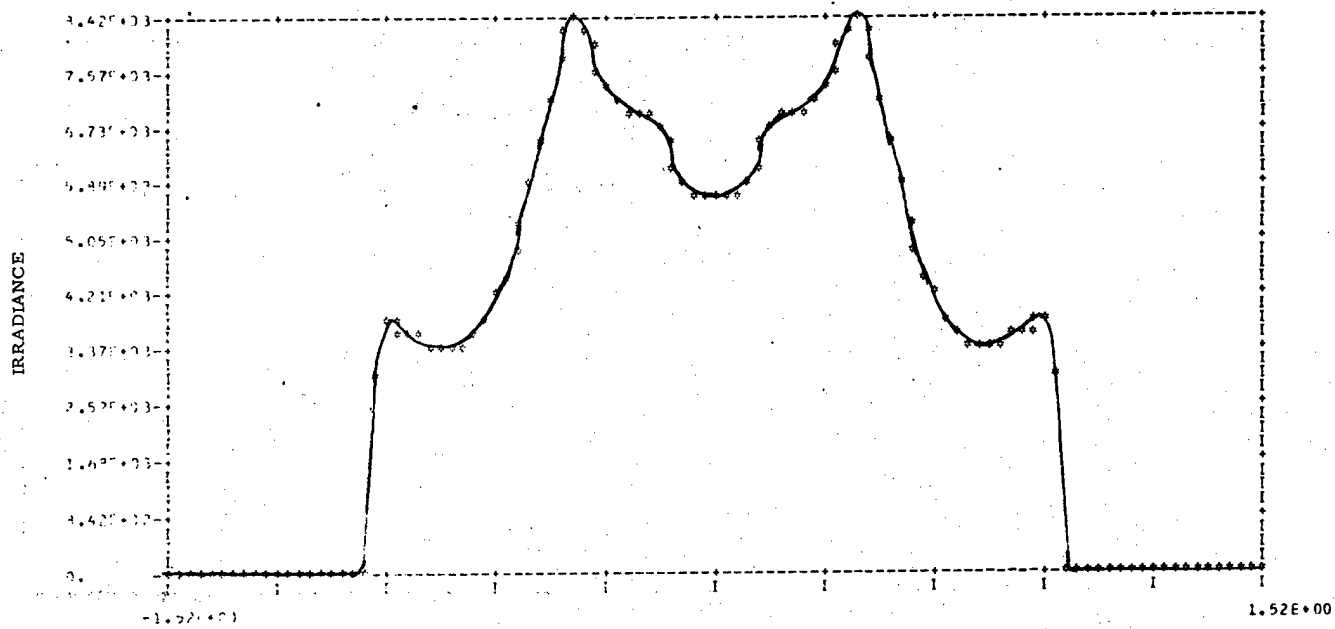


a) Irradiance.

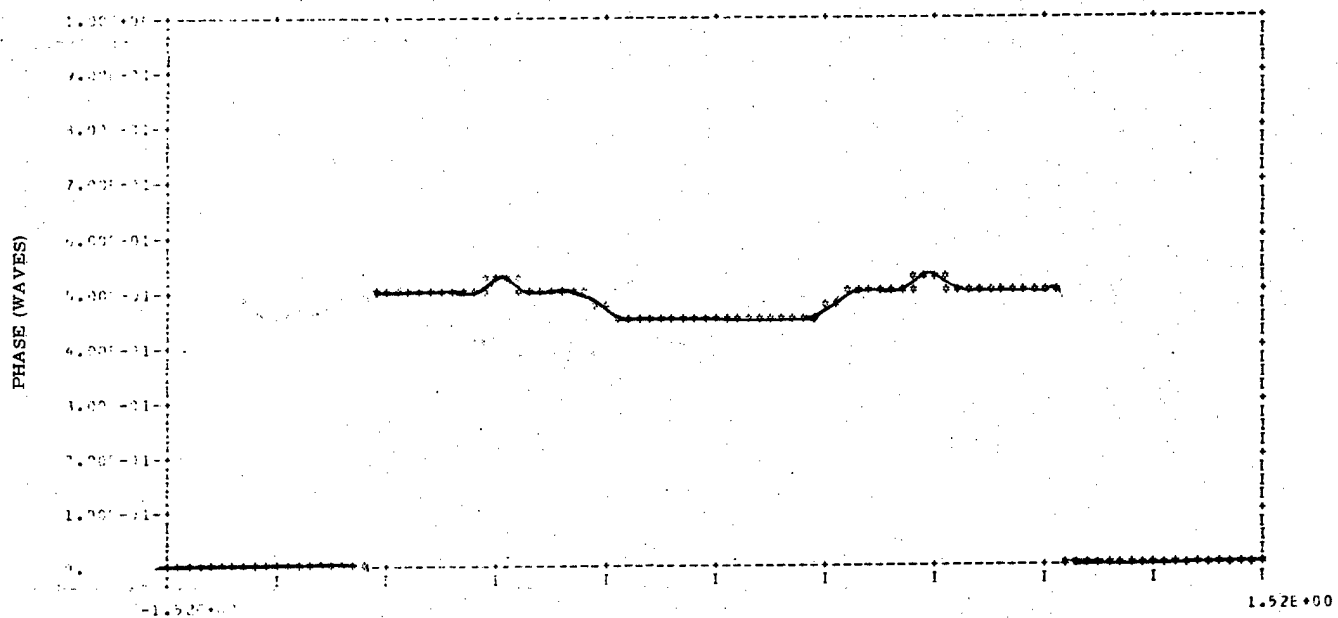


b) Phase.

Figure 4-7. Phase and irradiance distributions at feedback mirrors for  $M = 1.4$ , all-geometric resonator.

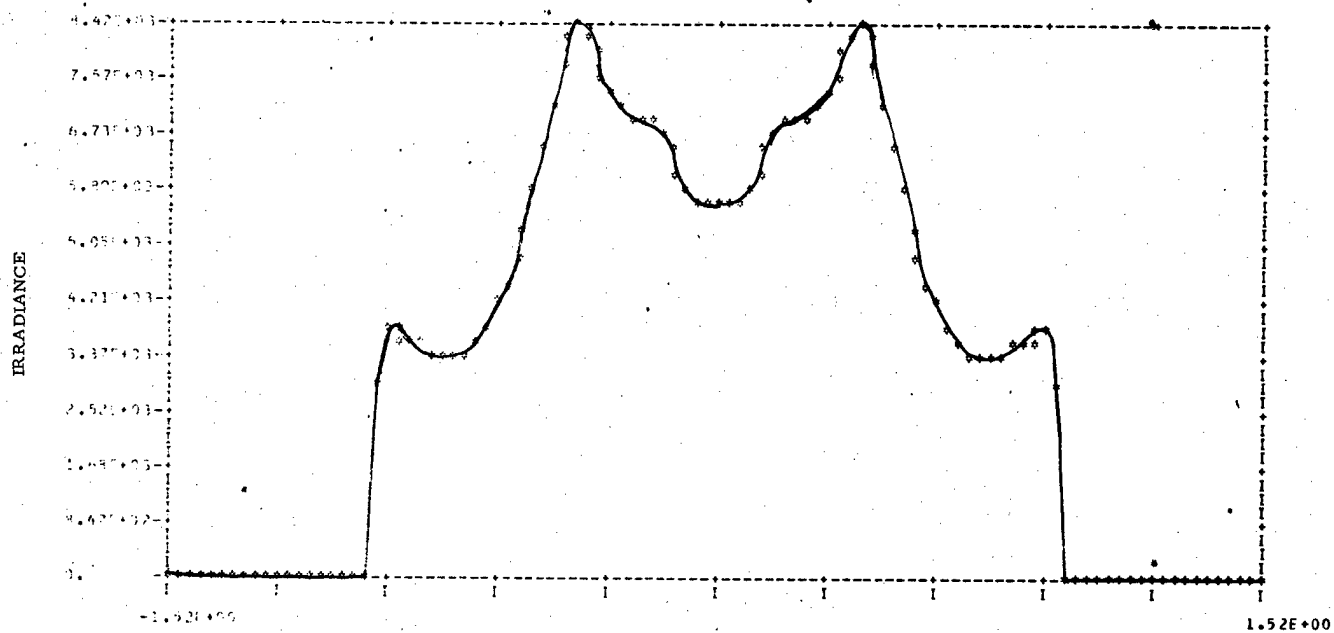


a) Irradiance at penultimate iteration.

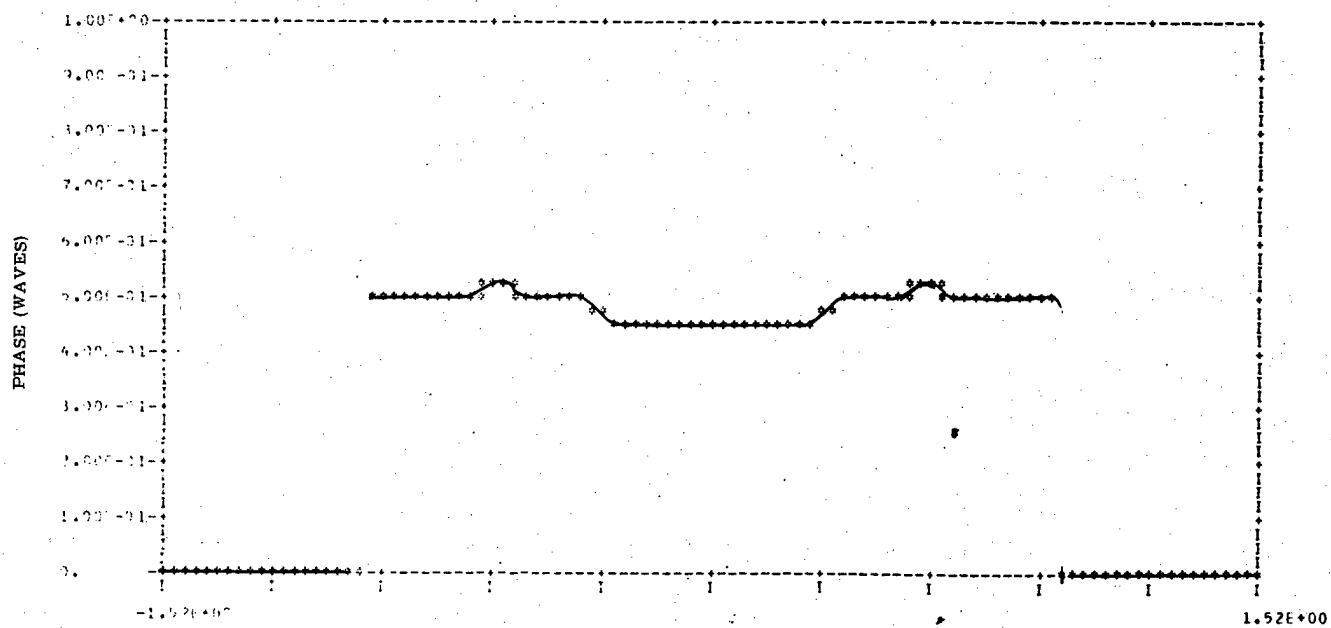


b) Phase at penultimate iteration.

Figure 4-8. Phase and irradiance distribution at feedback mirror for  $M = 2.0$ , all geometric resonator.

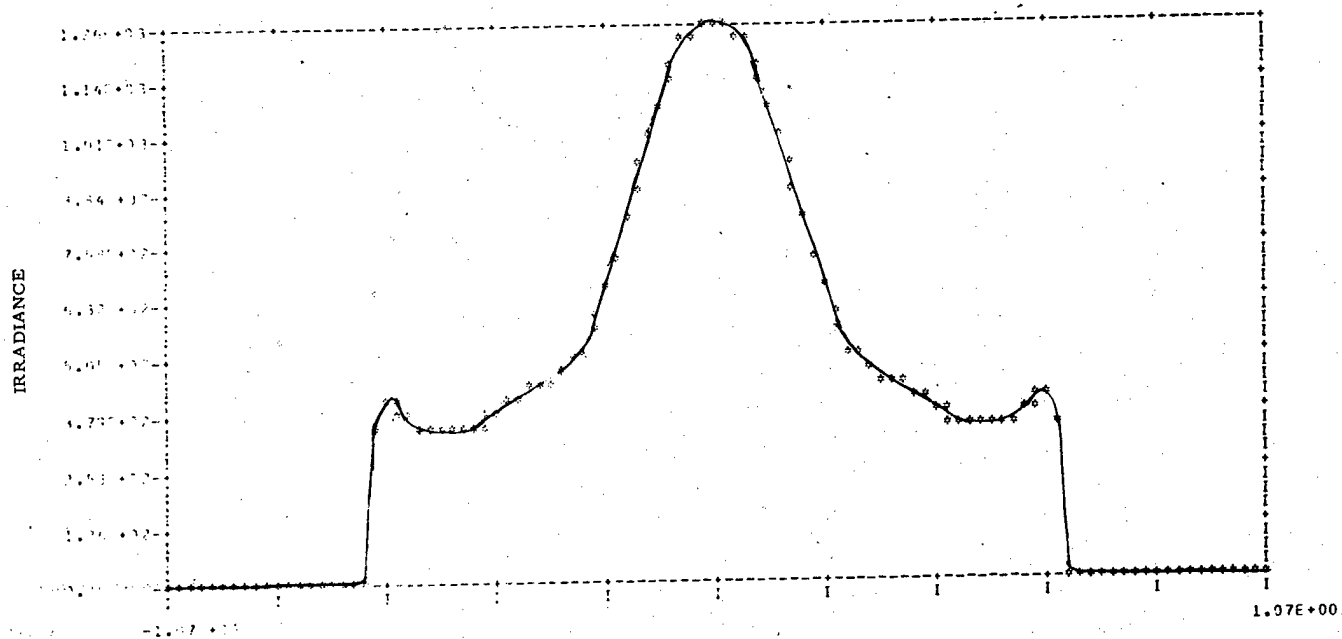


c) Irradiance at final iteration.

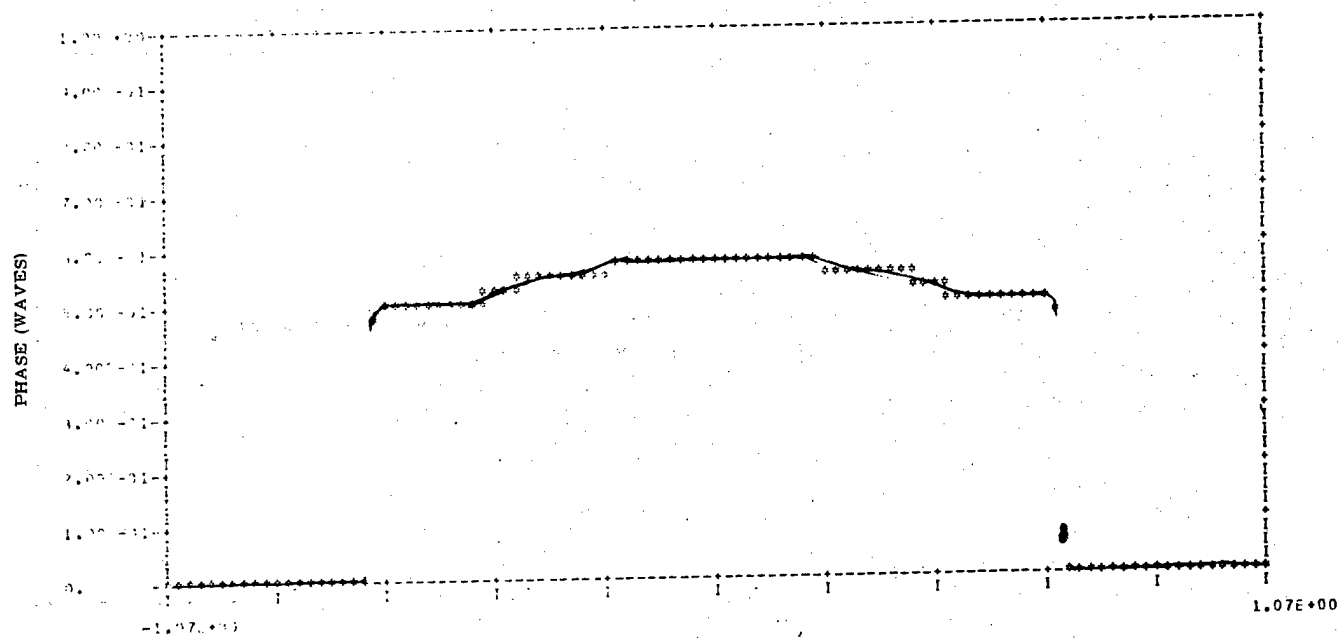


d) Phase at final iteration.

Figure 4-8. Phase and irradiance distribution at feedback mirror for  $M = 2.0$ , all geometric resonator. (Continued)

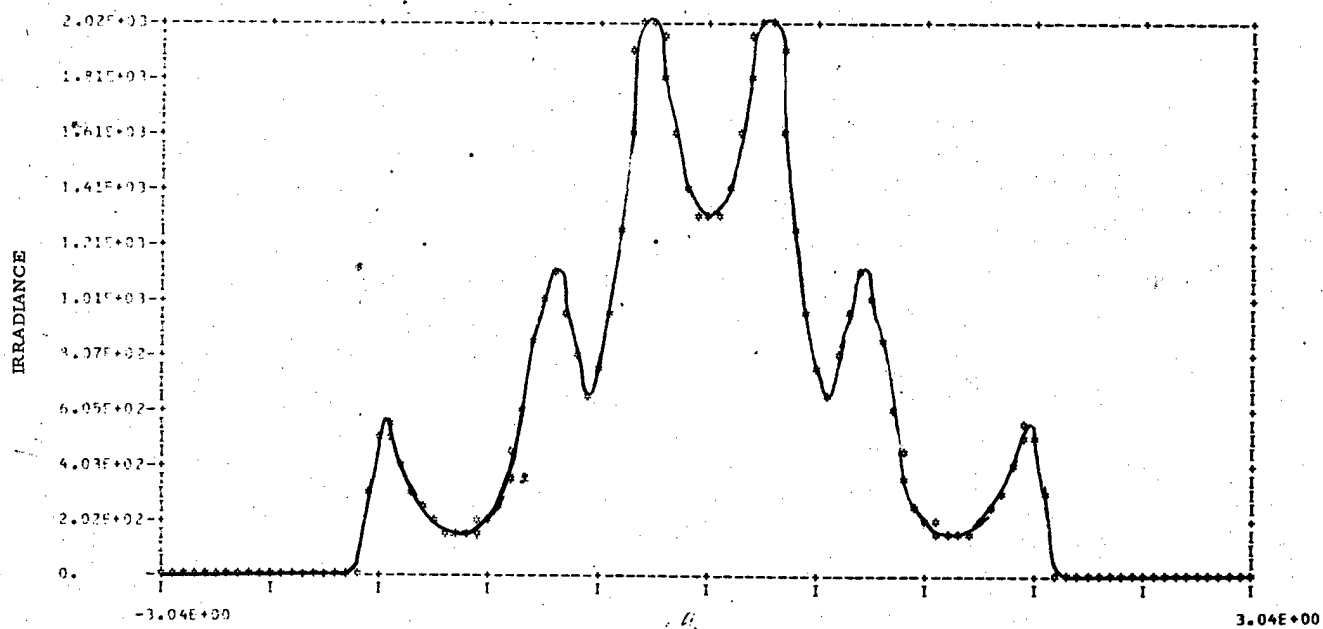


a) Irradiance

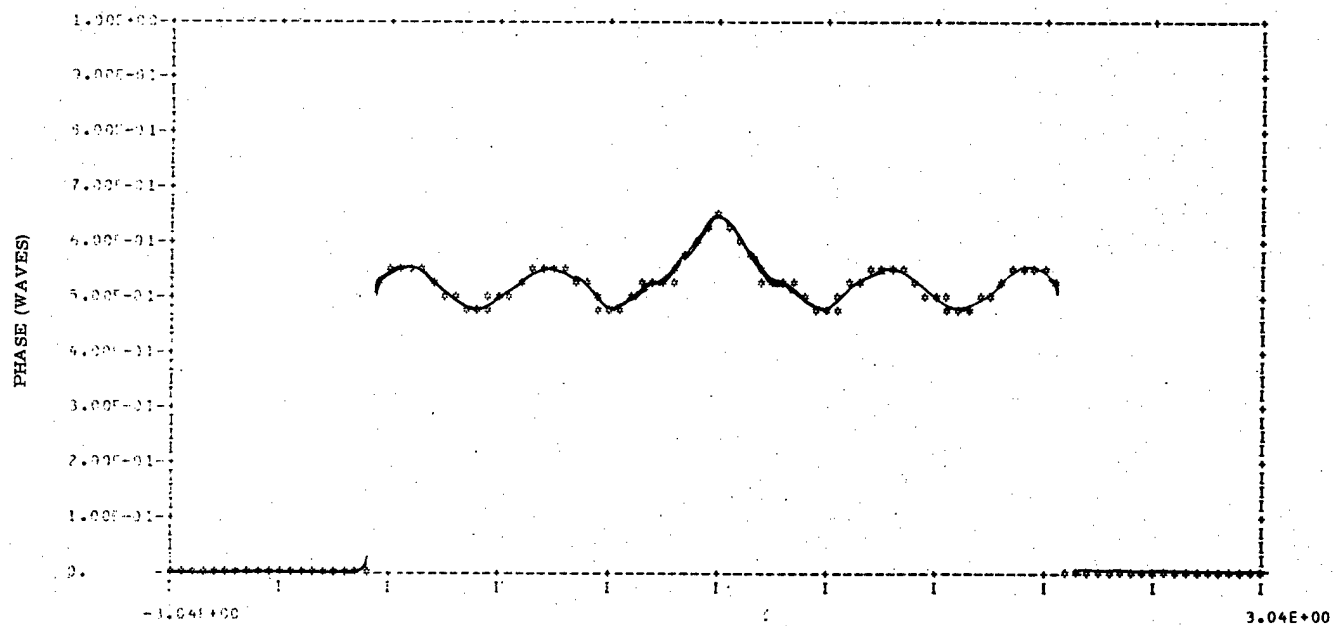


b) Phase

Figure 4-9. Phase and irradiance distribution at feedback mirror for  $M = 2.8$ , all geometric resonator.



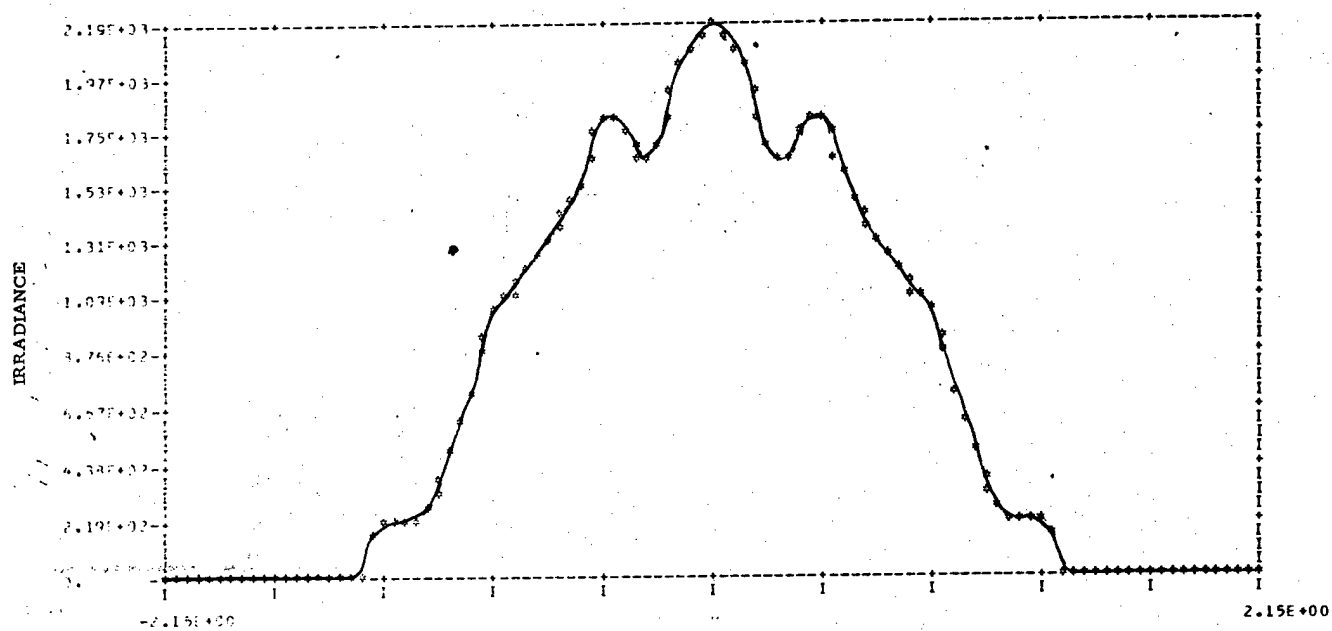
a) Irradiance



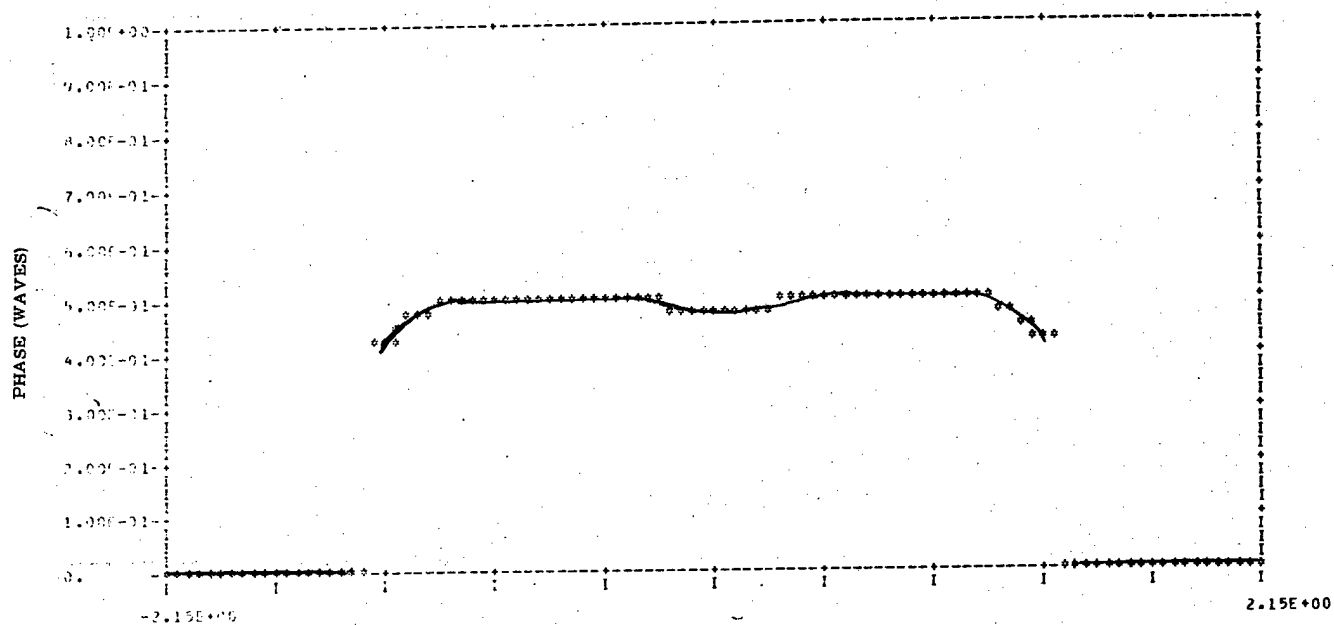
b) Phase

Figure 4-10. Phase and irradiance distribution at feedback mirror for  $M = 1.4$ , holographic axicon resonator.



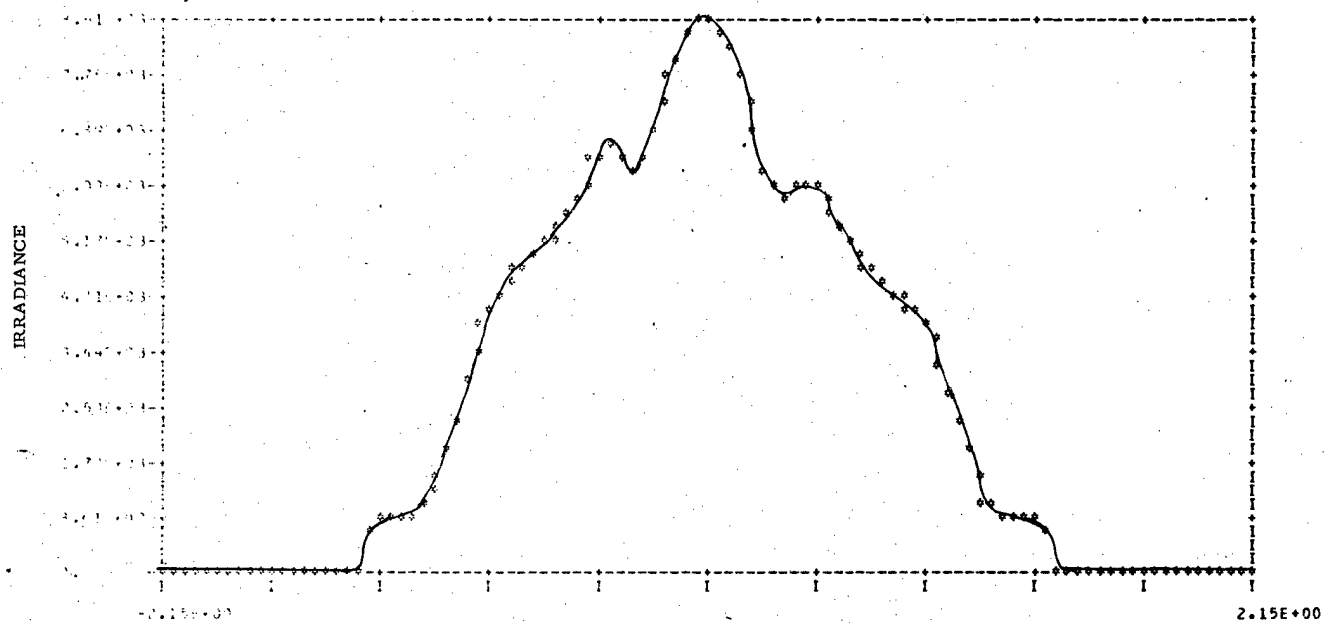


a) Irradiance

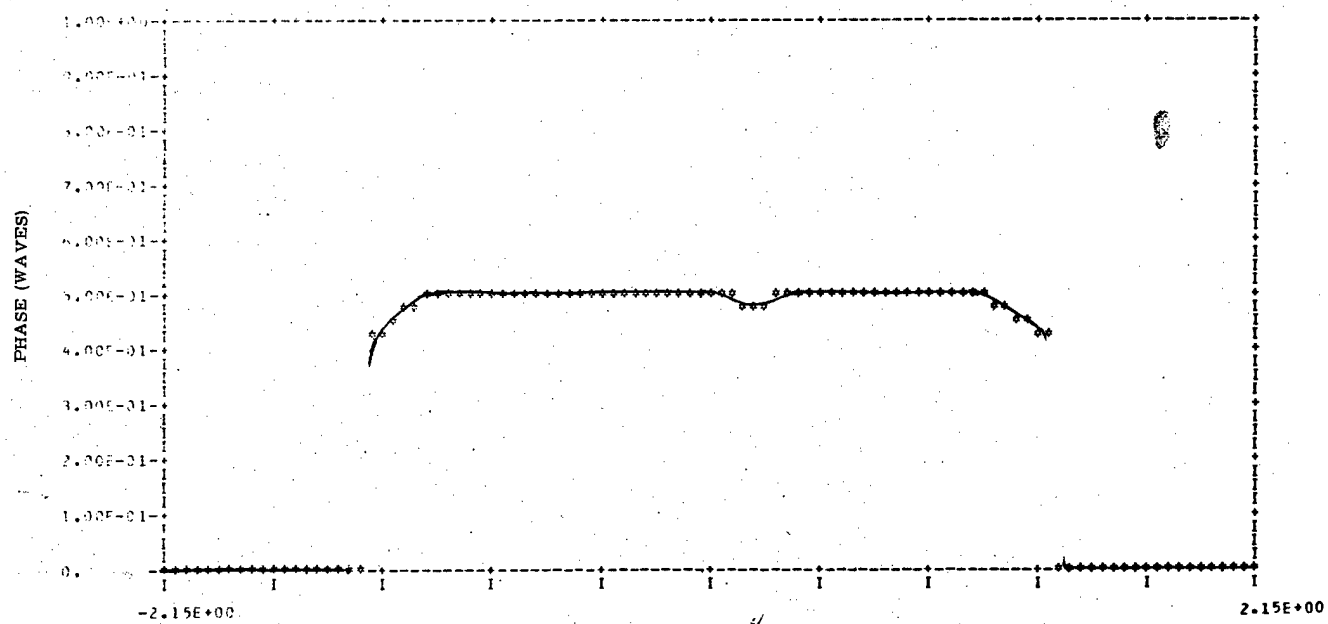


b) Phase

Figure 4-11. Phase and irradiance distribution at feedback mirror for  $M = 2.0$ , holographic axicon resonator with no gain.

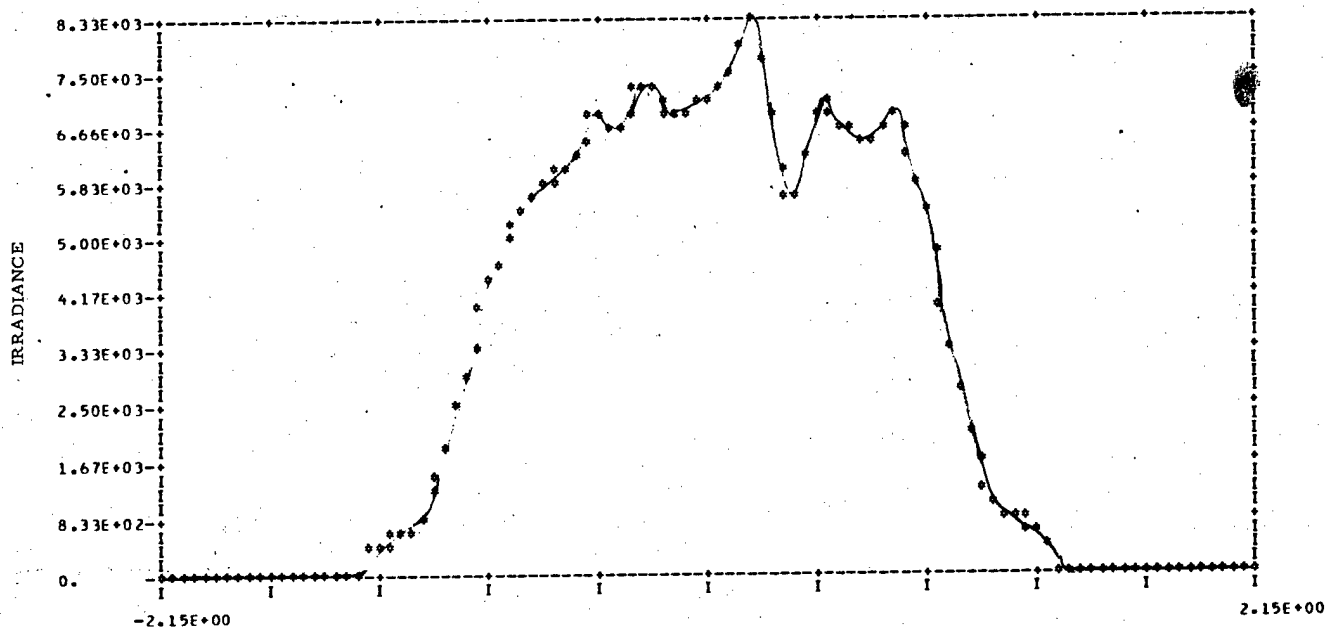


a) Irradiance after 60 iterations.

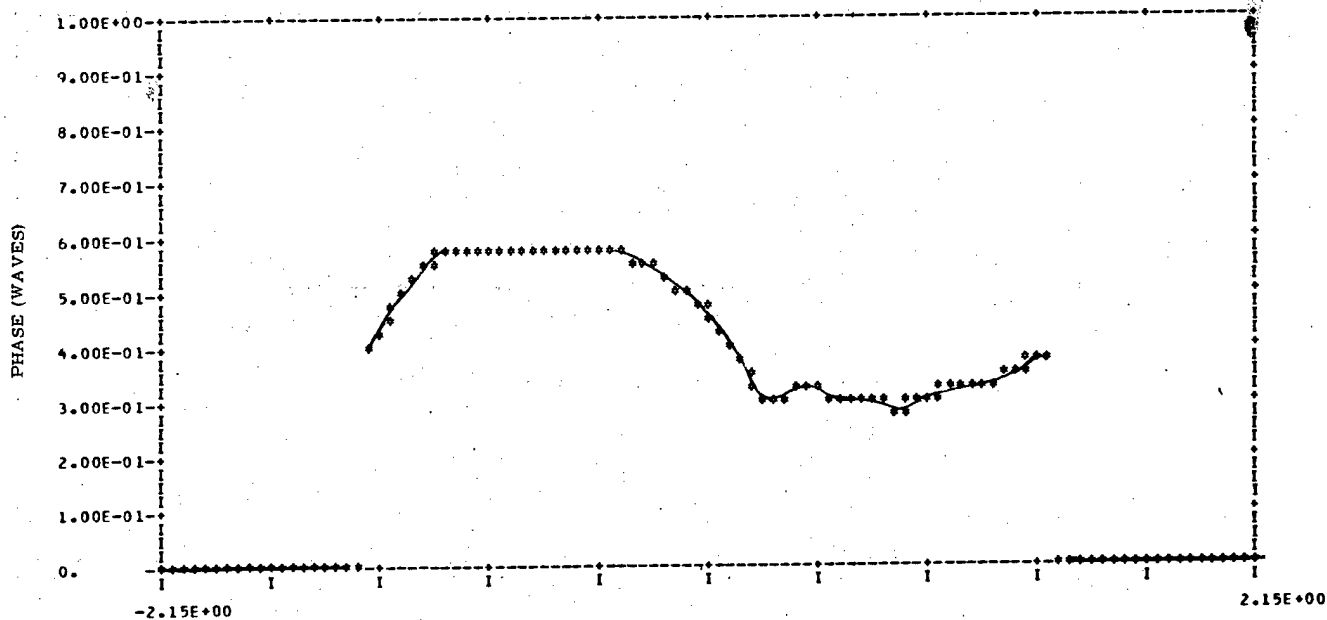


b) Phase after 60 iterations.

Figure 4-12. Phase and irradiance distribution at feedback mirror for  $M = 2.0$ , holographic axicon resonator with gain.



c) Irradiance after 120 iterations.



d) Phase after 120 iterations.

Figure 4-12. Phase and irradiance distribution at feedback mirror for  $M = 2.0$ , holographic axicon resonator with gain. (Continued)

As expected, variation of magnification does not result in such qualitative variation in calculated resonator performance for the all-geometric arrangements. Phase and intensity distributions vary among them, but not enough to make each case individually interesting. Therefore, subsequent sections will not include graphical displays of results for all three geometric cases when one representative seems sufficient.

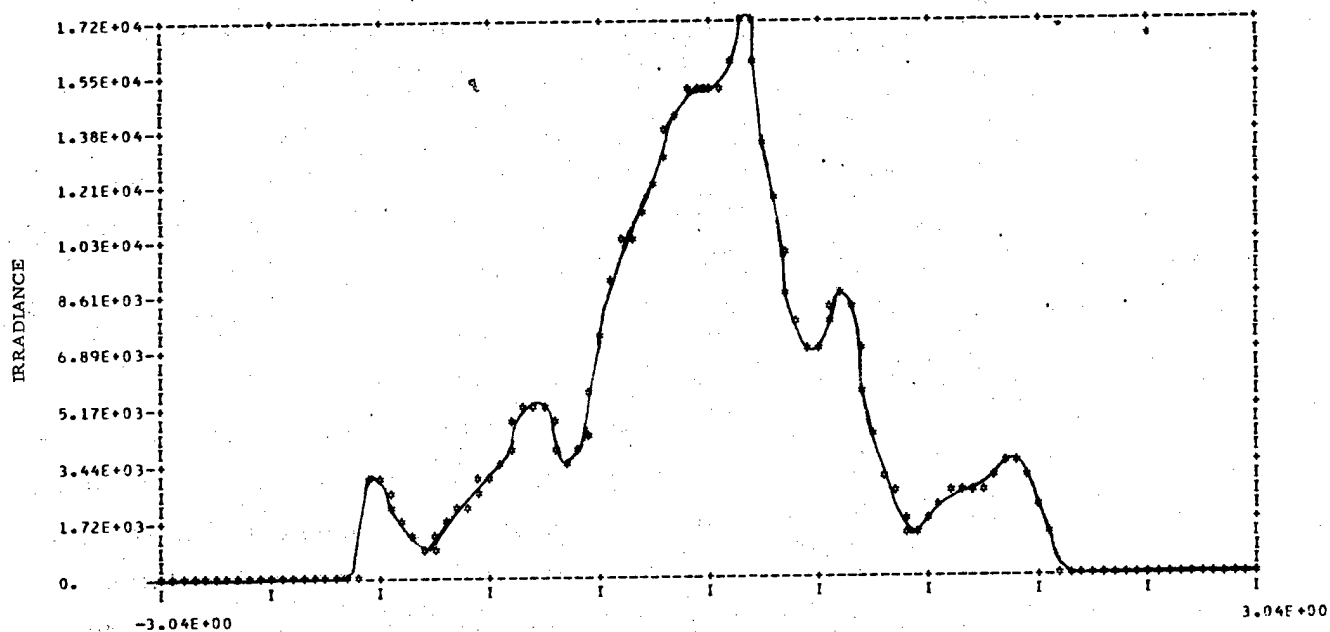
#### 4.5 MISALIGNED RESONATORS

It has been suggested that resonators containing axicons are particularly sensitive to misalignments. For example, Mumada et al. (1977)\* state that, in their experiments, beam quality improvement that occurred when a hollow corner reflector was added was due to its compensating for phase discontinuity induced by their axicon in a tilted wave front. We therefore studied the impact upon our resonator models caused by noncolinearity of beam and axicon axes. The effect of a non-zero angle between these axes was investigated by imposing a 100 microradian tilt upon the wave at the mirror immediately preceding the expander (see Figures 4-4 and 4-5). This is about the size of an alignment error of this sort that one would encounter in a device. Figures 4-13 and 4-14 show the resulting feedback beams for the  $M = 1.4$  HGA and the  $M = 2.0$  geometric rings. The resonator containing the holographic element has a steeper phase tilt than does the  $M = 2.0$  all-real ring, but much of this is due to the fact that the larger outcoupling results in a smaller portion of the wave being fed back and magnified. The  $M = 2.8$  geometric case resulted in a wave at output with about one-half the tilt of the  $M = 2.0$  model. The lowest outcoupling geometric case ( $M = 1.4$ ) failed to converge with 100 microradians of tilt.

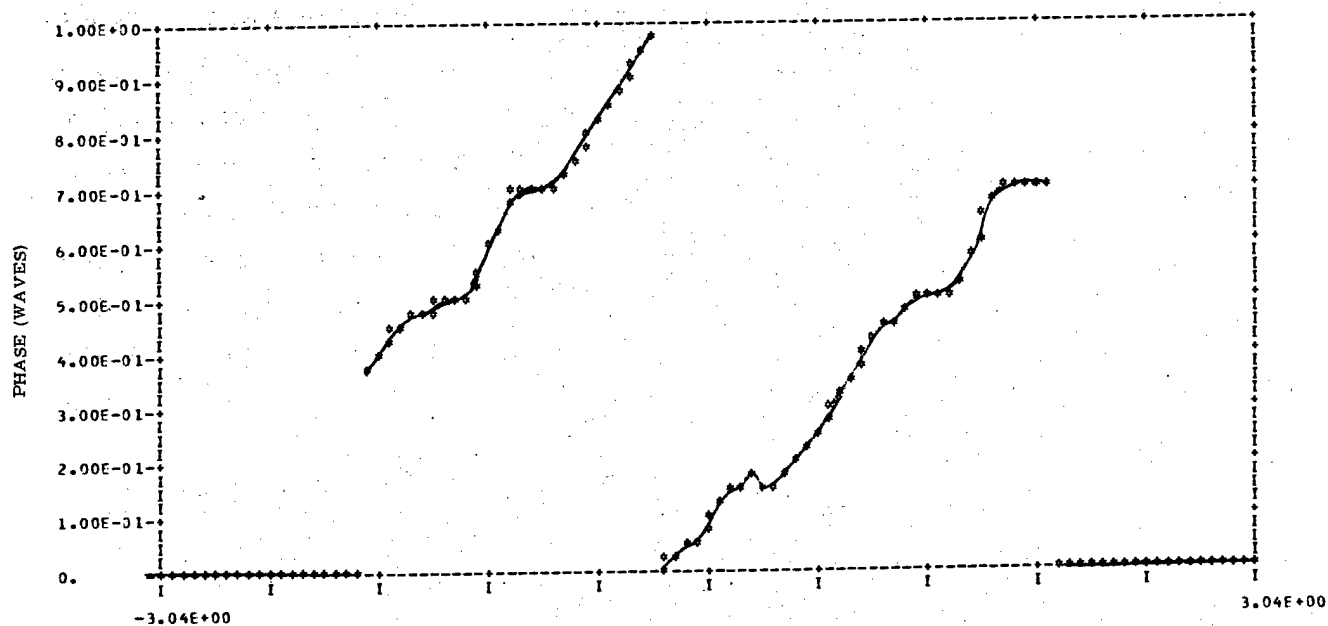
A rather clear advantage for the holographic expander appeared when the beam axis and that of the inner element of the expander were parallel but displaced from one another. The HGA ring converged for the largest offset tested, namely  $10^{-4}$  cm (about 0.1 wavelength), while the all-real cases could sustain only about one-half this decentering with their dignity intact.

---

\*Mumola, P. B. et al., Unstable Resonators for Annular Gain Volume Lasers, Appl. Opt., 17, 236-243 (1978)

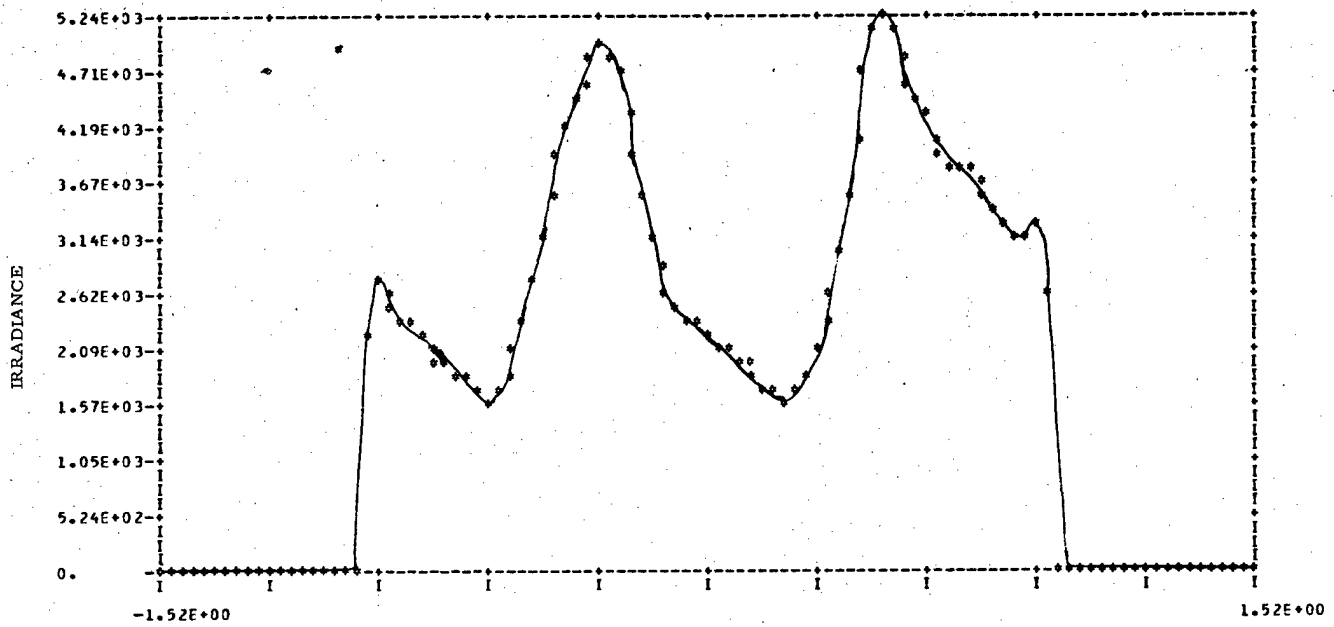


a) Irradiance

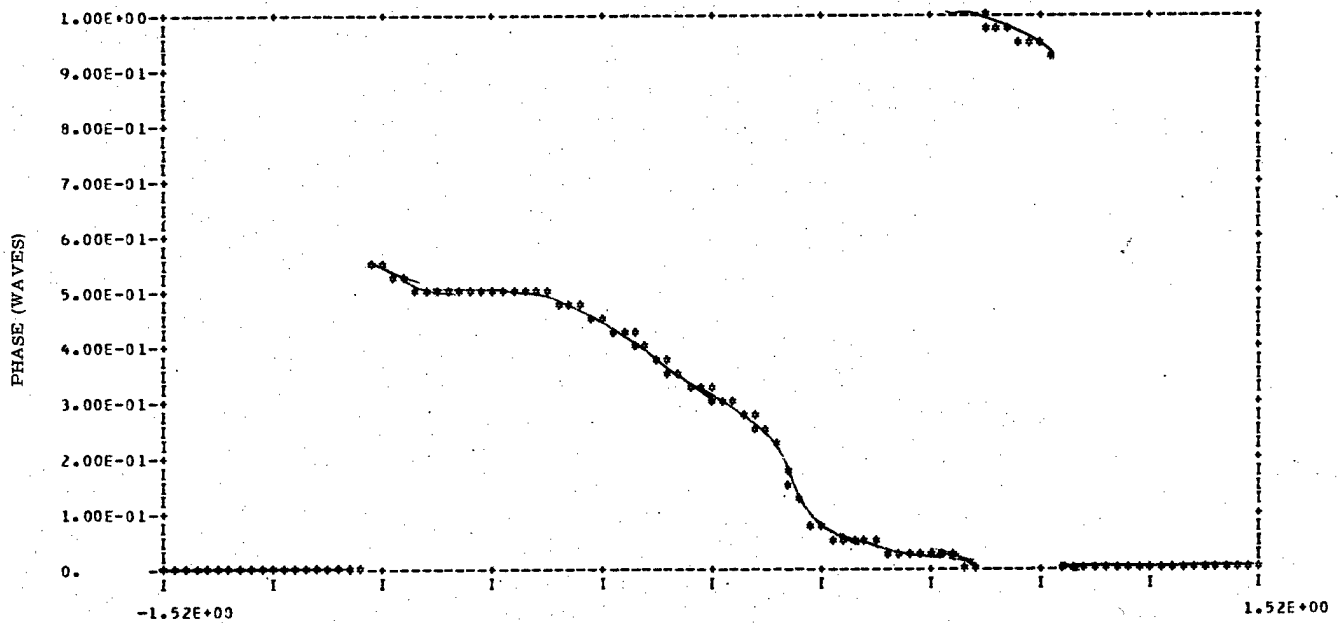


b) Phase. The apparent one wave discontinuity is only a plotting convenience. The phase is plotted modulo (one wave).

Figure 4-13. Phase and irradiance distribution at feedback mirror for  $M = 1.4$ , holographic axicon resonator, along direction of 100 microradian tilt.



a) Irradiance



b) Phase. The apparent one wave discontinuity is only a plotting convenience. The phase is plotted modulo (one wave).

Figure 4-14. Phase and irradiance distribution at feedback mirror for  $M = 2.0$ , all-geometric axicon resonator, along direction of 100 microradian tilt.

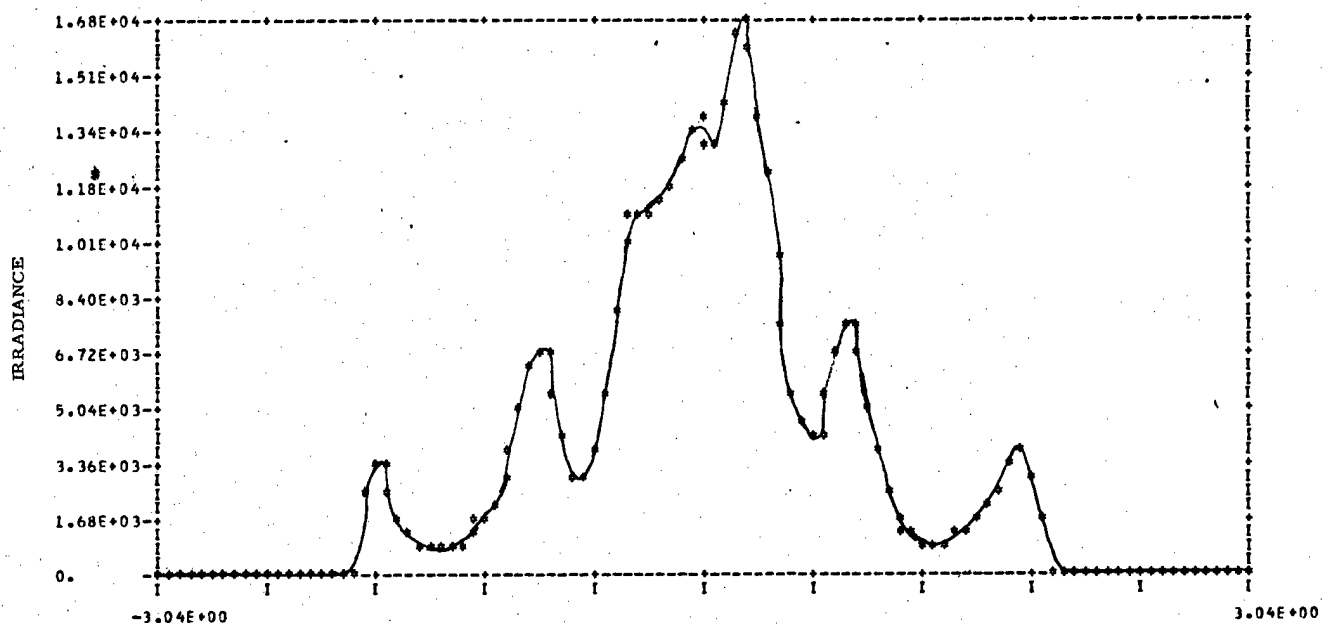
The mixing character of the HGA resulted in a wave front with considerably less tilt than that found in an all-geometric resonator with one-half as much decentration of the inner cone of the expander. Figures 4-15 and 4-16 illustrate this point.

#### 4.6 LENGTH VARIATION AND SAMPLING RATE

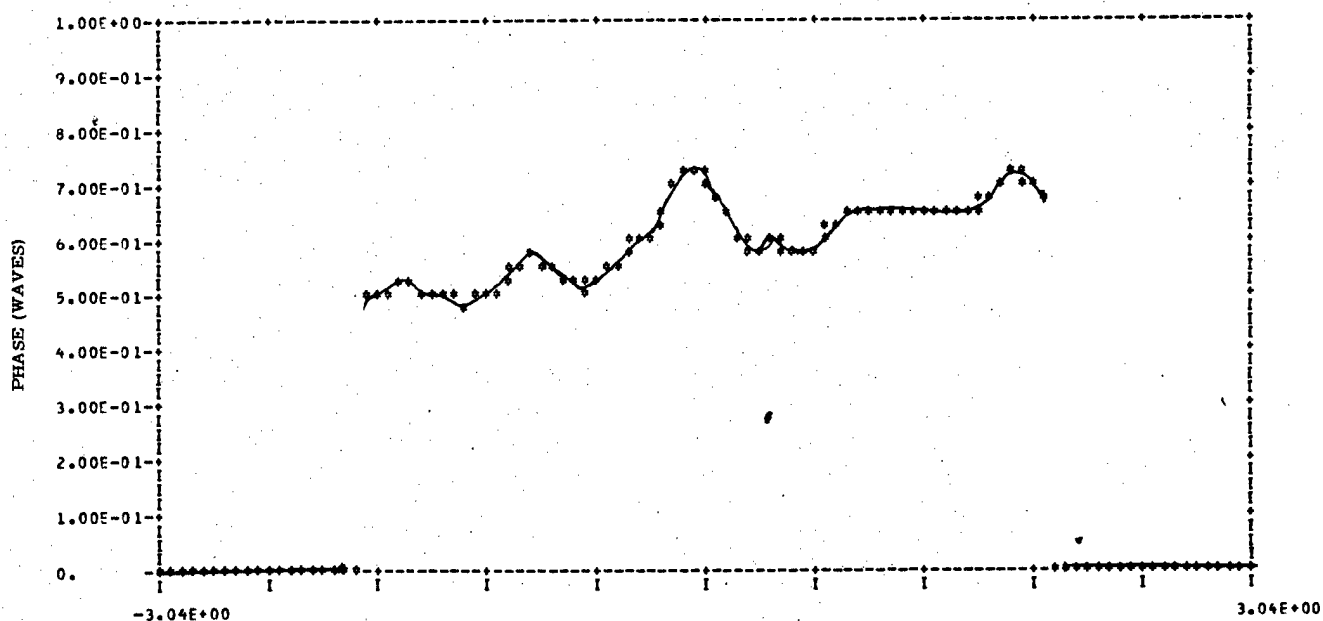
The above results were obtained for a model with a compacted beam path length of 308 cm, by no means an unreasonably long value. Considerable attention has been devoted to the requirements on this dimension that an axicon expansion and contraction places upon the system, and so we briefly investigated a similar ring but with a compacted length of only 130 cm. The converged solution of Figure 4-17 differs in some particulars from the comparable longer case (Figure 4-6). Apparently operation with rather short compacted lengths is quite feasible

In criticizing any numerical study, one has available a nearly free shot at the sampling interval. Was it sufficient to include the important phenomena? Since axicon resonators are insufficiently well understood to permit calculation of a necessary grid point density, we cannot say whether our choice of a 128 by 128 point mesh is insufficient, excessive, or optimal. An obvious check is to increase the sampling rate in a particular case to 256 x 256 points and compare the result to the corresponding 128 by 128 case.

When Figure 4-18 is compared to Figure 4-8, it is seen that the principle result of increasing the number of grid points is to alter the intensity and phase curves somewhat near the center of the beam. This is the portion of the beam reflected from the tip of the inner axicon of the compactor, and if a beam were actually compacted with no central hole at all, there would be a central singularity. It is the finite size of the grid boxes that avoids that difficulty in the calculations. In an experiment, a central hole would be required to avoid incinerating the axicon's tip. The detailed structure in the center of Figures 4-8 and 4-18 is therefore not terribly significant. Since the recomputed beam in such a resonator would leave the inner axicon with a hole at least as large as the coarser mesh grid box, the finer mesh does not improve the model in this region. In the rest of the beam, the curves are very similar. A four-fold increase in computation time would apparently not be worthwhile.



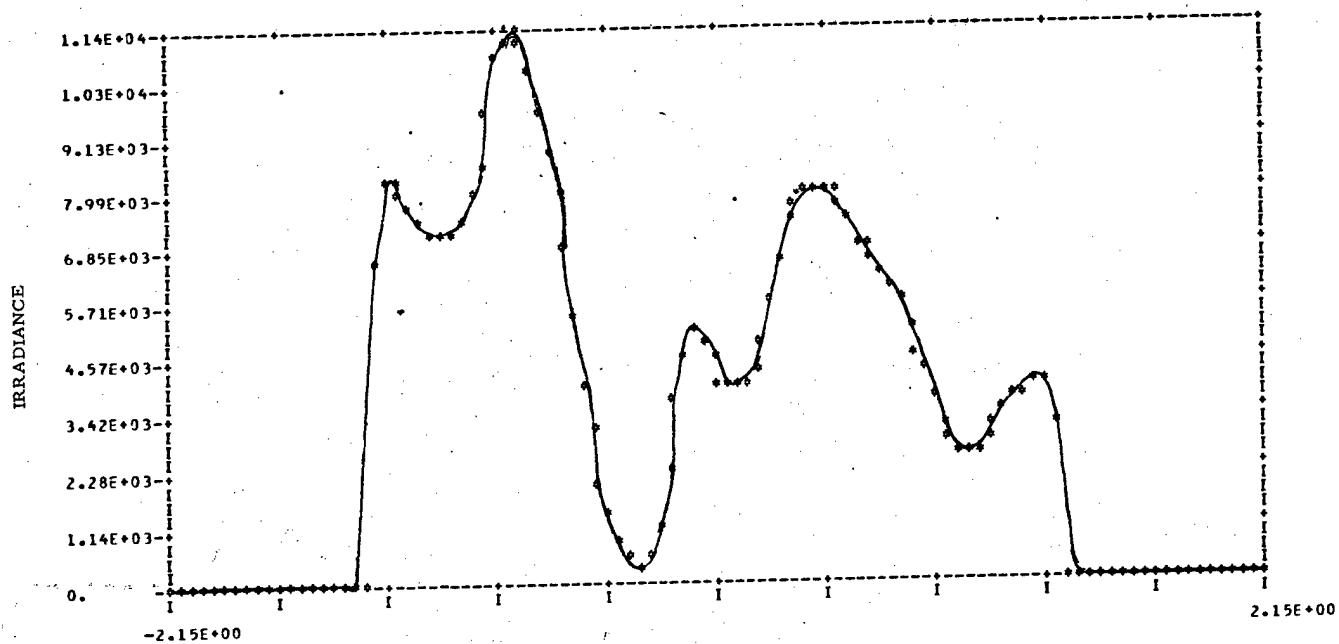
a) Irradiance



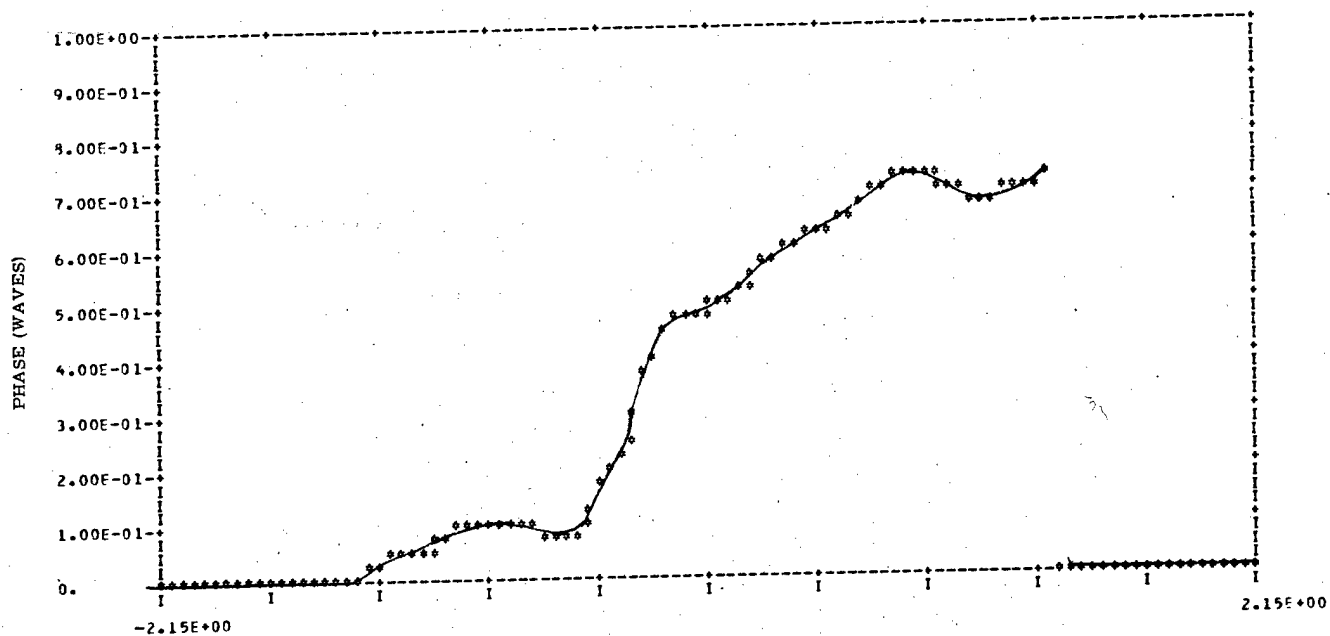
b) Phase

Figure 4-15. Phase and irradiance distribution at feedback mirror for  $M = 1.4$ , holographic axicon resonator, along direction of  $10^{-4}$  cm offset.



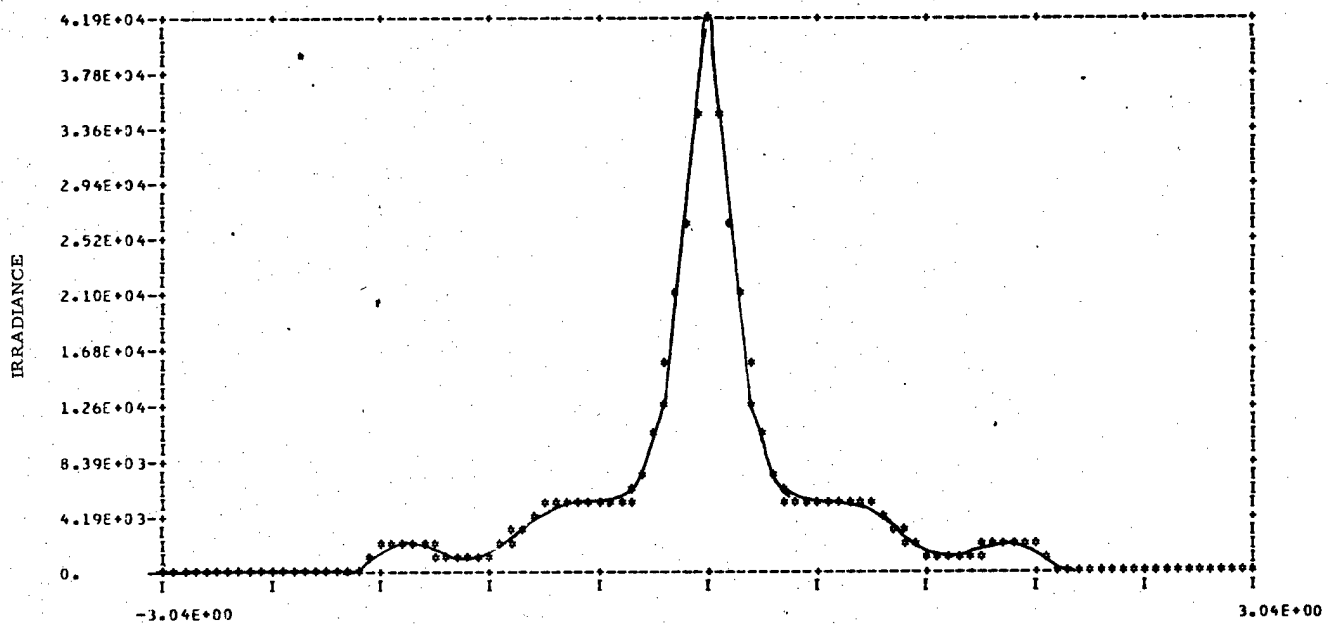


a) Irradiance

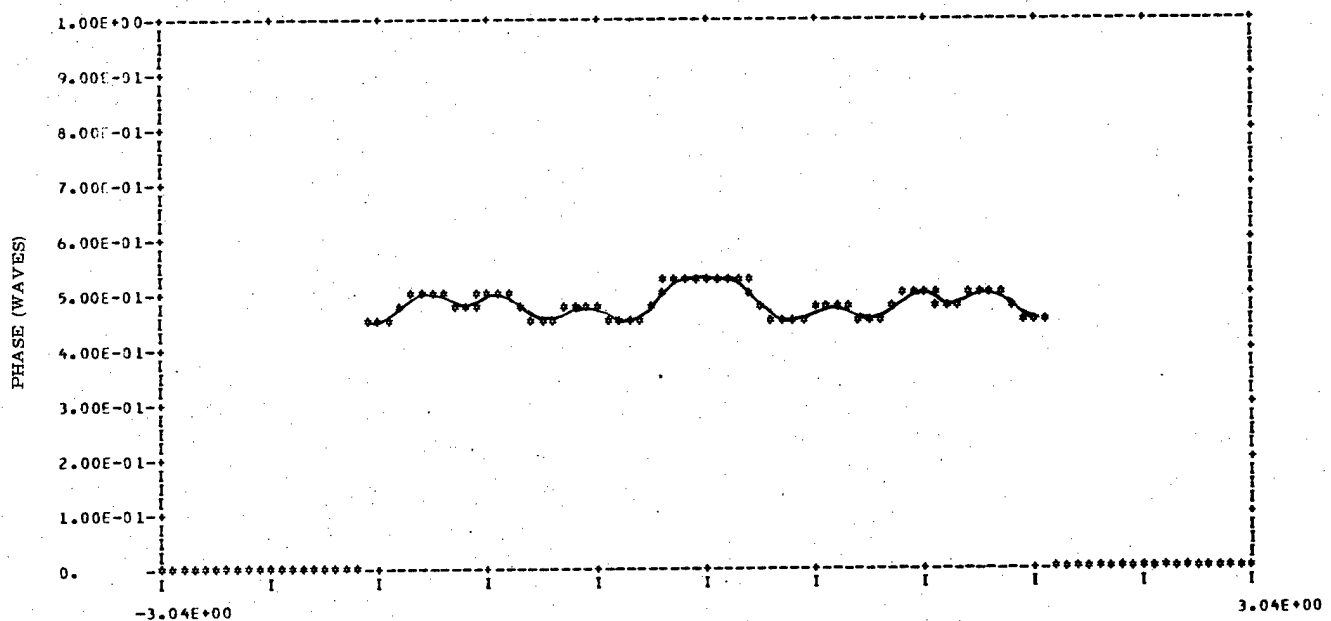


b) Phase

Figure 4-16. Phase and irradiance distribution at feedback mirror for  $M = 1.4$ , all-geometric axicon, along direction of  $.5 \times 10^{-4}$  cm offset.

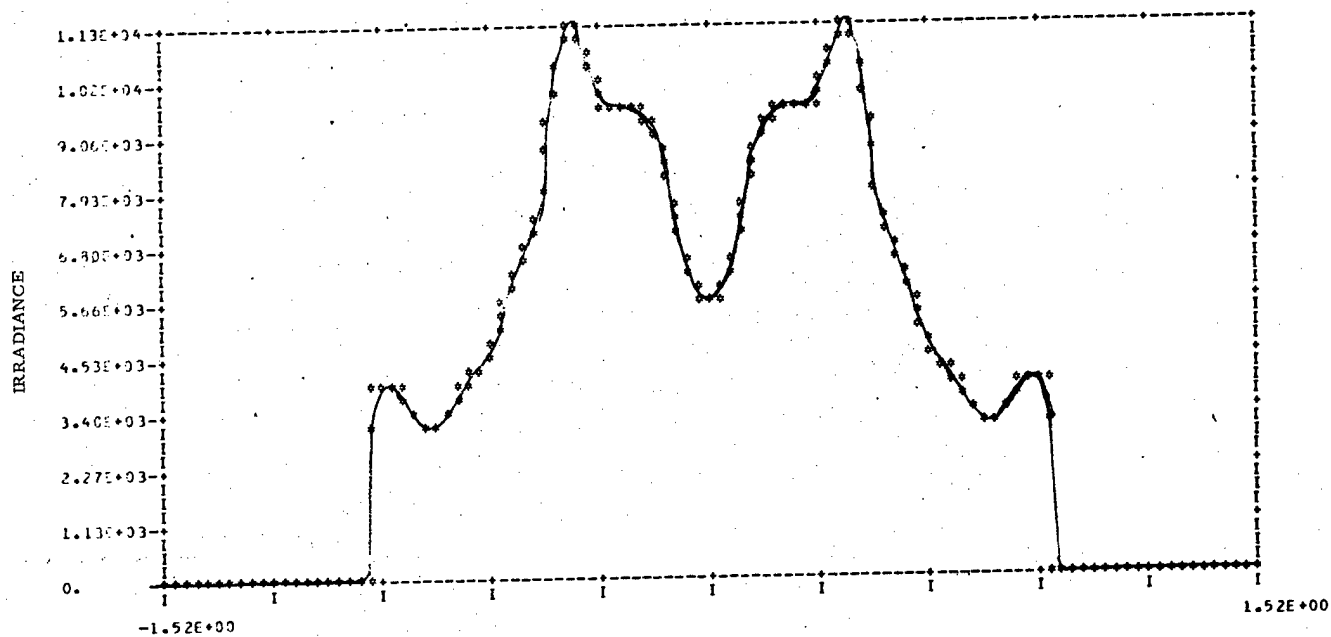


a) Irradiance

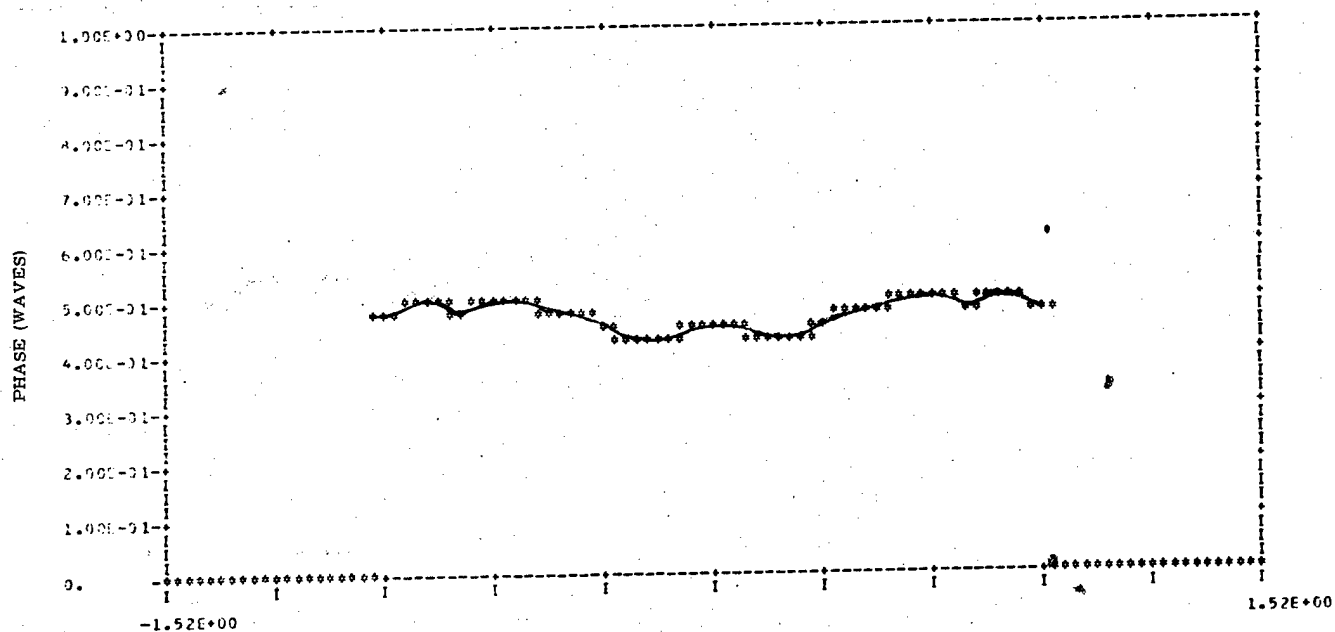


b) Phase

Figure 4-17. Phase and irradiance distribution at feedback mirror for  $M = 1.4$ , holographic axicon resonator with 130 cm compacted length.



a) Irradiance



b) Phase

Figure 4-18. Phase and irradiance distribution at feedback mirror for  $M = 2.0$ , all-geometric axicon resonator. A 256 x 256 point grid, instead of the 128 x 128 grid of figures 4-6 through 4-17.

Of course, this cannot answer suggestions that there are important effects observable only with a 100-fold grid point increase, nor is it likely that such an objection could be tackled with a three-dimensional code. This question must remain open for the present.

#### 4.7 CONCLUSIONS

Table 4-2 summarizes the results of computation performed in this task.

1. Resonators with axicon beam expansion and recompacting can achieve stable operation.
2. The portion of the resonator in which the beam is without a central hole need not be particularly long for this to occur.
3. If a holographic splitting axicon is used in the expansion, resonator magnification of less than 2.0 might be required for stability.
4. Tilt and decentration of the expander relative to the beam axis result in stable modes with attendant phase tilts.
5. The HGA resonator with  $M < 2$  is better able to endure tilt and decentration than an all-geometric configuration with magnification between 1.4 and 2.8.

TABLE 4-2.

M	Resonator Type	Starter Wave Type	Aligned, Empty Resonator	Aligned, Loaded Resonator	100 $\mu$ Rad Tilt	0.5 x 10 <sup>-4</sup> CM Decenter	1.0 x 10 <sup>-4</sup> CM Decenter	Power Outcoupling for Loaded Resonator (Geometric Outcoupling)
			CONVERGENT SOLUTION ATTAINED?					
1.4	All-Geometric	Plane	Yes	Yes	No	Yes	No	31% (50%)
		Tickled						
		Scrambled	Yes	Yes				
2.0	All-Geometric	Plane	Yes	Yes	Yes	Yes	No	58% (75%)
		Tickled						
		Scrambled		Yes				
2.8	All-Geometric	Plane	Yes	Yes	Yes	Yes	No	81% (88%)
		Tickled						
		Scrambled		Yes				
1.4	HGA	Plane	Yes	Yes	Yes	Yes	Yes	30% (50%)
		Tickled						
		Scrambled	Yes	Yes				
2.0	HGA	Plan	Yes	Yes	No			54% (75%)
		Tickled	Yes	No				
		Scrambled	Yes	No				
2.8	HGA	Plane	Yes	Yes	No			61% (88%)
		Tickled	No					
		Scrambled		No				

## SUMMARY OF CASES MODELED

The starter, or initial, waves have been described in the text. In the plane starter, the complex electric field value,  $x+iy$ , is constant over the beam. The scrambled initial wave has field values that are pairs of values obtained from a random number generator. The "tickled" starter is a mixture composed of 20 parts of the plane wave plus one part of the scrambled wave. The tickled start was attempted when convergence could not be reached from the scrambled starter. When convergence was attained for a loaded resonator from a scrambled start, the corresponding empty resonator case was usually not investigated. Since the purpose of the non-symmetric starters was to permit modes that are not actually symmetric to grow in an axially symmetric geometry, it was deemed unnecessary to use them in the tilted and decentered cases. A blank entry indicates that the case was not attempted.

## 5.0 DETAILED AXICON MODEL

### 5.1 TASK REQUIREMENTS

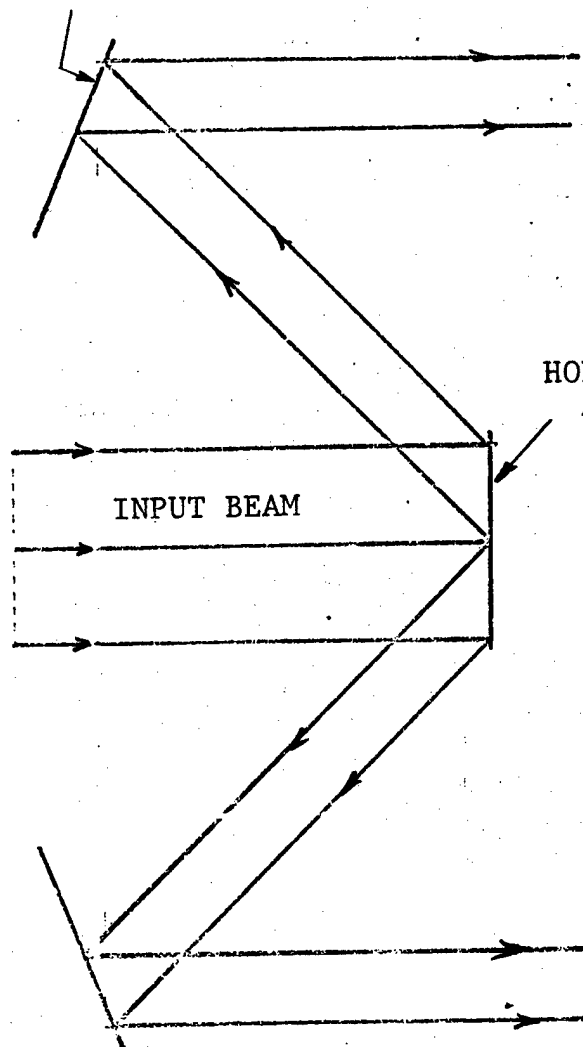
The analytic axicon models described earlier in the resonator modeling section are limited to axicons with their two cones perfectly aligned with respect to each other. Misalignment or figure error of either cone causes extreme complications in the analytic mapping function. Because of this difficulty, a ray trace model is needed for misaligned axicons or axicons with figure errors. HEXAGON, the Hughes optical design and evaluation program, has extensive ray trace capabilities, so a task to merge the resonator code with the ray trace code was developed.

Section 5-2 describes the tasks performed, while Section 5-3 explains the major modifications that had to be incorporated into HEXAGON. Section 5-4 gives the final results and an indication of necessary future work.

### 5.2 THE TASKS

The two axicon geometries modeled are shown in Figures 5-1 and 5-2. Figure 5-1 shows the operation of the holographic axicon expander, consisting of a single holographic grating and a conventional reflecting axicon. As shown, the output beam is an annulus consisting of the two diffraction orders from the grating. Figure 5-2 shows the conventional reflecting axicon contractor, consisting of two conventional reflecting axicons, that subsequently is used to contract the annulus to form the output beam. Figures 5-3 and 5-4 give examples of the output beam amplitudes from the two systems as found by the ray tracing methods to be described below. For Figure 5-3, a collimated, uniform amplitude was expanded. For Figure 5-4, the output from the holographic

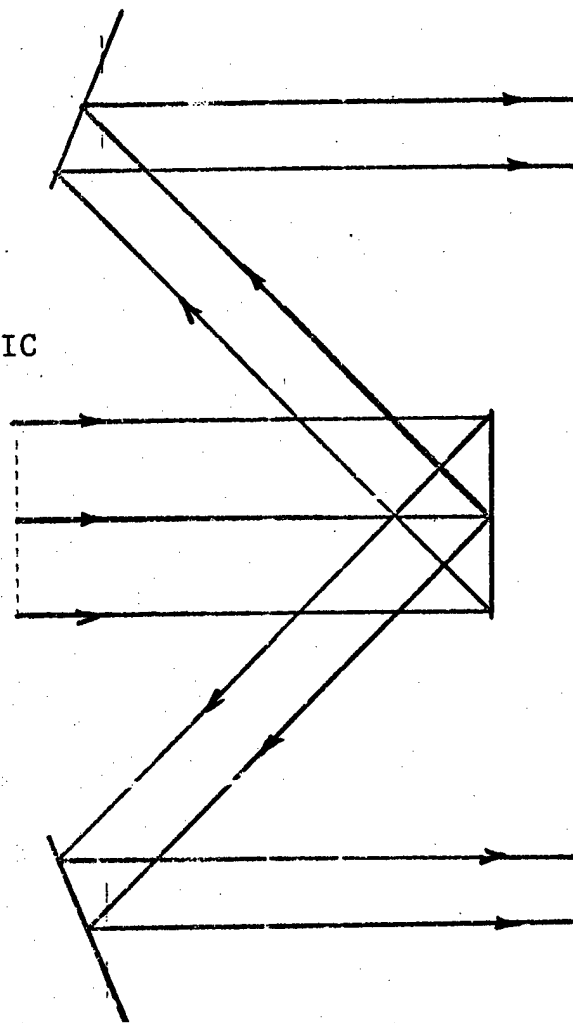
REFLECTOR



INPUT BEAM

HOLOGRAPHIC  
AXICON

a) Order = +1



b) Order = -1

Figure 5-1. Axicon beam expander profiles.

expander was used as the input to the contractor. As can be seen, the use of the holographic expanding element significantly alters the beam profile.

Due to the existence of extensive ray tracing codes in the Hughes optics program (HEXAGON), the modeling of the two subsystems was not difficult, even with the possibility of including in the models mechanical misalignments and construction errors in the axicons. The ray tracing approach was selected for the imperfect case because the analytical approach then becomes complex

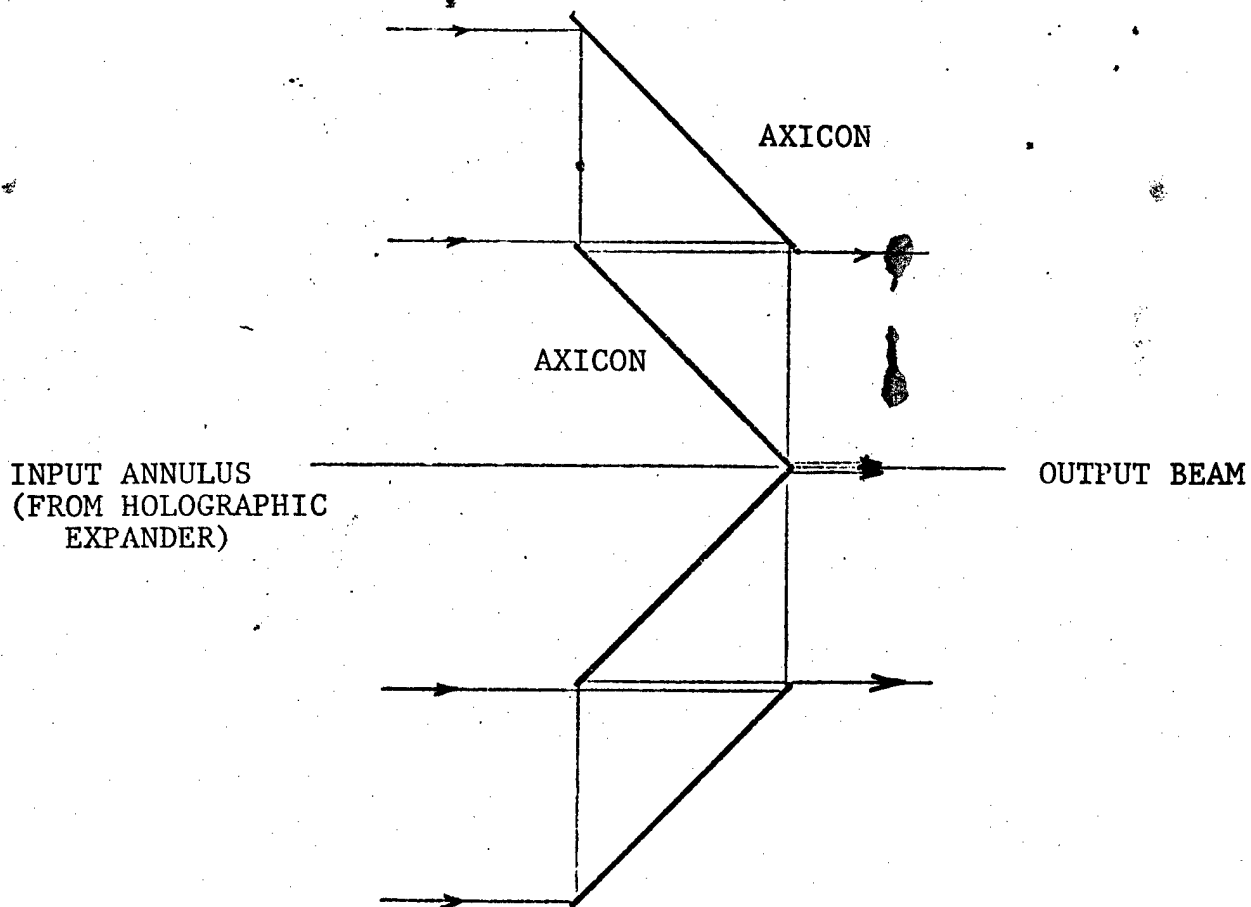
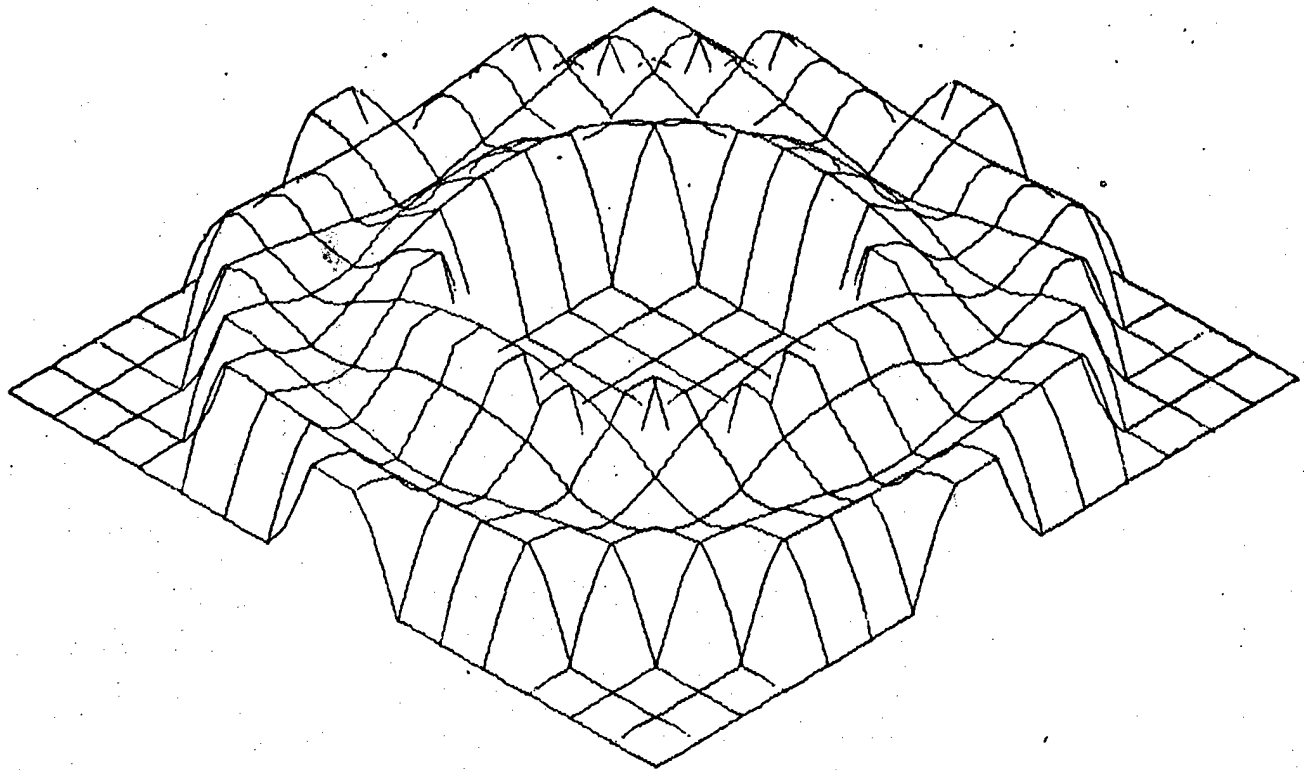


Figure 5-2. Axicon beam contractor profile.

and could involve some approximations. The ray tracing, on the other hand, is accurate, and can be used in a straightforward manner. In the beginning of the study, though, a large problem existed in the means of data transfer between the optics program and the resonator code.

Originally, the two programs were on different computers. The easiest way of transferring wavefront amplitude and phase information between the two programs was by punched cards, an inefficient method in view of the large number of passes around the resonator needed to establish convergence. In order to create a unified program, a resonator code was developed that worked on the Hughes IBM system. After this was supplied, we incorporated the routine in HEXAGON as a user-controlled subroutine, thereby allowing either interactive or batch operation of the complete resonator/optics program.





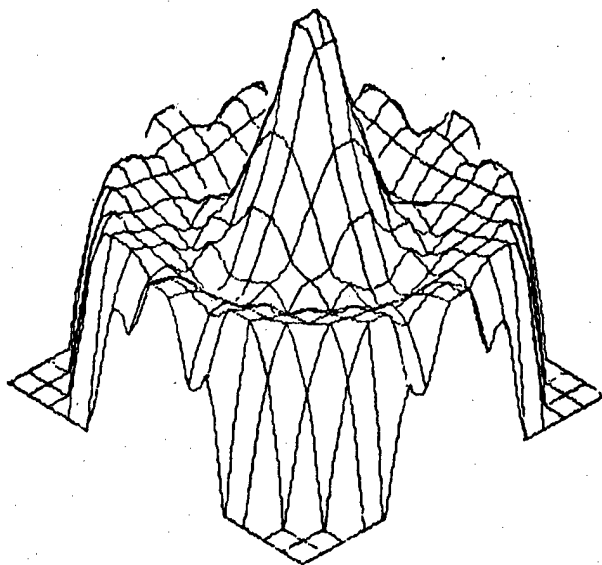
- UNIFORM AMPLITUDE BEAM INPUT

Figure 5-3. Holographic axicon expander output amplitude.

### 5.3 HEXAGON MODIFICATIONS

HEXAGON, as it existed at the onset of this study, lacked a few features that have since been added specifically for this study. First, since the input wavefront to either of the two optics models will always be in the form of amplitude and phase information defined over a square grid in space, it was necessary to create a transmission function that could be defined by the input information. Second, a geometric intensity mapping based on differential area transformations was developed to create, in conjunction with the transmission function, the amplitude descriptions at the outputs of the models. Finally, the early computer runs showed that use of the optics models, especially the expander, would be very expensive. As a result, two cost-saving schemes were incorporated in HEXAGON, both of which have been shown to produce substantial savings.

To understand these modifications, it is necessary to know how HEXAGON operates. In creating the wavefront description that is the output of either



- EXPANDER OUTPUT USED AS INPUT
- SAME SCALE AS FIGURE 5-3

Figure 5-4. Conventional axicon contractor output amplitude.

of the two optics models, rays are traced through the system to a square grid at the output. Since the input wavefront will not generally be flat, it is not known beforehand what path these rays will take, so an iterative ray-aiming process is used. To define the input wavefront and ray directions for the ray aiming process, the OPD map received from the resonator codes is first fitted to an aberration polynomial. This results in some smoothing of the data, but preserves the fundamental form of the input and therefore should not detract from the modeling results. The transmission function and intensity mapping modifications work with the results of the ray-aiming routine, whereas both cost-reduction schemes involve simplifying the ray-aiming process.

After the input amplitude information is used to set up a grid of transmission values at the inputs of the models, a ray is traced to a point on a square grid at the output. The location of this ray at the input surface is determined, and a four-point interpolation is used to determine the relative input intensity associated with the ray. The geometric transformation is then used to determine the output intensity. For this, a differential area at the output is related

to its mapping at the input, with the ratio determining the relative energy densities of the ray at the output and at the input. After all the rays have been traced, the total energy at the output is scaled to equal the input energy, and the amplitudes associated with each point on the output grid are calculated.

As stated above, both methods of reducing the operating cost work by simplifying the ray-aiming process. First, mathematically describing the holographic axicon as a phase grating rather than as a hologram significantly reduced the cost of tracing rays through the expander. This is because describing a surface as a hologram also requires defining the construction optics used to create the hologram. HEXAGON actually constructs the hologram each time a ray is traced, so raytracing through holograms is relatively expensive. Describing the same surface as a phase grating removes the construction optics from the ray-tracing procedure. This feature has been included in the unified program. The second method is one which has been put into the optics program, but which cannot yet be used in the unified program. In it, rays are aimed at a square grid at the input of the optical systems, rather than at the output, and a file is created that contains the output location, phase and amplitude of each ray traced. Before this information can be used by the resonator routine, though, an interpolation onto a square grid is needed for subsequent propagation through the gain medium, etc. To date, such an interpolation routine has not been developed.

Both of these methods can produce cost savings. The use of the phase grating has been included in the unified program, with a cost reduction of about a factor of three in establishing the wavefront description at the input of the laser cavity. The time required to do this, though, would still be roughly 75 percent of the time needed to propagate a wavefront entirely around the resonator, so that program is still not inexpensive to run. Even though the second method presently cannot be used with the resonator, we have shown a reduction by another factor of nine in the computing time needed to produce the output from the expander, relative to the system using the phase grating. An interpolation routine would somewhat reduce the savings, but, based on the time used by the expander in the present set-up, it is still likely that the resultant savings reduction would be significant.

#### 5.4 CONCLUSION

In its final form, the unified program did not work satisfactorily. We were able to propagate a wavefront once around the laser, but, on the second circuit, the ray-aiming process of the optics routine failed at the contractor model. The explanation is that if, after 10 iterations, a ray has not been traced sufficiently near the desired output point, the program assumes that no ray will reach that point. Ordinarily this causes no difficulty, but if the point is the one that defines the reference ray for calculating the phase information at the output, an output file cannot be generated. This was the situation at the contractor.

A few schemes have been considered that should solve the ray-aiming problems, but none are currently available in the unified program. First, once an interpolation routine is developed, the second cost-saving scheme described above can be used. If a ray fails to be traced through the system, it will be because it physically misses a surface, not because the ray-aiming procedure failed to converge. Second, the method of determining the first-guess for the iterative ray-tracing routine can be modified to fit the axicon models more accurately. This would probably be fairly involved, though, and still may not ensure that the iterative process will always work. Finally, the phase information at the input to either of the models can be ignored, except as additive phase contributions at the output, rather than being used to produce ray deviations corresponding to a deformed wavefront at the input. Since the rays being traced would then be independent of any input phase information, if the system could be made to work once, it would always work.

## 6.0 AXICON FABRICATION AND MEASUREMENT

### 6.1 TASKS

The grating fabrication tasks were (a) to fabricate and test a grating axicon for a visible wavelength ( $6328\text{\AA}$ ) and (b) to investigate techniques for producing grating axicons for infrared wavelengths.

A grating axicon consists of concentric circular grooves of constant period, as shown in Figure 6-1. An inner axicon diffracts an incident collimated beam into  $\pm 1$  orders, forming a conical annular beam. An outer axicon diffracts into only one order and is used to convert a conical beam into a collimated annular beam. For high efficiency inner axicons, where  $\pm 1$  diffraction orders are used, symmetric groove shapes are suitable. Asymmetric

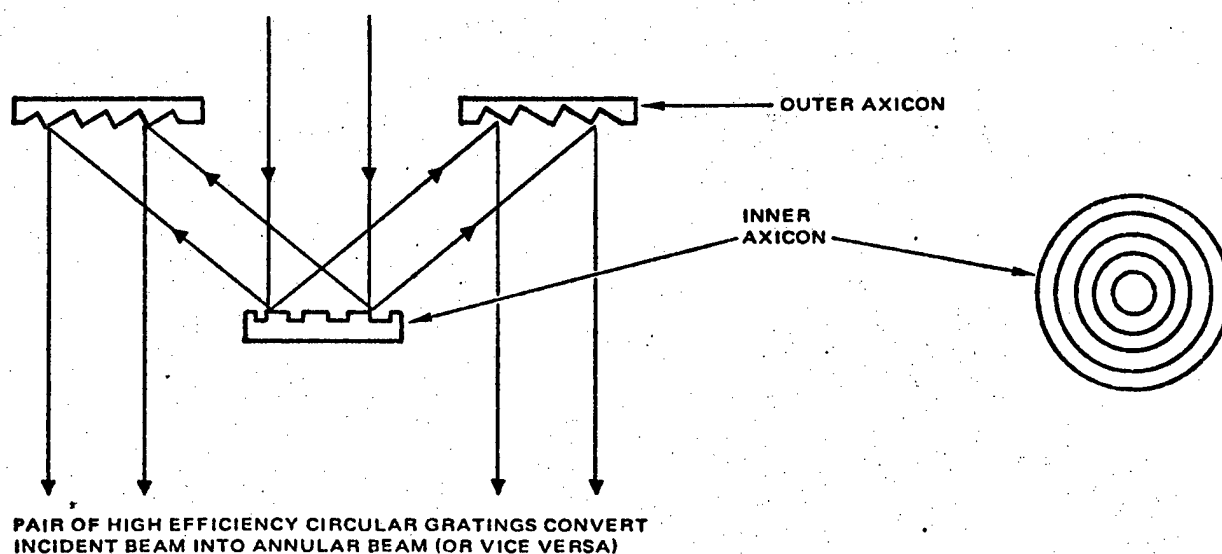


Figure 6-1. Holographic grating axicon.

(blazed) groove shapes are required for high diffraction efficiency into one order for outer axicons. The groove shape and depth for maximum efficiency in both cases can be determined by theoretical grating design. Aberrations in the diffracted wavefronts are determined by the accuracy of the groove locations and substrate quality. In holographic fabrication techniques, high quality construction optics are necessary to minimize variations in the grating period. For computer generated axicons, the plotting and photo-reduction equipment and development processes determine the accuracy of the grating period.

In a previous phase of our current contract effort and on other diffraction grating work, we have demonstrated theoretically and experimentally that high diffraction efficiency at infrared wavelengths can be attained with ion etched (or ion machined) gratings that normally have symmetrical grooves. However, asymmetrical ion etched grooves have also been demonstrated at Hughes by using an ion beam incident at an angle to the substrate. In addition, asymmetrical grooves can be made by diamond ruling techniques. Gratings with asymmetrical grooves have been shown theoretically and experimentally to produce very high diffraction efficiencies at infrared wavelengths.

The major problem in making grating axicons is not of producing the high efficiency groove shapes, but of producing circular fringe patterns of adequate optical quality. As optical interferometry is most simply accomplished at visible wavelengths, our original plans were to fabricate axicons suitable for measurement at  $6328\text{\AA}$ . These were to be fabricated holographically by interfering waves refracted from a glass cone. We were able to demonstrate feasibility, and to identify and solve a number of problems associated with this technique. However, a simpler approach than holography was found in contact printing a photoreduced pattern generated by computer. This limited us to groove spacings suitable for infrared wavelengths, and these gratings were designed to operate at  $10.6\text{ }\mu\text{m}$ .

Grating axicons are fabricated by first exposing the pattern onto a photoresist layer deposited over the substrate of interest. The exposure is accomplished either by the interference of construction wavefronts or by contact printing through a master pattern. The developed photoresist grating axicon is then used as a mask to transfer the pattern into the metal layer of

the substrate via ion matching. The excess photoresist is subsequently removed leaving a grating axicon in the metal layer suitable for high power applications.

The visible axicon task was initiated in part to allow for wavefront interrogation using simple interferometry with visible light. The grating axicon is fabricated holographically using a refracting glass cone to produce the construction wavefronts. One problem encountered during the experimental work was obtaining a glass cone of sufficient optical quality to be used in the exposure system. Further difficulty was caused by intensity variations at the exposure plane due to the nature of the interfering geometry. A small glass cone was borrowed from another project and used during the program; this cone was suitable for fabricating a  $41^\circ$  diffracting grating axicon for  $6328\text{\AA}$  wavelength with a  $0.96\text{ }\mu\text{m}$  grating period. Experimental exposures with and without intensity-shaping filters failed to produce an axicon of sufficient size for phase measurement.

Although not part of the contract task, experimental work was started during the course of the program to fabricate an IR grating axicon for the  $10.6\text{ }\mu\text{m}$  wavelength using a computer generated mask. A 20X enlarged grating axicon pattern (42-inch diameter) was drawn by the Hughes Precision Plotting Facility on photographic sheet film. Subsequent photo-reduction by a vendor (Optronics Speciality Co.) produced a chrome master pattern (2.1-inch diameter) suitable for contact printing a  $45^\circ$  diffracting axicon for the  $10.6\text{ }\mu\text{m}$  wavelength with a  $15\text{ }\mu\text{m}/\text{cycle}$  grating period. The axicon diffraction characteristics and performance will be measured using this 2 inch diameter IR grating axicon ion machined into gold on a glass substrate. An inner-outer axicon pair will be fabricated to produce a collimated annulus whereby phase measurements can be done using a point diffraction interferometer at the operating wavelength of the grating axicon. These data on the IR axicon should be more pertinent to the ultimate use of grating axicons in laser resonator geometry than similar data on a visible axicon.

## 6.2 VISIBLE GRATING AXICON FABRICATION - HOLOGRAPHIC TECHNIQUE

The interference wavefronts for recording constant spacing concentric circular grooves utilize a refracting cone in an exposure geometry as shown

in Figure 6-2. The 4416 Å wavelength output of HeCd laser is collimated and incident onto the base of the glass axicon. The exposure plane is located at the intersection of the refracted conical wavefront. The grating spacing at the exposure plane is a function of the base angle of the glass cone, and the size of the exposure plane is proportional to the size of the construction optics.

This method has two advantages: It does not require the use of the axicon tip (which is often difficult to fabricate to optical tolerances) in the exposure. It is also self-referencing; that is, it does not require a previously split off reference wave, and consequently no fringe stabilization is necessary. There are, however, several disadvantages: A major drawback is that the holographically produced patterns are limited in optical quality by the quality of the glass cones. It was not until the end of the program that one vendor was able to supply a 10 cm diameter cone with wavefront aberrations of

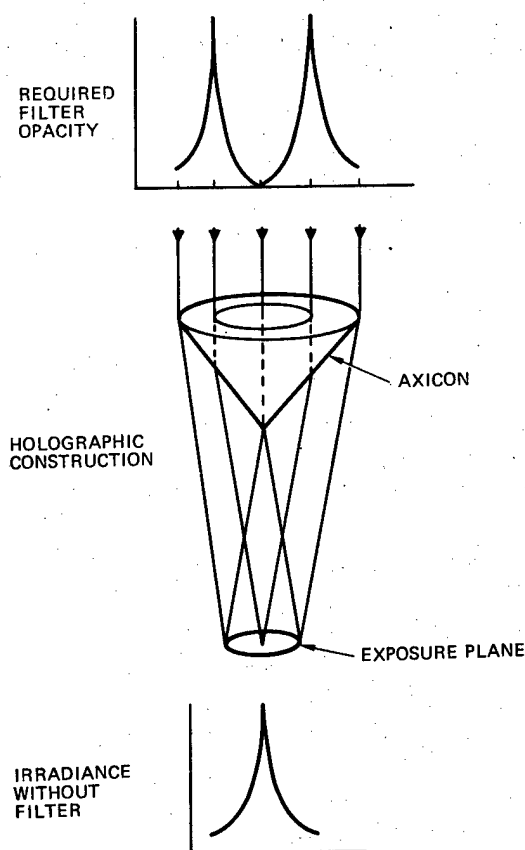


Figure 6-2. Self-referencing exposure geometry for a holographic grating axicon. The filter is required to compensate for the nonuniform intensity in the exposure plane.



only  $1/4$  to  $1/2$  visible wavelengths. Unlike conventional optics, no reduction in aberration will result at longer wavelengths for grating axicons produced from these components (aberrations will always be the same fraction of the laser wavelength irrespective of that wavelength). Even on high quality glass cones, circular polishing striations were apparent on the transmitted beam as shown in Figure 6-3. Although these circular striations do not restrict the holographic exposure, an image of these marks is superimposed onto the the exposed grating grooves during exposure. With transmissive optics, extraneous reflections from the many optical surfaces cause moire fringes which can further degrade the grating. However, reflection problems can be minimized by proper antireflection coating of all construction optical elements.

Further difficulty is introduced by intensity variations at the exposure plane. Each groove at the exposure plane is formed by the interference of different diameter annular ring sections of the incident wavefront at the base of the glass axicon. This causes a variation in exposure intensity as well as beam ratio which determines the fringe contrast. The non-uniformity is inherent in conical optics, but it can be compensated by making accurate filters.

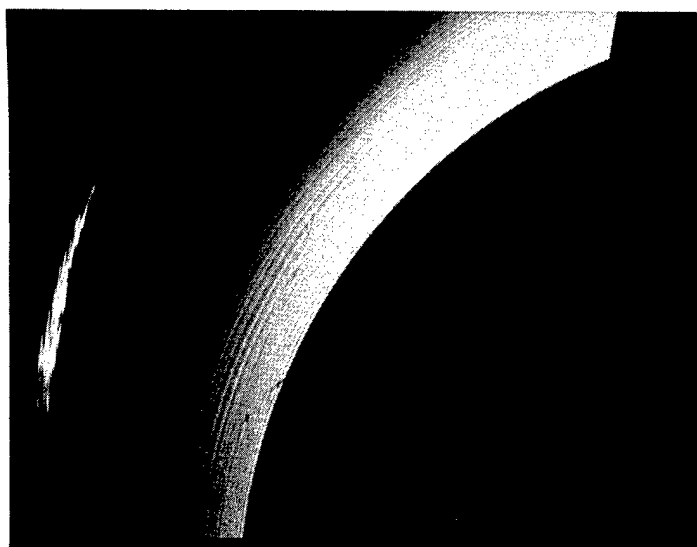


Figure 6-3. Transmitted annular beam shows circular polishing striations of refracting cone.

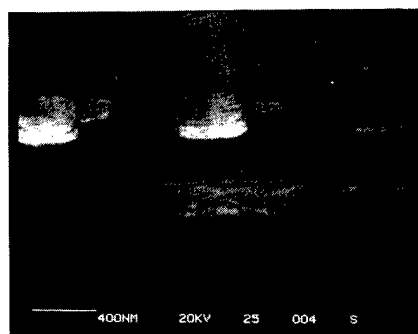
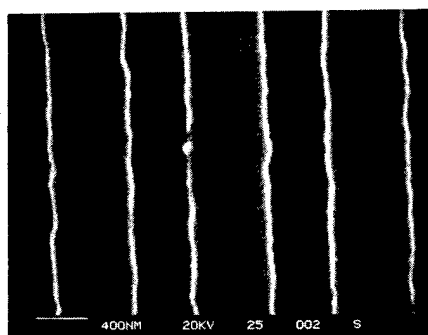
### 6.3 LINEAR GRATING FABRICATION

To investigate fabrication of grating axicons, experimental work was initiated with  $1\text{ }\mu\text{m}/\text{cycle}$  linear gratings formed by the interference of two intersecting wavefronts. The grating period was chosen to be representative of the spatial frequencies of circular grating axicons for use at the visible wavelength. Photoresist characteristics and the effects of the photoresist layer thickness were examined. Also the exposure tolerance required for generating a grating axicon can be identified.

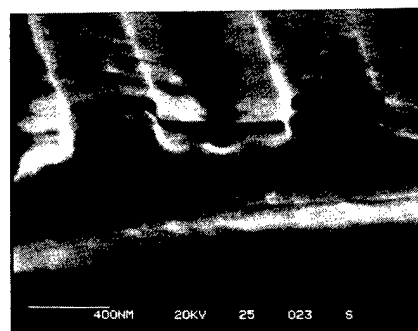
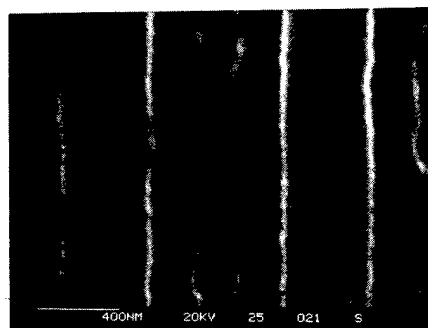
A gold layer was sputter deposited on a silicon wafer substrate. Shipley photoresist (1350B) layers of  $1000\text{ }\text{\AA}$  and  $4200\text{ }\text{\AA}$  were deposited by spin coating. A vacuum prebake of two hours at  $60^{\circ}\text{C}$  was used to remove non-photosensitive solvents in the photoresist coating. A grating was then recorded in the photoresist layer using the  $4416\text{ }\text{\AA}$  wavelength of the HeCd laser. The resist was developed in Az developer, rinsed in deionized water for 5 minutes, and dried using a nitrogen air gun. The grating samples were then cleaved, and the profiles were examined with a SEM.

SEM photographs of  $1\text{ }\mu\text{m}/\text{cycle}$  linear gratings recorded in  $4200\text{ }\text{\AA}$  of photoresist are shown in Figure 6-4. Note the standing waves along the side walls of the grating profile. This is due to the interference of reflected waves from the gold substrate with the incident construction wavefronts. Separation between nodes is  $\lambda/2n = 1314\text{ }\text{\AA}$ , where  $n$  (photoresist index of refraction) is 1.68. The development rate of the photoresist is dependent on exposure energy. Due to the standing waves, the development rate varies as layers of the standing wave are penetrated until the substrate is reached. A proprietary technique to minimize these standing wave effects is discussed in the Holographic Grating Study Report, v. 1., August '78. Underexposure causes excess photoresist to remain in the grooves of the grating, thereby impeding the ion machining of the metal layer. Overexposure causes reduction in duty cycle and deformation of groove shape. Roughness along the edge of grating grooves is attributed to the substrate surface quality, since each standing wave layer is a holographic image of the substrate surface.

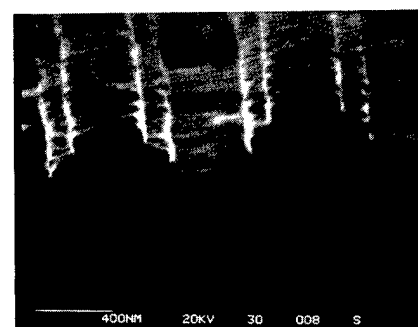
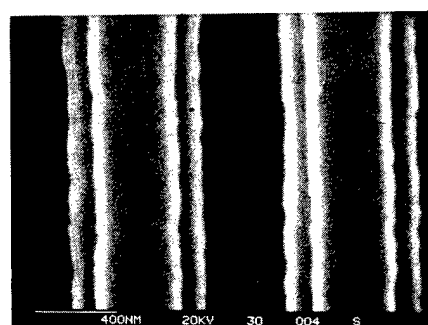
SEM photographs of  $1\text{ }\mu\text{m}/\text{cycle}$  gratings recorded in  $1000\text{ }\text{\AA}$  layers of photoresist are shown in Figure 6-5. Note the improvement in grating profile due to the absence of standing waves. This is attributed to the resist layer thickness being less than the period of the standing waves.



a.  $25 \text{ mJ/cm}^2$

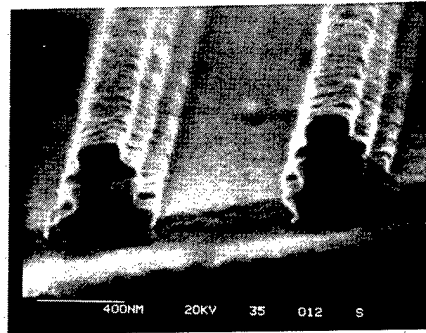
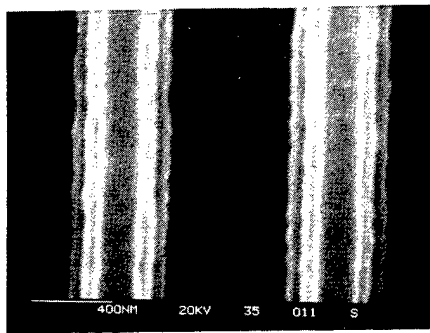


b.  $28 \text{ mJ/cm}^2$

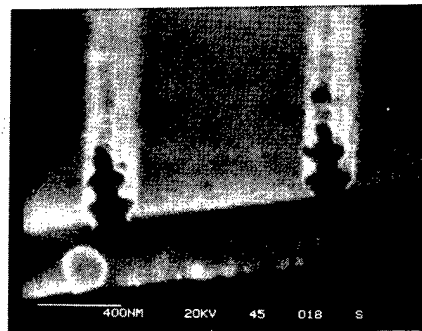
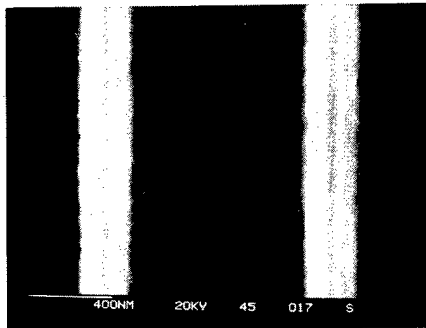


c.  $34 \text{ mJ/cm}^2$

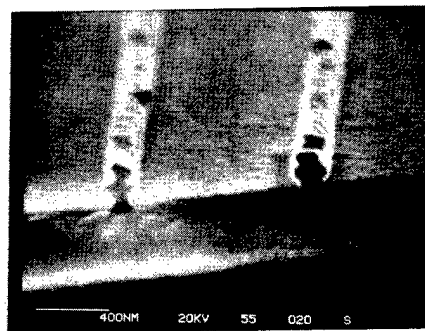
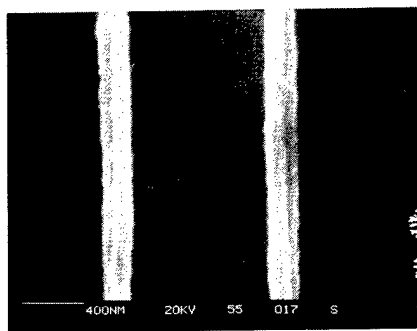
Figure 6-4.  $1\mu\text{m/cycle}$  grating recorded in  $4200^\circ\text{A}$  of photoresist with standing wave nodal separation of  $1314^\circ\text{A}$ .  
(Sheet 1 of 2)



d.  $40 \text{ mJ/cm}^2$

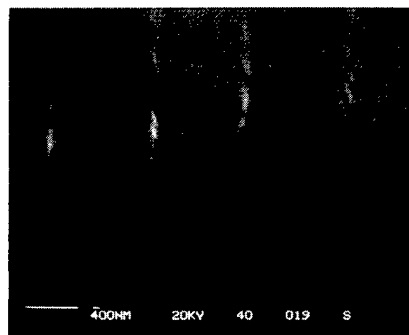
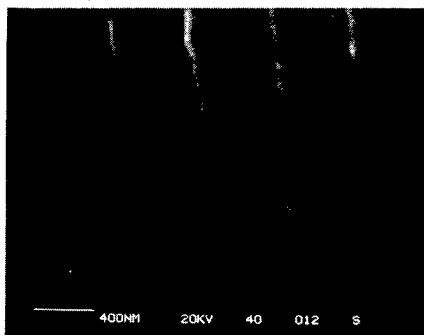


e.  $52 \text{ mJ/cm}^2$

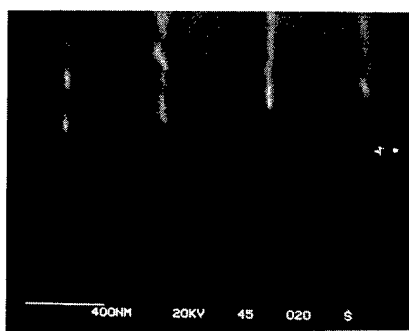
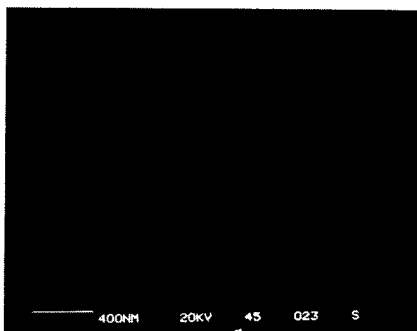


f.  $63 \text{ mJ/cm}^2$

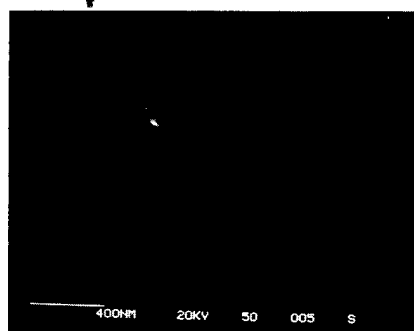
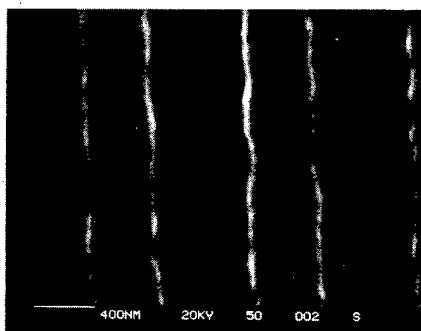
Figure 6-4.  $1 \mu\text{m/cycle}$  grating recorded in  $4200^\circ\text{A}$  of photoresist with standing wave nodal separations of  $1314^\circ\text{A}$ .  
(Sheet 2 of 2)



a.  $40 \text{ mJ/cm}^2$

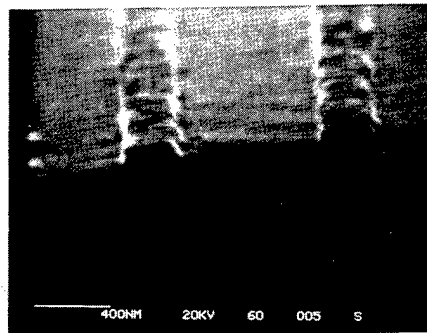
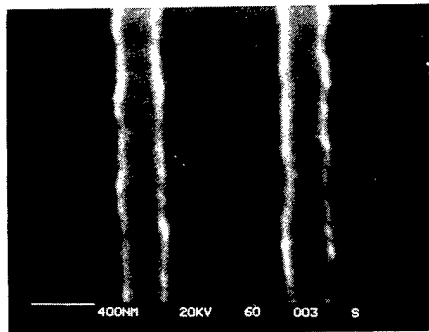


b.  $45 \text{ mJ/cm}^2$

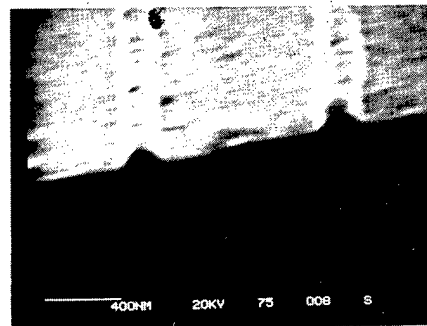
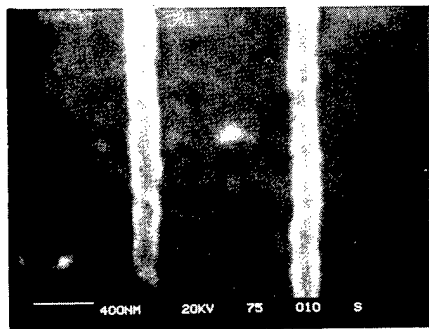


c.  $50 \text{ mJ/cm}^2$

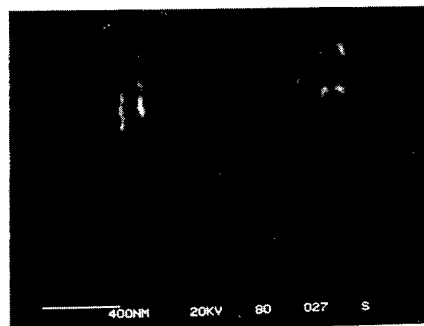
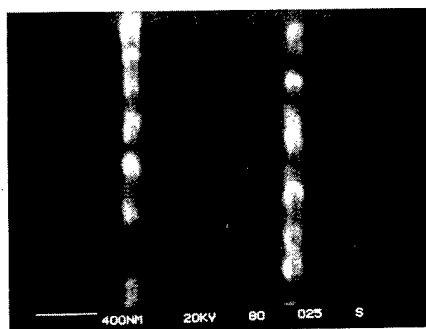
Figure 6-5.  $1\mu\text{m/cycle}$  grating recorded in  $1000^\circ\text{A}$  of photoresist. (Sheet 1 of 2)



d.  $60 \text{ mJ/cm}^2$



e.  $75 \text{ mJ/cm}^2$



f.  $80 \text{ mJ/cm}^2$

Figure 6-5.  $1\mu\text{m/cycle}$  grating recorded in  $1000^\circ\text{A}$  of photoresist. (Sheet 2 of 2)

Figures 6-6 and 6-7 are summary graphs of the duty cycle versus exposure energy for the photoresist gratings shown in the previous two figures. For thicker photoresist layers where standing waves are dominant, there is a steep change in duty cycle versus exposure. Therefore small variations in exposure energy can cause large duty cycle changes. The exposure range between underexposure (duty cycle = 1) and overexposure (deformed resist grating) is  $37 \text{ mJ/cm}^2$  to  $57 \text{ mJ/cm}^2$ . For thinner photoresist layers where standing wave effects are minimized, a much larger range of exposures can be tolerated without either over or under exposing the photoresist grating and therefore better control of the duty cycle can be achieved.

High efficiency symmetric grating grooves for the 6328 Å wavelength require an ion machining depth of approximately 1600 Å. Although the ion machining rate is 4x faster in gold than in photoresist, the trapezoidal photoresist grating shape erodes to a triangular shape. Further ion machining at this point produces a multi-faceted sidewall of the grating groove. From experimental work on previous programs we concluded that the photoresist grating height should be comparable to the required ion machining depth. In general it is desirable to achieve photoresist gratings with high aspect ratios (grating height to period) to insure accurate transfer of the grating into the metal layer via ion machining.

#### 6.4 CIRCULAR GRATING FABRICATION

Within the self-referencing exposure scheme, the master cone may be oriented either for refraction or reflection. Analysis shows that each geometry yields different manufacturing tolerances on deviations from the specified cone angle.

Design calculations were made as follows: The desired annular reconstruction at wavelength  $\lambda_r$  and angle  $\theta_r$  determines the fringe spacing, D:

$$D = \frac{\lambda_r}{\sin \theta_r}.$$

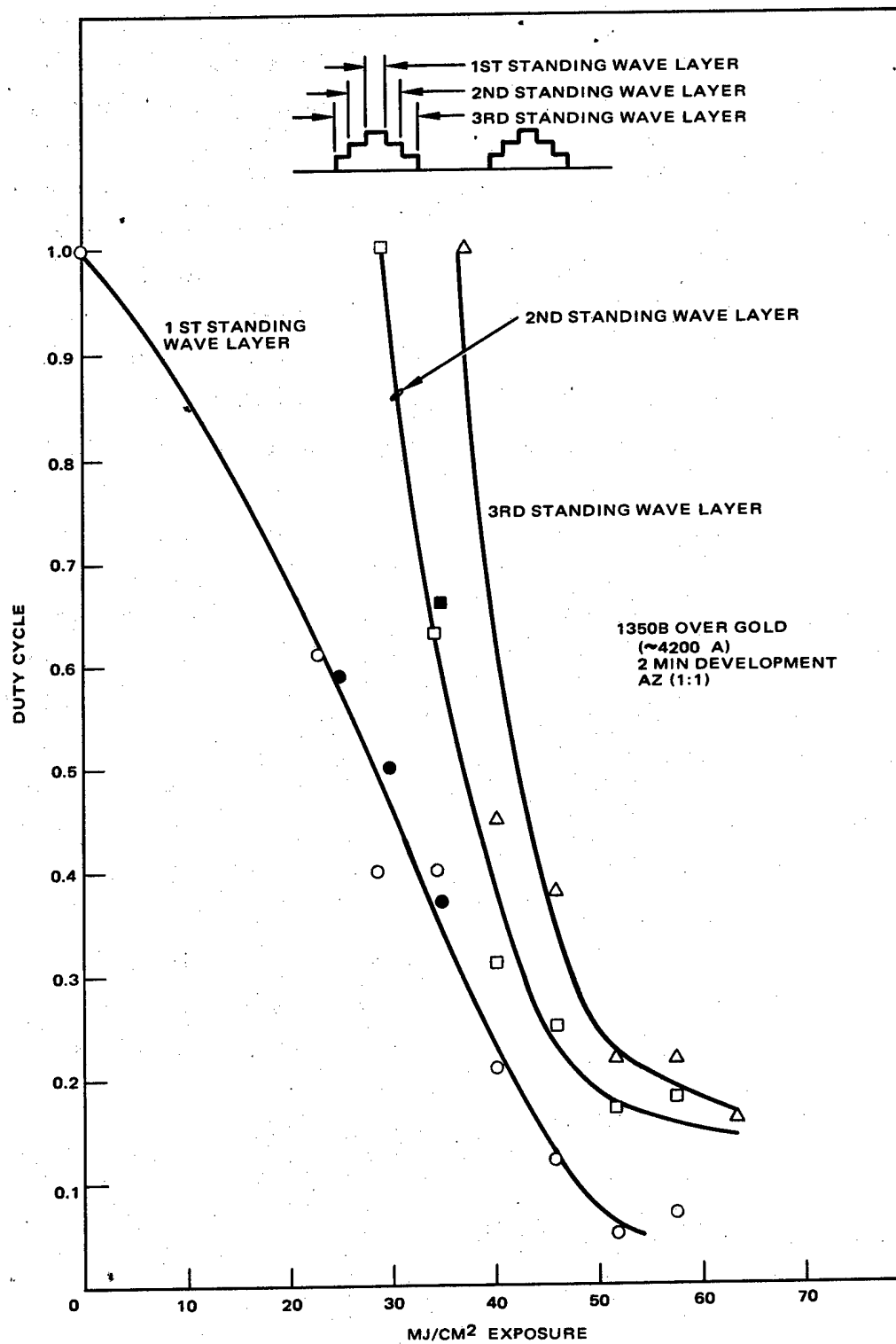


Figure 6-6. Experimental data of duty cycle versus exposure for  $1\mu\text{m}/\text{cycle}$  grating on  $4200\text{\AA}$  of photoresist.



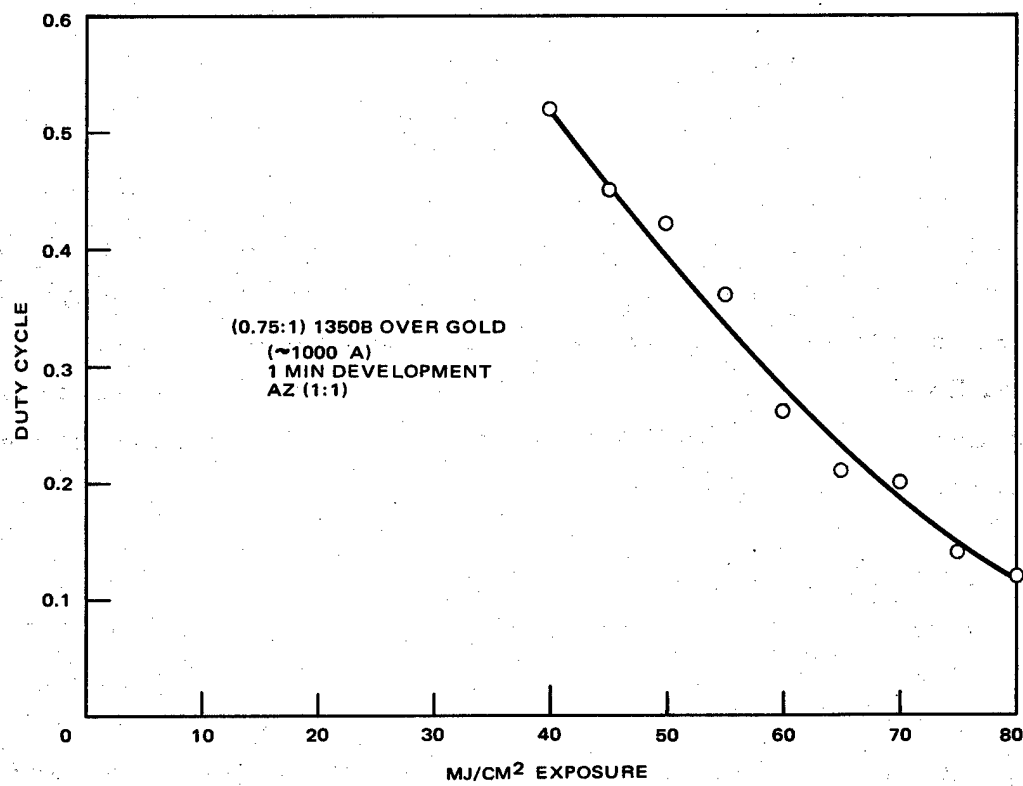


Figure 6-7. Experimental data of duty cycle versus exposure for 1 $\mu$ m/cycle grating on 1000 $\text{\AA}$  of photoresist.

This spacing is produced by a construction annulus at wavelength  $\lambda_c$  converging at an angle  $\theta_c$  given by

$$2 \sin \theta_c = \frac{\lambda_c}{D}.$$

Combining the two gives

$$\theta_c = \sin^{-1} \left( \frac{\lambda_c}{2\lambda_r} \sin \theta_r \right).$$

The three construction axicons shown in Figure 6-8 have been analyzed to determine the base angle,  $\theta_a$ , of each. The sample angles next to each figure were calculated by assuming a construction wavelength of 4416 Å, axicon material BK-7 ( $n = 1.526$  at 4416 Å) and reconstruction at 6328 Å to yield a  $45^\circ$  annulus. Numbers listed under  $\frac{d\theta_c}{d\theta_a}$  give a relative measure of the sensitivity of each axicon to manufacturing errors.

#### Quality of the Conical Axicon

Because of the delays and difficulties encountered by our initially chosen optical vendor, we received only one good-quality cone during the course of the program. This axicon had a 10 cm base and a  $\theta_a$  of approximately  $26^\circ$ . As originally delivered, the axicon was of exceptionally poor optical quality. In Figure 6-10 is an image of a beam that was passed twice through the axicon. Note that this is not an interferogram. The lines radiating from the center are actually due to microfocusing from a scalloped edge.

To test the optical quality, we set up the interferometer shown in Figure 6-9. In Figure 6-11 we show the interferogram of the  $26^\circ$  axicon as originally delivered. We had this same axicon resurfaced by a local optical vendor

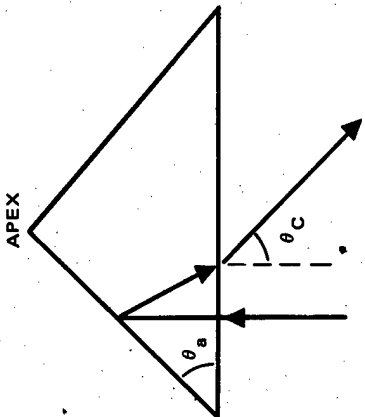
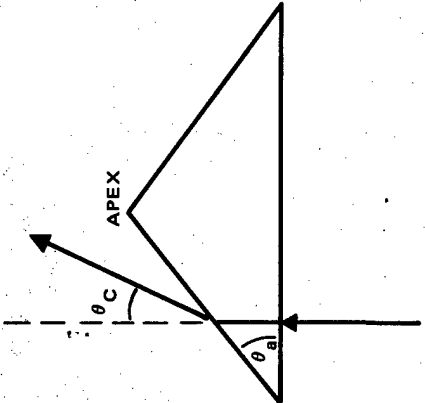
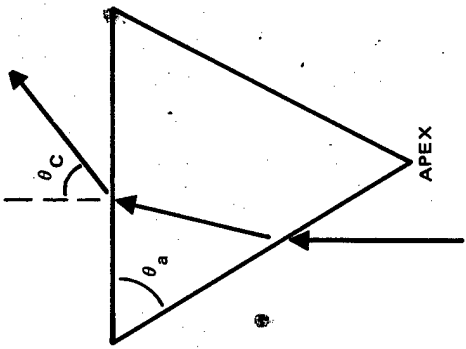
TYPE	REFLECTIVE AXICON INSIDE A REFRACTIVE CONE	REFRACTIVE AXICON: BEAM INCIDENT ON BASE	REFRACTIVE AXICON: BEAM INCIDENT ON CONE
GEOMETRY			
$\theta_a$ WHERE $\theta'_C \equiv \sin^{-1} \left( \frac{\sin \theta_C}{n} \right)$	$\frac{1}{2} \theta'_C$	$\tan^{-1} \left( \frac{\sin \theta_C}{n \cdot \cos \theta_C} \right)$	$\tan^{-1} \left( \frac{\sin \theta'_C}{\cos \theta'_C \cdot 1/n} \right)$
EXAMPLE (SEE TEXT)	$\theta_a = 4.65^\circ$ $\frac{d\theta_C}{d\theta_a} = 3.3$	$\theta_a = 23.89^\circ$ $\frac{d\theta_C}{d\theta_a} = 2.2$	$\theta_a = 26.0^\circ$ $\frac{d\theta_C}{d\theta_a} = 0.83$

Figure 6-8. Results of construction axicon design analysis.

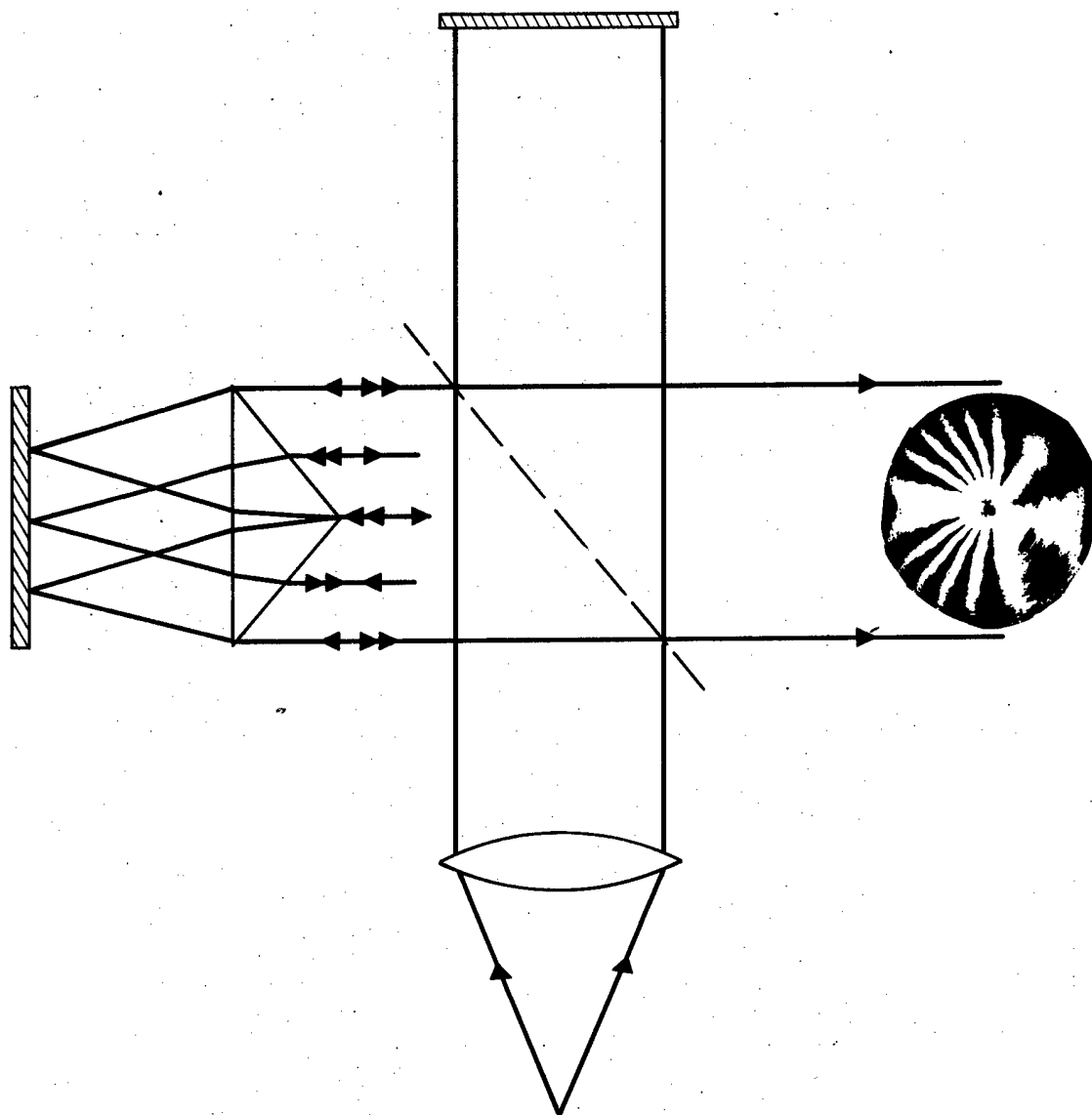


Figure 6-9. Interferometric testing of refractive conical axicon.

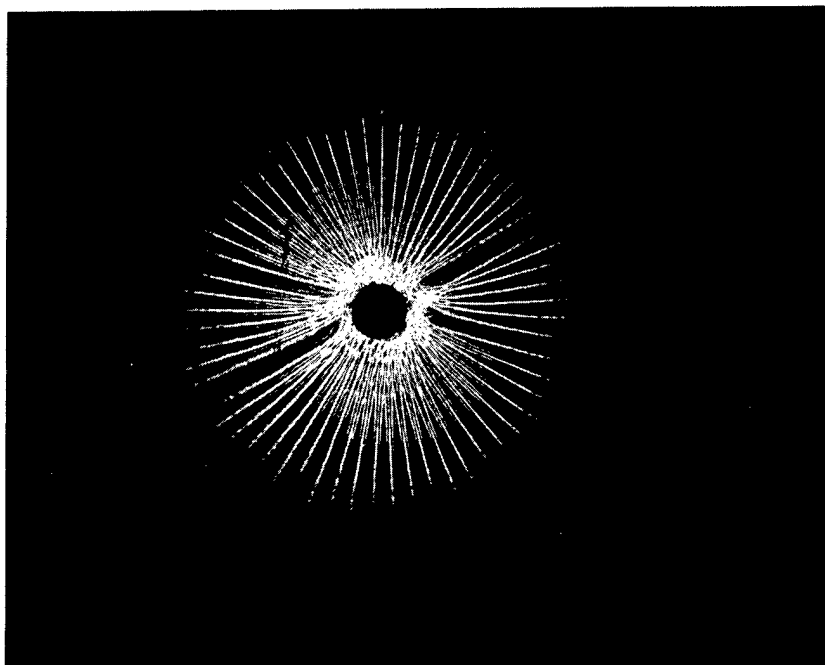


Figure 6-10. Twenty-six degree BK-7 axicon, as received. Pattern shows microfocusing of double-passed beam (not an interferogram).

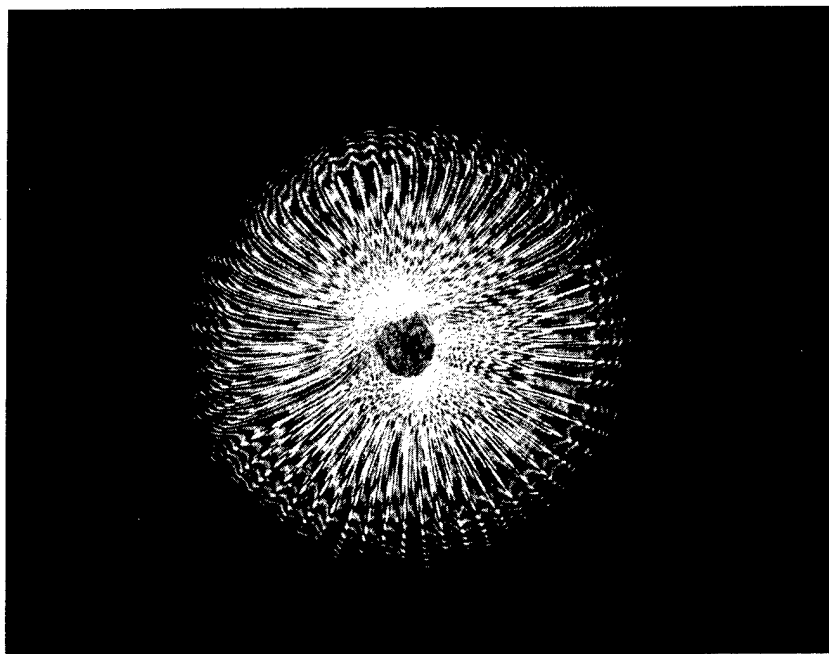


Figure 6-11. Twenty-six degree BK-7 axicon, as received. Interferogram of double-passed beam.

and we tested the axicon during an intermediate stage in the polishing process to aid the polisher. The intermediate and final interferometric results are shown in Figures 6-12, 6-13 and 6-14. Away from the center, the magnitude of the phase aberrations can be determined by

$$\frac{(1 \text{ to } 2 \text{ fringes deviation})}{(2 \text{ passes})} \left( \frac{\lambda}{2} \text{ per fringe} \right) = \frac{\lambda}{2} \text{ to } \frac{\lambda}{4}.$$

### Controlling the Intensity Distribution in the Exposure Plane

The first grating axicon samples were generated for use at 6328 Å with a small (2-inch) conical axicon borrowed from another project. We were able to demonstrate the simplicity of the basic self-referencing exposure scheme. However, the trial samples confirmed the need to compensate for the intensity nonuniformities in the holographic exposure. By minimizing standing wave effects, the tolerance in fabricating a proper density profile has been increased. However, any non-uniformity in exposure energy will cause duty cycle variation and consequently non-uniformity in the efficiency.

The nonuniformities arise because each "ring" of beam area incident on the axicon will be expanded or contracted before reaching the exposure plane, causing the rings that interfere to have unequal intensities. Figure 6-15 describes the interference of two waves, and Figure 6-16 shows the variation in beam ratio and intensity at the grating axicon exposure plane. The beam ratio varies from 1:1 with maximum contrast at the center to zero fringe contrast at the edge of the exposure plane. The exposure intensity approaches infinity at the center of the exposure plane where interfering wavefront sections are compressed to a focal point. A filter that can compensate for this inherent nonuniformity has been designed to be placed before the axicon.

The desired filter profile was shown in Figure 6-2. It features a nearly opaque ring with the density tapering off radially about it. If a uniform beam were allowed to enter the axicon, a line focus would be formed on-axis, which would yield a non-uniform holographic exposure. By shading the ring of incident light that focuses in the grating exposure plane, it is possible to smooth out the exposure plane intensity.



Figure 6-12. Twenty-six degree BK-7 axicon, after first resurfacing.  
Interferogram of double-passing beam.



Figure 6-13. Twenty-six degree BK-7 axicon, after second resurfacing.  
Interferogram of double-passed beam.

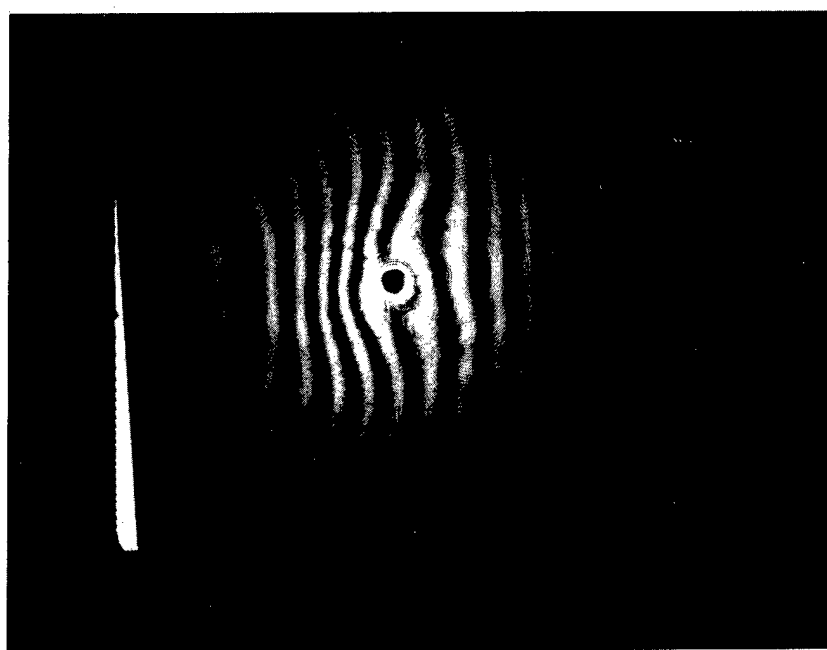
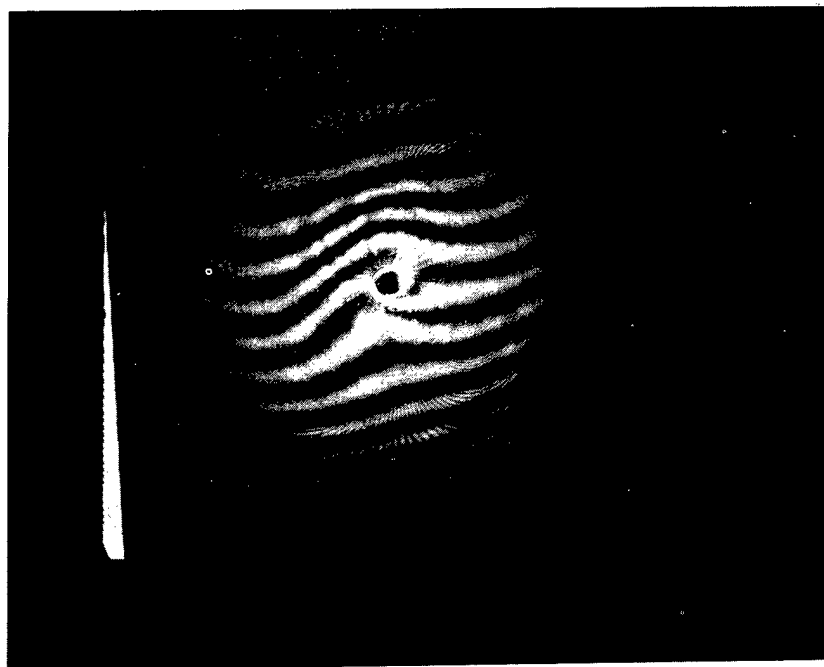
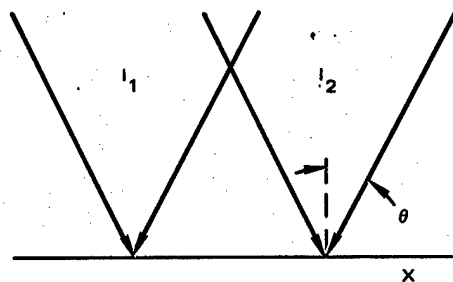


Figure 6-14. Twenty-six degree BK-7 axicon, after second resurfacing.  
Interferogram of double-passed beam.





$$I(X) = I_1 + I_2 + 2\sqrt{I_1 I_2} \cos \frac{2\pi X}{D}$$

$$I(X) = I_1 (1 + R + 2\sqrt{R} \cos \frac{2\pi X}{D})$$

$$I(X) = I_{AVG} (1 + K \cos \frac{2\pi X}{D})$$

$$I_{AVG} = I_1 + I_2$$

$$R = \frac{I_2}{I_1} \quad K = \frac{2\sqrt{R}}{1+R}$$

#### HOLOGRAPHIC AXICON EXPOSURES

- VARIATION IN K (FRINGE CONTRAST)
- VARIATION IN  $I_{AVG}$  (AVERAGE INTENSITY)

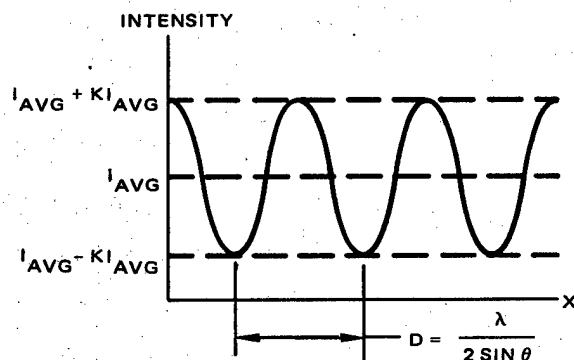


Figure 6-15. The interference of two waves produces a sinusoidal intensity variation for holographic exposures.

Two proposed methods of generating the correct filter profile are shown in Figure 6-17. In the first, transparency film is drawn through the region containing a ring focus created by a lens-axicon pair. The focus creates the required opaque ring, and the less intense regions before and behind it can be used to provide the correct density taper. We have successfully fabricated a number of masks in this way. A more difficult method, but one in which the density taper could be controlled more accurately if necessary, is the second shown in Figure 6-17. Here, the lens and the film plane travel together, separated by the focal length of the lens. As the pair move away from the axicon, the diameter of the ring focus will grow. By controlling the speed of travel, any desired radial-profile filter can be generated.

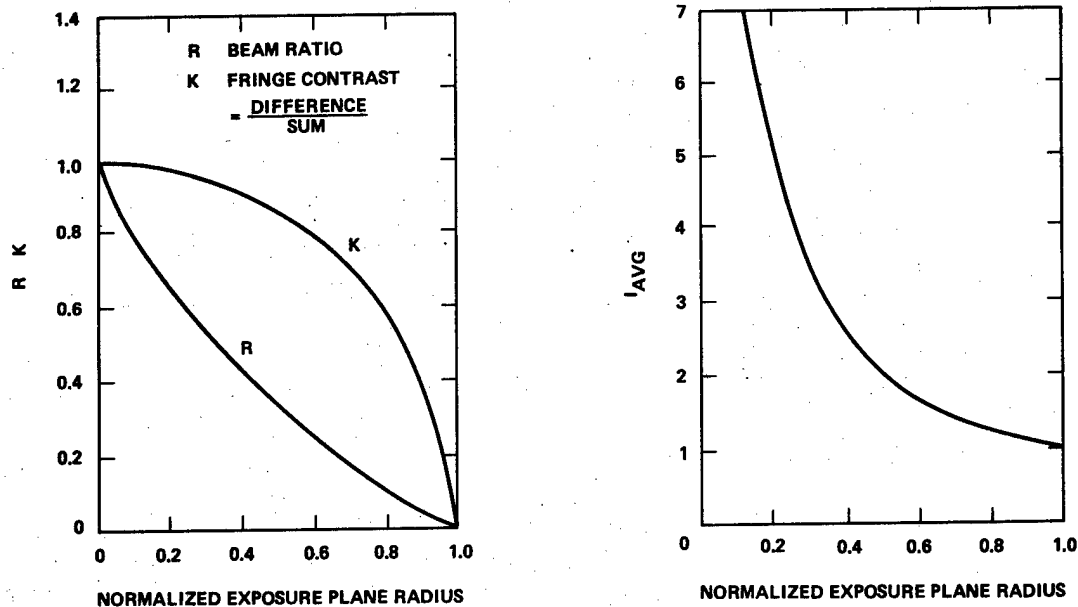


Figure 6-16. Fringe contrast and intensity variation in the exposure plane of a holographic grating axicon recording system.

Experimental exposures were made on both 4200 Å and 1000 Å thick photoresist layers. Without a density filter mask, when the grating axicon center was properly exposed, the edge of the grating axicon was underexposed. Properly exposed edges resulted in overexposure and lift-off of the grating in the center. Exposures using the thinner resist layer did produce a larger grating area, but it was insufficient for any phase measurements.

Several density filters were generated on 649F photographic emulsion on glass plate by the fabrication techniques described and used for exposure compensation. The feasibility of the concept was demonstrated in that we were able to attenuate the intensity variation to achieve grating definition at the center and edge of the exposure plane simultaneously. Further efforts to improve the profile of the density filter were halted in favor of developing an IR grating axicon.

### IR Techniques

Although IR grating axicons can be fabricated using the holographic exposure geometry described in the previous section, other fabrication methods were investigated. Because of the longer operating wavelengths, the grating periods are an order of magnitude larger than those of visible grating axicons.

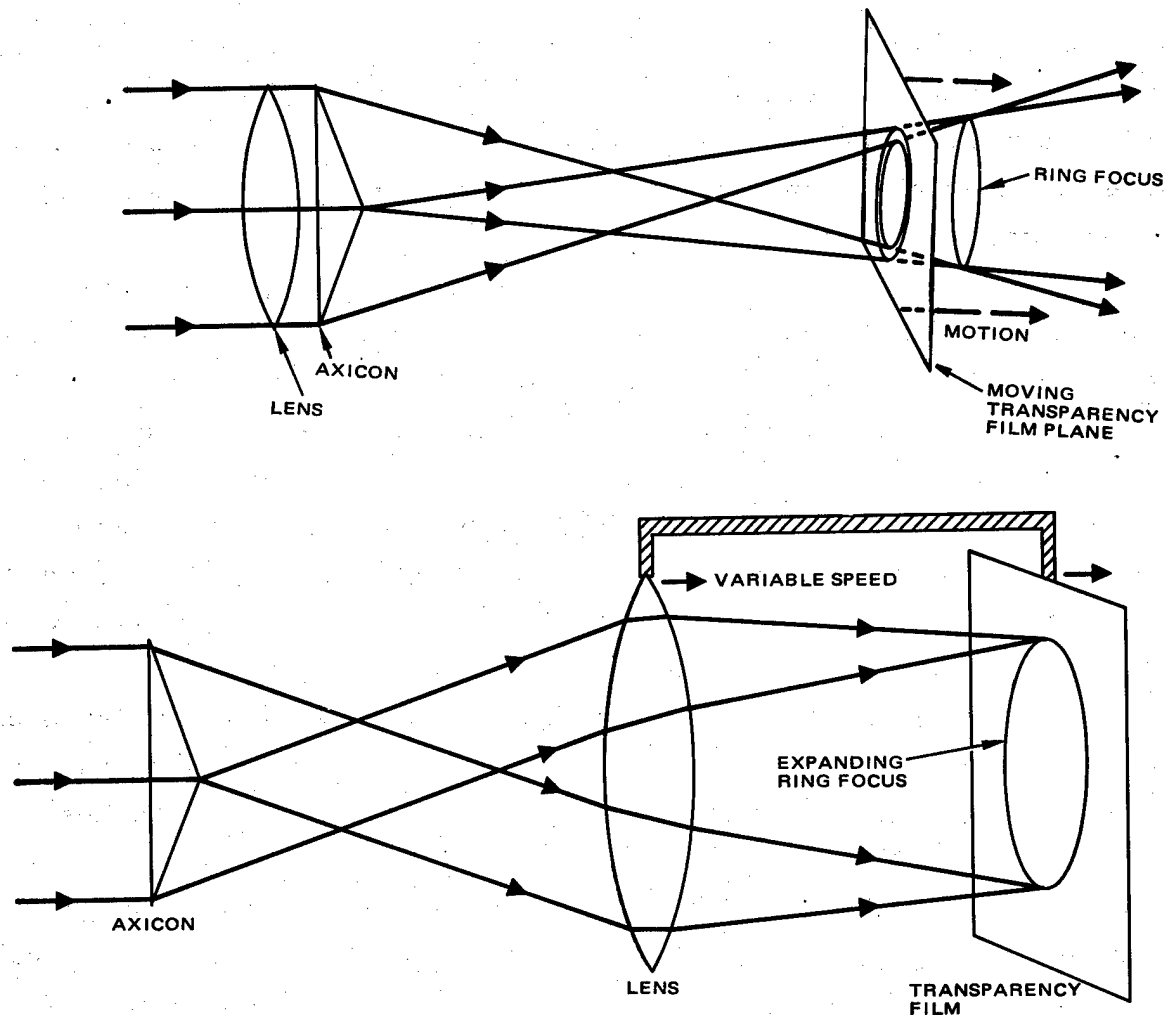


Figure 6-17. Two methods of generating a compensating filter for exposure of a holographic axicon, using photographic superposition.

The accuracy of precision mechanical and digital equipment, although inadequate for visible axicon grating fabrication, can be used to fabricate IR grating axicons by novel techniques.

One proposed technique uses linear interference fringes to approximate circular grating grooves. The substrate is exposed to the interference through a slit while being rotated about a central axis. Rotational stages with air bearings are capable of providing high rotational accuracy with minimal run-out. The major advantage of this method is the elimination of the glass cone required in the holographic exposure described previously, thereby making this technique highly adaptable to scale up to larger size grating axicons. However,

this method suffers from severe exposure intensity variations. Each radial location of the exposure plane rotates across the slit aperture at different angular velocity resulting in very high exposure at the center tapering off toward the edge. A mask with properly designed density profile could be utilized at the exposing slit to minimize this effect.

A more viable technique is to use a computer controlled plotter to draw a magnified version of the desired circular grating grooves. A reduced master pattern can then be obtained by photoreduction and used for contact printing the circular grating pattern into photoresist on the substrate of interest. This method is also suitable for scale up to larger sizes depending on the copy size of the computer plotter and the resolution of the photoreduction equipment. Grating axicon size can be further increased by generating only a segment of the symmetric circular pattern and using multiple contact printing to expose the complete pattern piecewise.

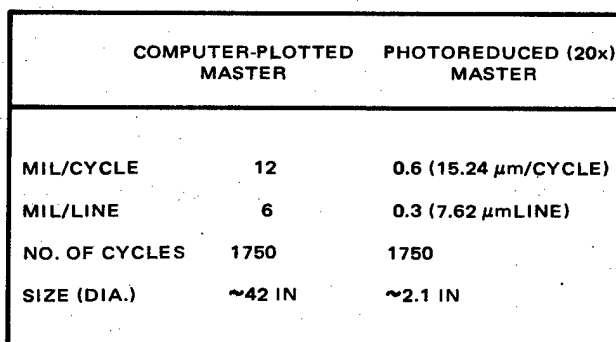
Pattern generators can "write" grating patterns in photoresist using an interferometric stepping table. However, their current feature size is limited to 0.2 mil, and the overall pattern size is limited to 1-2 inches.

Mechanical ruling of circular grating pattern may also be a viable fabrication method. Interferometric control similar to that presently used on linear grating ruling machines can control the radial location of the scribe and thereby determine the grating period. The substrate is then rotated to rule a circular grating axicon in gold or other material for use as a contact printing master.

#### Computer Generated Grating Axicon

Due in part to the difficulty in obtaining a large glass cone for holographic exposure and to the feasibility investigation of the computer controlled plotting technique, we initiated fabrication of a 2-inch diameter  $45^\circ$  diffracting IR grating axicon for the  $10.6 \mu\text{m}$  wavelength.

The Hughes Precision Plotting Facility was used to generate the magnified pattern described in Figure 6-18. The photoplotter exposed photographic film by projecting light images of various sizes and shapes. A computer



program controls the movement of the photohead thereby generating the desired pattern. Some specifications of the Hughes facility are:

		Aperture Size
Image tolerance . . . . .	0.3 mil	2 mil - 5 mil
(at film plane)	0.5 mil	6 mil - 150 mil
	1.5 mil	151 mil - 200 mil

6-25

The computer plotted grating axicon pattern used a 6 mil x 50 mil rectangular writing aperture. The 42 inch diameter pattern required drawing 1750 circular rings (6 mil wide lines) separated by 6 mil wide spaces. The grating period is 12 mil/cycle. The first attempt was aborted after 72 hours of computer plotting time during which only 2/3 of the desired pattern size was completed. Further complications were encountered due to fogging and handling of the large photographic sheet film during processing of the exposed pattern. On our second attempt, the computer program was optimized to minimize plotting time, and development techniques were improved. The completed pattern required 50 hours of computer plotting time. The writing aperture was controlled to draw straight line segments to approximate a circular arc to form each ring. Each circular ring was comprised of 800 line segments. The line segments lengthened as the circumference of each ring increased. The accuracy of the circular pattern can be improved by using more line segments per ring; however, the computing and plotting time required to complete the pattern is also increased.

The photoreduction was done by a vendor. The computer generated pattern is held in place by a 60 inch by 80 inch electrostatic copy board. The exposure system includes a 28-foot long vibration isolation support rail for the camera. The computer generated pattern was reduced 20x using a 250mm F4 Wray lens. Characteristics of this lens and other potentially useful lenses are listed:

	Resolving Power	Optimized Reduction	Flat Field
450mm F8 Wray Lens	0.5 mil	10x	7 inch
250mm F4 Wray Lens	0.1 mil	20x	2 inch
165mm F4 Ultra-Nikon Lens	0.1 mil	40x	1 inch

In general, larger field size is achieved at the expense of resolution.

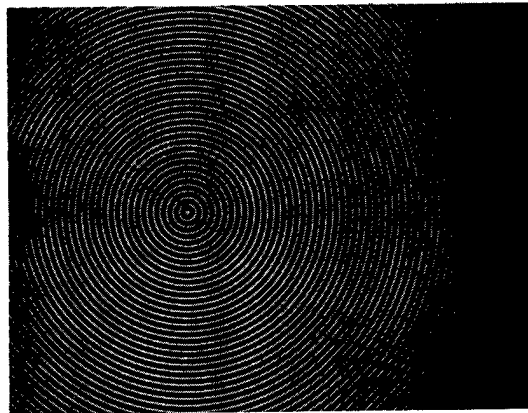
The first step in the photoreduction process was contact printing a positive of the computer generated pattern on another photographic sheet film. The positive as used to expose a reduced dark field image onto a photographic emulsion on glass. This pattern was then used to contact print photoresist

on chrome over a photomask-grade glass substrate. The chrome was chemically etched to obtain transparent grating regions. The finished chrome grating axicon master was comprised of clear and opaque (chrome) rings of  $15\text{ }\mu\text{m}$ /cycle. Investigation under the optical microscope showed no evidence of resolution degradation due to the camera lens.

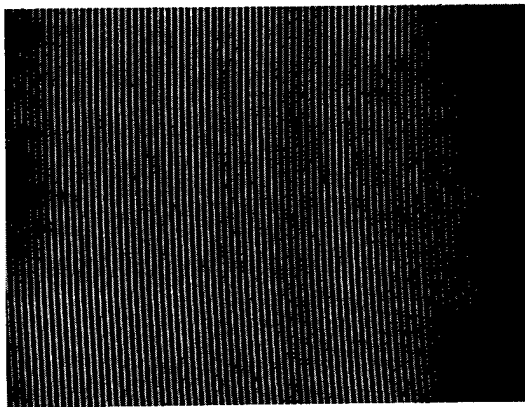
Microscope photographs of various sections of the reduced chrome mask pattern are shown in Figure 6-19. The grating period and duty cycle (chrome width/grating period) were measured using a filar micrometer calibrated to a stage micrometer with  $0.01\text{ mm}$  per division. Measurement repeatability was approximately 5 percent. No systematic deviation of grating period or duty cycle was evident. The average period of 13 measurements taken in increments of  $2.4\text{ mm}$  starting from the axicon center to the edge was  $15.19\text{ }\mu\text{m}$  with a standard deviation of  $0.31\text{ }\mu\text{m}$ . Average duty cycle was  $0.4547$  with a standard deviation of  $0.0023$ . Although microscopic interrogation indicates the chrome master pattern was quite good, the final test of accuracy of the computer plotting and photoreduction will be done by phase measurements using a point diffraction interferometer at the  $10.6\text{ }\mu\text{m}$  wavelength.

The chrome grating axicon master was used to expose photoresist on a sputtered gold film over a silicon wafer by contact printing using a UV light source. Shipley 1375 photoresist was spin coated to a layer thickness of  $2.6\text{ }\mu\text{m}$ . The exposed grating was developed for 2 minutes in AZ developer. Photographs of the photoresist grating pattern on gold as well as the chrome master pattern are shown in Figure 6-20.

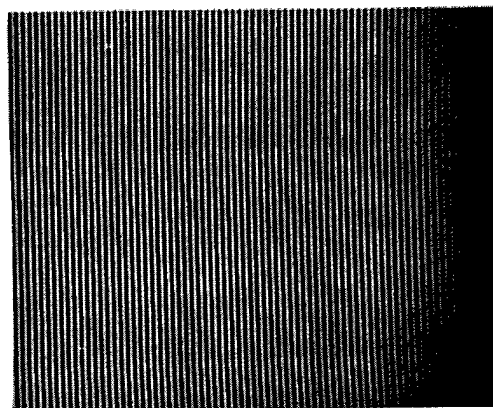
Non-uniformities in the resist layer prevent intimate contact of the chrome master pattern during exposure. Consequently moire fringes were superimposed on the circular grating pattern in localized regions. High quality thick resist coatings are difficult to obtain by spin coating techniques because of radial striations that form on the resist layer due to drying of the film during the spinning cycle. Techniques to eliminate these coating defects through the use of solvents to create an atmosphere of solvent vapor in the spinner bowl can only produce uniform layers of approximately  $1\text{ to }1.5\text{ }\mu\text{m}$ . Dip coating is better suited for achieving uniform thick photoresist layers required for the deep ion machining depths of IR grating axicons and especially for preparing these photoresist coatings over large area substrates.



a. Center



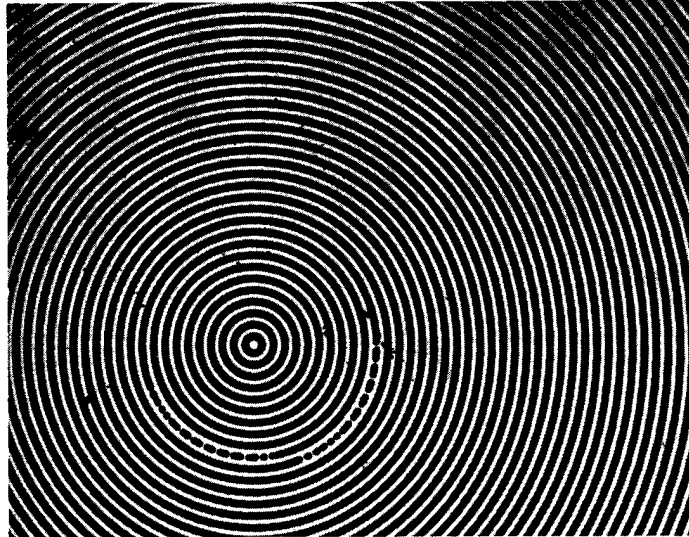
b. Mid-point



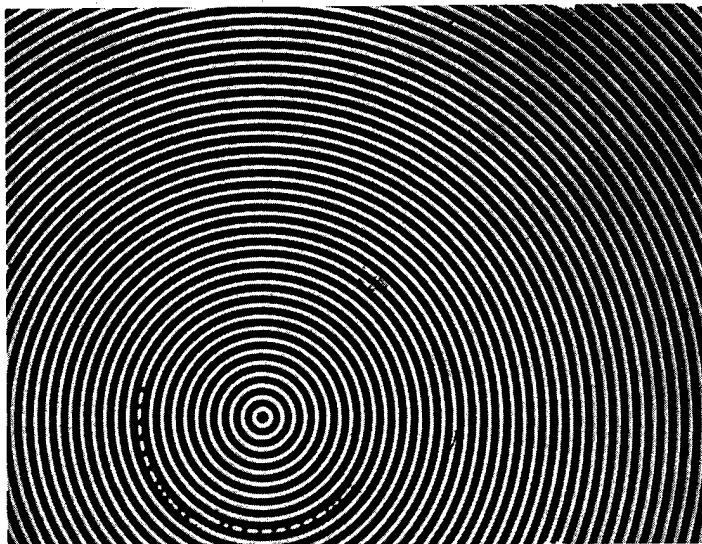
c. Edge

Figure 6-19. Microscopic photographs of (15.24 $\mu$ m/cycle) reduced chrome mask pattern for IR grating axicon.





a. Chrome contact printing master



b. Exposed photoresist on gold

Figure 6-20. Photoresist grating axicon is exposed using the chrome master pattern.

Exposed grating samples were ion machined and the excess photoresist was removed. Figure 6-21 shows the quality of the center of the grating axicon ion machined in gold. Figure 6-22 shows SEM photographs of ion machined axicon grating profiles in gold for various depths. The multifaceted sidewall is due to inadequate resist grating height. Efficiency measurements at a wavelength of  $10.6 \mu\text{m}$  indicated more etch depth is required to achieve peak efficiency in either polarization (see the following section on efficiency and polarization).

Fabrication of an inner and outer axicon pair is presently in progress. The chrome grating axicon master will be utilized to contact print both the inner and outer axicon substrate. Phase measurements using a point diffraction interferometer at the  $10.6 \mu\text{m}$  wavelength will determine the accuracy of axicon grating grooves fabricated via the computer controlled plotter and photo-reduction method.

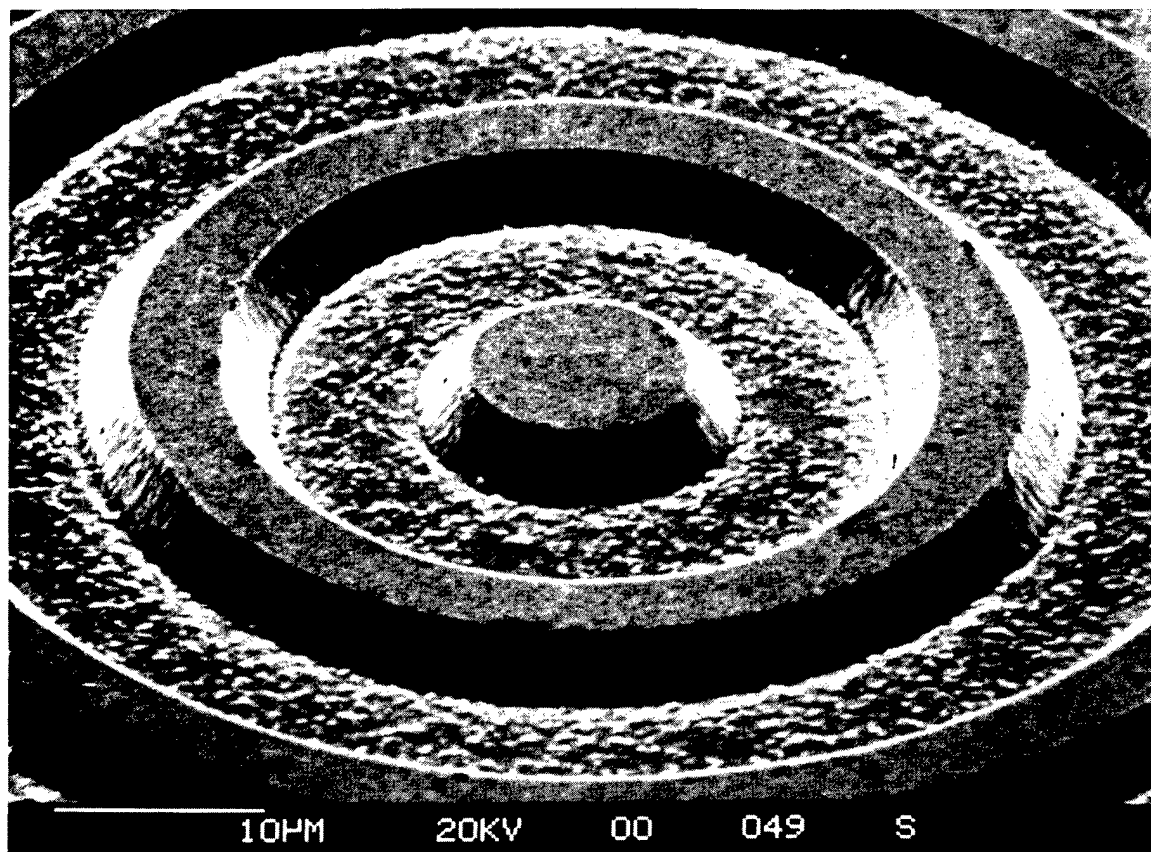
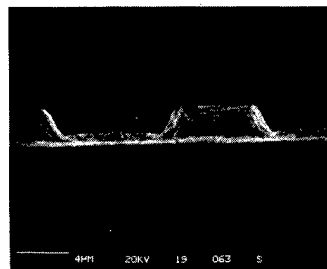
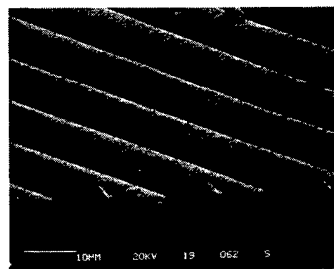
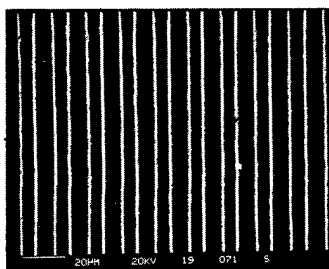
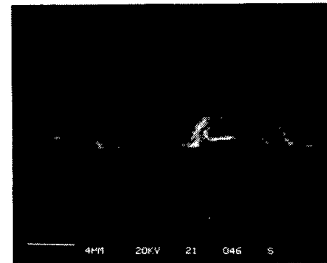
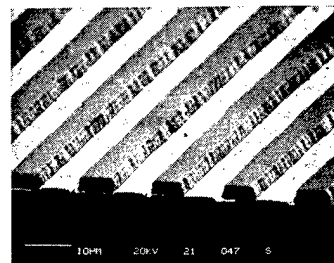
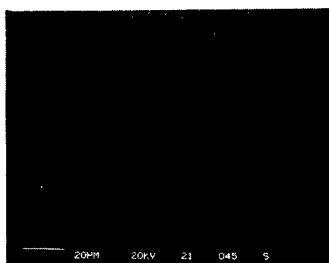


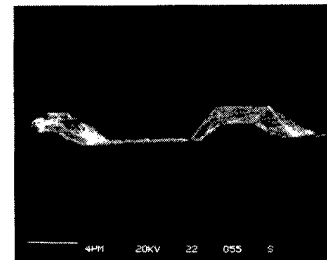
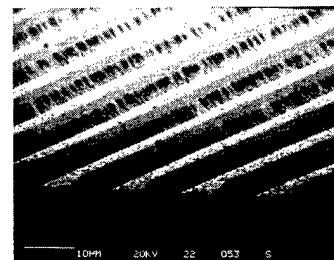
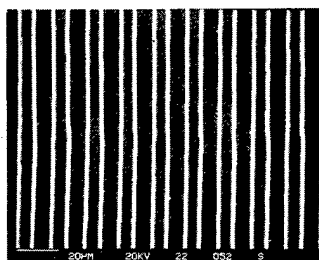
Figure 6-21. Grating axicon ( $15.24 \mu\text{m}/\text{cycle}$ ) center ion machines in gold.



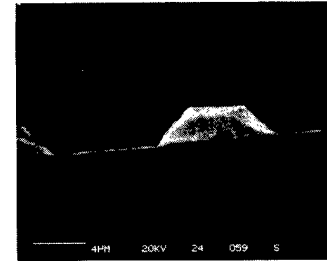
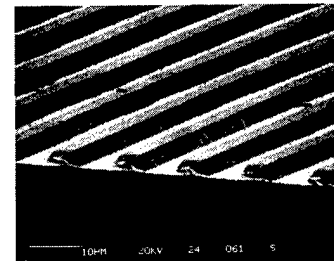
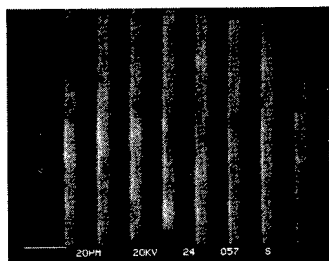
a. Ion-machined depth, 1.925  $\mu\text{m}$



b. Ion-machined depth, 2.115  $\mu\text{m}$



c. Ion-machined depth, 2.295  $\mu\text{m}$



d. Ion-machined depth, 2.475  $\mu\text{m}$

Figure 6-22. Ion-machined 15.24  $\mu\text{m}/\text{cycle}$  grating axicon profiles in gold.

## 6.5 EFFICIENCY AND POLARIZATION

Calculations of diffraction efficiency for an infrared grating axicon diffracting at  $45^\circ$ , and supporting measurements from holographic gratings were reported earlier in this program. (Holographic Grating Study Report, v. I., August '78, pp. 175-180). For the two possible polarizations of the incident wave, the peak efficiency occurred at different groove depths.

Polarization	Maximum efficiency into each order	Groove Depth
TE (E $\parallel$ )	0.47	0.29
TM (E $\perp$ )	0.50	0.24

Based on the theory and measurements, we can locate a crossover point at which equal efficiencies may be obtained:

Polarization	Crossover Efficiency	Groove Depth
TE or TM	0.45 - 0.46	0.28

If a linearly polarized wave is incident on a grating axicon, however, the grooves will lie perpendicular to the E-field (TM wave) in certain areas of the axicon, and parallel in others (TE wave). Figure 6-23 shows the spatial variation of the diffraction efficiency for several groove etch depths; the depth which optimizes either polarization in one quadrant of the axicon yields very much lower efficiency in the next quadrant. Uniform efficiency can be achieved by etching to the crossover depth, but net efficiency is below either of the two polarization peaks. Highest average efficiency may be attained by dividing the axicon into approximate quadrants and etching alternate quadrants for the TE or TM peak. The efficiency distribution would then follow the heavy line in the figure, raising the average efficiency from 45 percent to over 47 percent into each order.

If the axicon is to be used within a laser resonator, there is an even stronger argument in favor of splitting the axicon into quadrants of alternate etch depth. A uniform etch depth, if it favored one polarization even slightly, would predispose the laser to resonate in an undesirable radial or axial polarization. The non-uniform etch depth shown in Figure 6-23 would act instead to discriminate in favor of a uniformly linearly polarized wave.

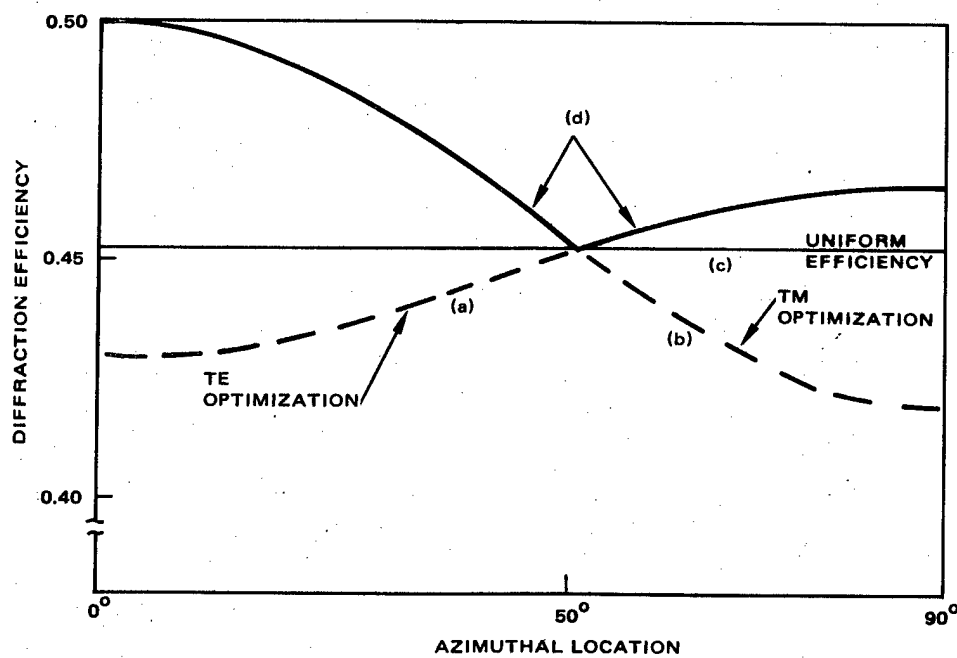
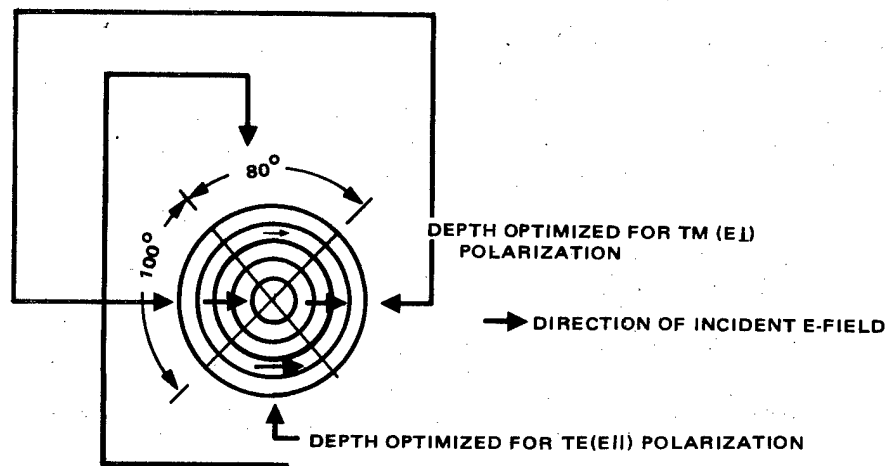


Figure 6-23. Predicted diffraction efficiency of a grating axicon; angular variation. (a) Groove depth optimized for (E $\parallel$ ) wave. (b) Groove depth optimized for TM(E $\perp$ ) wave. (c) Grooves etched to TE = TM cross-over point. (d) Etch depth optimized by quadrant, as shown above.

During this program we demonstrated the ease of ion machining unequal etch depths into adjacent segments. The sample was etched uniformly until the shallowest depth was achieved, then silicon wafer segments were laid over those sections in which no further etching was desired.

We were able to measure the diffraction efficiency of four axicon samples as shown in Figure 6-24. The results are shown in Figure 6-25. Measurements were made at  $10.6\text{ }\mu\text{m}$  with a collimated beam at normal incidence. In order to keep the diffracted beam from diverging too quickly and expanding beyond the aperture of the Scientech detector, we limited the beam to a 2 mm spot size and measured the efficiency close to the outer edge of the axicon, where groove curvature is less. In addition, we found it easier to measure the +1 order which diffracted into a focal spot on axis, rather than the -1 order, which diverged immediately upon diffracting (Figure 6-24). Unfortunately, the samples were not etched quite deeply enough to reach the peak of the efficiency curves for either polarization, but no problem is anticipated with doing so in the future.

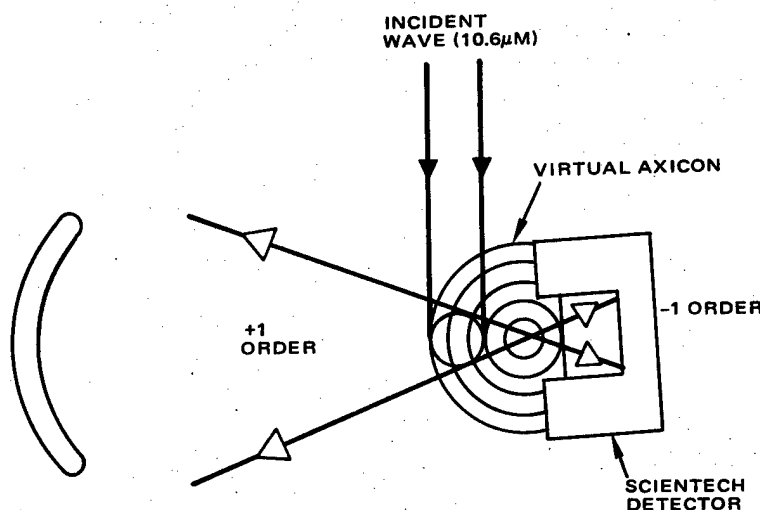


Figure 6-24. Measuring the diffraction efficiency of a grating axicon. Diffracted orders form sections of an annulus.

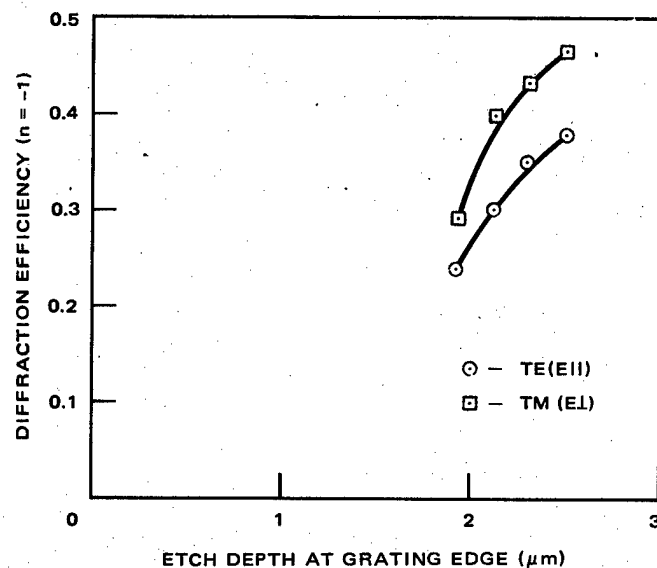


Figure 6-25. Measured diffraction efficiency ( $P_{-1}/P_{inc}$ ) of four grating axicon samples. Etch depth is measured by Dektak at the grating edge.

## 6.6 PHASE MEASUREMENT

Phase is most simply measured on a collimated or simply focused beam. We, therefore, proposed to create a "rhomb axicon," consisting of an inner-outer grating pair. A collimated wave will diffract into a cone from the  $\pm 1$  orders of the inner axicon, and be recollimated into an annulus by the  $-1$  order of the outer axicon. Fabrication is underway; at the time of this writing, matched pairs of substrates have been polished and coated with gold and photoresist. No unusual problems are anticipated.

Following the calculations of Koliopoulous et al.,\* we were able to design and demonstrate a point diffraction interferometer (Smartt interferometer) at  $10.6 \mu\text{m}$ . This interferometer has the advantage that it does not require a vibration isolation table, and more importantly for us, it is not necessary to anticipate how much the optical element under consideration will attenuate the beam. The low efficiency of the outer axicon ( $<50$  percent since only one order can be used) will be unimportant.

\*C. Koliopoulous et al., Infrared point-diffraction interferometer, Optics Letters, v. 3 No. 3, 9/78.

The interferometer functions by allowing a small fraction of a focused beam to pass through a pinhole on a partially transmitting substrate. If the pinhole is much smaller than the focused spot, an unaberrated spherical wave will be emitted. This wave will interfere with the transmitted fraction of the aberrated wave. Our setup is shown in Figure 6-26. Intensity matching of the reference and aberrated beams can be accomplished by choice of pinhole diameter, PDI plate transmissivity,  $f\#$  of the incident beam, and the choice of the central spot or a lower local maximum to be incident on the pinhole.

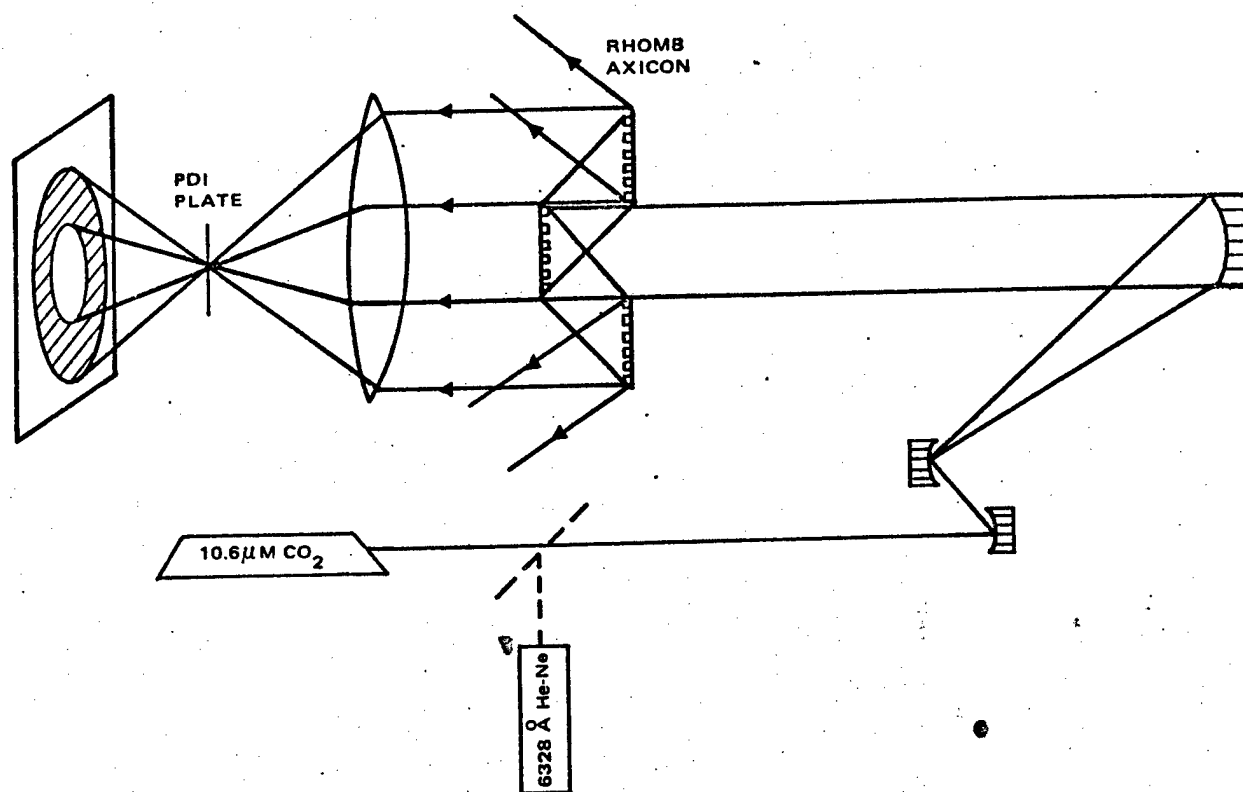


Figure 6-26. Point diffraction interferometry at  $10.6\mu\text{m}$ .



A PDI plate was fabricated using techniques similar to those of grating fabrication. We deposited gold on a ZnSe flat to achieve a transmissivity of 0.1 percent at  $10.6\text{ }\mu\text{m}$ , spun on photoresist, contact printed holes of various sizes (12.5, 20,  $30\text{ }\mu\text{m}$ ) into the resist using spatial filter foils, and ion-etched through the gold to form transmitting pinholes. The resulting interference pattern was then imaged with a pyroelectric vidicon. The high quality of a test interferogram of our unaberrated beam is shown in Figure 6-27.

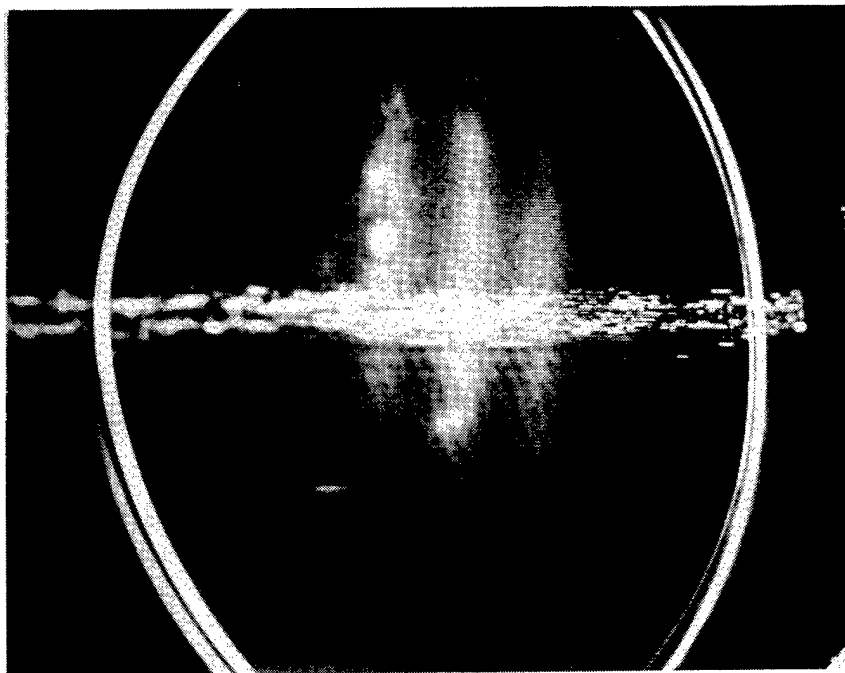


Figure 6-27. Interferogram of PDI system without axicon rhomb. Pattern at  $10.6\text{ }\mu\text{m}$  was detected with a pyroelectric vidicon and displayed on a TV screen. Light band through the center of the pattern is due to electrical interference.